

The Extraction and Study of Interstellar Grains

A thesis submitted to The University of Manchester for the degree
of Doctor of Philosophy in the Faculty of Science and Engineering

2018

Alex Clarke

School of Earth and Environmental Sciences
The University of Manchester

List of Contents

List of Contents	2
List of Figures	6
List of Tables	9
The Extraction and Study of Interstellar Grains.....	10
Declaration.....	11
Copyright Statement.....	12
Acknowledgments.....	13
About the Author	15
Chapter 1: Introduction	16
1.1 Context of the Project	16
1.2 Project Aims.....	17
1.3 Thesis Outline	18
Chapter 2: Literature Review	20
2.1 Stellar Formation, Evolution, and Nucleosynthesis	20
2.1.1 Stellar Evolution.....	21
2.1.1.1 Main Sequence.....	21
2.1.1.2 Red Giant Branch	23
2.1.1.3 Asymptotic Giant Branch	24
2.1.1.4 Novae and Supernovae	25
2.1.2 S- and R-Process Nucleosynthesis	27
2.1.2.1 S-Process	28
2.1.2.2 R-Process.....	30
2.1.2.3 P-Process.....	32
2.2 Presolar Grains	32
2.2.1 Formation	33
2.2.2 Processing in the Interstellar Medium	34

2.2.3 Processing in the Solar Nebula and Solar System.....	35
2.2.4 Discovery and Isolation from Meteorites	35
2.2.5 Analysis	38
2.3 Presolar SiC.....	41
2.3.1 Presolar SiC Sub-Groups	41
2.3.1.1 Mainstream Grains.....	41
2.3.1.2 Type AB Grains	42
2.3.1.3 Type C Grains	44
2.3.1.4 Type X Grains.....	45
2.3.1.5 Type Y Grains.....	46
2.3.1.6 Type Z Grains.....	46
2.3.1.7 Nova Grains.....	47
2.3.2 Trace Elements	47
2.3.3 Morphology	48
Chapter 3: Experimental Methods.....	49
3.1 Sample Preparation	49
3.1.1 Gently Separated Grains	49
3.1.2 Acid Residue Grains	55
3.1.3 In-situ Grains.....	57
3.2 Scanning Electron Microscopy (SEM).....	58
3.3 Secondary Ion Mass Spectrometry (SIMS)	58
3.3.1 NanoSIMS.....	62
3.3.2 TOF-SIMS.....	65
3.3.2.1 Primary Ion Gun	65
3.3.2.2 Secondary Ion Extraction	65
3.3.2.3 Flight Tube and Detector	67
3.3.2.4 Data Analysis	68
Chapter 4: Isotopic Fractionation Induced by Sample Topography During SIMS Analysis	69

4.1 Introduction.....	69
4.2 Methods	74
4.2.1 SIMION Modelling.....	74
4.2.2 NanoSIMS Analysis.....	77
4.3 Results and Discussion	78
4.3.1 SIMION Modelling.....	78
4.3.1.1 High Energy Secondary Ions.....	78
4.3.1.2 Low Energy Secondary Ions	80
4.3.2 Effects of Altering Cy.....	83
4.4 Conclusions.....	85
Chapter 5: A Comparison of Acid Residue and <i>In-Situ</i> Presolar SiC Grains	87
5.1 Introduction.....	87
5.2 Experimental Methods	91
5.2.1 Sample Preparation	91
5.2.2 NanoSIMS Analysis.....	92
5.2.3 Data Reduction	94
5.3 Results	95
5.4 Discussion	97
5.3.1 Carbon and Nitrogen Isotopes.....	97
5.3.1.1 Acid Residue Grains.....	97
5.3.1.2 In-Situ Grains.....	99
5.3.2 Silicon Isotopes	103
5.4 Conclusions.....	106
Chapter 6: A Comprehensive Analysis of Ten Presolar Silicon Carbide Grains	108
6.1 Introduction.....	108
6.2 Experimental Methods	110
6.2.1 Sample Preparation	110
6.2.2 NanoSIMS.....	111

6.2.3 TOF-SIMS.....	112
6.2.4 Data Analysis.....	113
6.3 Results	114
6.3.1 Carbon, Silicon and Nitrogen Isotopes	114
6.3.2 Element Depth Profiles	116
6.3.2.1 JA-MM2 grains	116
6.3.2.2 KJG grains	118
6.4 Discussion	122
6.4.1 Carbon, Silicon and Nitrogen Isotopes	122
6.4.2.2 KJG Grains	122
6.5 Conclusions.....	124
Chapter 7: Summary and Future Work.....	125
7.1 Issues with ‘Gentle Separation’	125
7.2 Comparison of Acid Residue and <i>In-Situ</i> Grains	126
7.3 Effect of Sample Topography on Secondary Ion Extraction in the NanoSIMS.....	127
7.4 Trace Element Depth Profiles.....	128
7.5 Future Work.....	129
7.5.1 Gently Separated SiC Grains	129
7.5.2 Acid Residue and <i>In-Situ</i> Grains	129
7.5.3 Trace Element Depth Profiling.....	130
References	131
Appendix	149

Word Count: 40730

List of Figures

Figure 2.1: Hertzsprung-Russell diagram depicting stellar evolution.....	22
Figure 2.2: Abundance of elements in the solar system.....	24
Figure 2.3: Cross-section of a supernova, displaying the onion-shell model of explosive nucleosynthesis.....	27
Figure 2.4: S- and r-process pathways around Xe on the chart of the nuclides.....	28
Figure 2.5: S- and r-process pathways on the chart of the nuclides.....	30
Figure 2.6: $^{12}\text{C}/^{13}\text{C} - ^{14}\text{N}/^{15}\text{N}$ distribution of presolar SiC grains.....	43
Figure 2.7: Si three-isotope plot of presolar SiC grains.....	43
Figure 2.8: $^{12}\text{C}/^{13}\text{C} - ^{26}\text{Al}/^{27}\text{Al}$ distribution of presolar SiC grains.....	44
Figure 3.1: Stainless steel pestle and mortar used to crush meteorite chips during the gentle separation procedure.....	50
Figure 3.2: Predicted grain size distributions of the fractions produced following the size separation step of the gentle separation procedure.....	52
Figure 3.3: Predicted grain size-density distributions of the fractions produced following the density separation step of the gentle separation procedure.....	53
Figure 3.4: Optical image of sample gently separated sample GRA-1.....	54
Figure 3.5: Overview of the 'Chicago Procedure'.....	56
Figure 3.6: Optical images of the three acid residue samples: KJG, JA-MM and JA-MM2.....	56
Figure 3.7: Optical images of the two polished meteorite sections: Acfer 094 and GRA 95229.....	57
Figure 3.8: Energy spread of atomic and molecular secondary ions produced during sputtering with a primary ion beam.....	60
Figure 3.9: Schematic of the Cameca NanoSIMS 50L.....	63
Figure 3.10: Typical $^{12}\text{C}^-/^{13}\text{C}^-$ isotope ratio image of a SiC grain, produced using L'Image following NanoSIMS analysis.....	64
Figure 3.11: Overview of the IDLE-3 TOF-SIMS instrument.....	66
Figure 4.1: Secondary ion images of $^{12}\text{C}^-$, $^{12}\text{C}^{14}\text{N}^-$, $^{12}\text{C}^{15}\text{N}^-$ and $^{28}\text{Si}^-$ from grain AC-KJG-1.....	71
Figure 4.2: Kinetic energy spread of Si^- , C^- and CN^- secondary ions.....	72
Figure 4.3: Secondary ion images of $^{12}\text{C}^-$, $^{12}\text{C}_2^-$ and $^{12}\text{C}^{14}\text{N}^-$, displaying the heterogeneous images produced by altering Cy.....	73
Figure 4.4: Potential array of the lenses nearest the sample surface in the NanoSIMS.....	75

Figure 4.5: SIMION model showing the penetration of equipotential surfaces through the EOW lens.....	76
Figure 4.6: SIMION model showing the distortion of the local electric field over a 5 μm grain at the sample surface.....	76
Figure 4.7: Secondary electron image of a group of terrestrial SiC grains.....	78
Figure 4.8: Simulated trajectories of high energy (20 eV) secondary ions in the NanoSIMS.....	79
Figure 4.9: Simulated trajectories of high energy (20 eV) secondary ions in the NanoSIMS.....	79
Figure 4.10: Simulated trajectories of low energy (0.1 eV) secondary ions in the NanoSIMS.....	80
Figure 4.11: Simulated trajectories of low energy (0.1 eV) secondary ions in the NanoSIMS.....	81
Figure 4.12: Cumulative currents of C^- , CN^- and Si^- secondary ions as a function of slit width.....	82
Figure 4.13: Variation in $^{12}\text{C}/^{13}\text{C}$ ratios of atomic and molecular C secondary ions in terrestrial SiC grains at varying C_y values.....	84
Figure 4.14: Variation in $^{14}\text{N}/^{15}\text{N}$ ratios in terrestrial SiC grains at varying C_y values.....	84
Figure 5.1: $^{12}\text{C}/^{13}\text{C}$ and $^{14}\text{N}/^{15}\text{N}$ ratios of presolar SiC grains from the literature vs those measured with the NanoSIMS.....	90
Figure 5.2: Histogram comparing the $^{14}\text{N}/^{15}\text{N}$ distribution of SiC grains analysed with the NanoSIMS with the Presolar Grain Database.....	90
Figure 5.3: NanoSIMS isotope ratio image from which a presolar SiC grain can be identified by its $\delta^{13}\text{C}$ anomaly.....	93
Figure 5.4: Secondary ion images of $^{12}\text{C}^-$, $^{13}\text{C}^-$, $^{28}\text{Si}^-$ and $^{12}\text{C}^{14}\text{N}^-$ from grain AC-MM-43.....	94
Figure 5.5: $\delta^{13}\text{C}$ isotope ratio image of grain AC-MM-43.....	95
Figure 5.6: $^{12}\text{C}/^{13}\text{C} - ^{14}\text{N}/^{15}\text{N}$ ratios of acid residue and in-situ presolar SiC grains.....	96
Figure 5.7: Model demonstrating the effect of terrestrial contamination on the $^{14}\text{N}/^{15}\text{N}$ ratio of presolar SiC grains.....	98
Figure 5.8: Relationship between grain size and $^{14}\text{N}/^{15}\text{N}$ ratio of in-situ presolar SiC grains.....	101
Figure 5.9: Carbon and nitrogen isotope ratios of 13 presolar SiC AB grains.....	102
Figure 5.10: Model demonstrating the effect of terrestrial contamination on the $^{12}\text{C}/^{13}\text{C}$ ratio of presolar SiC AB grains.....	102

Figure 5.11: $\delta^{29}\text{Si}$ and $\delta^{30}\text{Si}$ isotope ratios of presolar SiC grains.....	104
Figure 5.12: Model demonstrating the effect of terrestrial contamination on the $\delta^{29,30}\text{Si}$ isotope ratios of presolar SiC grains.....	105
Figure 5.13: Relationship between grain size and $\delta^{29,30}\text{Si}$ ratios of in-situ presolar SiC grains.....	106
Figure 6.1: Secondary electron images of grains AC-KJG-2 and AC-KJG-3.....	110
Figure 6.2: NanoSIMS images showing the identification of presolar SiC grains from the JA-MM2 acid residue.....	111
Figure 6.3: $^{12}\text{C}/^{13}\text{C}$ and $^{14}\text{N}/^{15}\text{N}$ isotope ratios of 10 presolar SiC grains which were later analysed with TOF-SIMS.....	115
Figure 6.4: Silicon isotope ratios of 10 presolar SiC grains which were later analysed with TOF-SIMS.....	115
Figure 6.5: Secondary ion images of $^{12}\text{C}_2^-$, $^{12}\text{C}^{13}\text{C}^-$, $^{12}\text{C}^{14}\text{N}^-$, $^{12}\text{C}^{15}\text{N}^-$, $^{28}\text{Si}^-$ and $^{29}\text{Si}^-$ for grain AC-KJG-41.....	116
Figure 6.6: Secondary ion images of ^{10}B , ^{11}B , ^{12}C , ^{23}Na , ^{24}Mg , ^{27}Al , ^{28}Si , ^{29}Si , ^{30}Si , ^{39}K , ^{48}Ti and ^{52}Cr from grain MM2-3-19.....	117
Figure 6.7: Secondary ion images of ^{23}Na , ^{24}Mg , ^{27}Al , ^{28}Si , ^{29}Si , ^{30}Si , ^{39}K , ^{48}Ti , ^{49}Ti , ^{50}Ti , ^{52}Cr and ^{56}Fe from grain AC-MM2-1.....	117
Figure 6.8: Secondary electron images of grains AC-KJG-2 and AC-KJG-3 following NanoSIMS analysis.....	119
Figure 6.9: Trace element depth profiles of Na, Mg, K, Ti, Mn, Fe, Sr and Cr for grain AC-KJG-2.....	119
Figure 6.10: Trace element depth profiles of Li, O, Na, Mg, Al and Ca for grain AC-KJG-3.....	121

List of Tables

Table 2.1: Typical sizes and abundance of known presolar grain types.....	37
Table 3.1: Settling times and g-forces required for each grain fraction during the size separation step of the gentle separation procedure.....	52
Table 3.2: Settling times and g-forces required for the density separation of the 1-20 μm grain fraction during the gentle separation procedure.....	53
Table 3.3: Relative Sensitivity Factors for selected elements for both silicate and SiC glass standards, when analysing with Au ⁺ primary ions and delayed extraction.....	61
Table 3.4: Instrumental mass fractionation values for selected isotope ratios for silicate glass standards, when analysing with Au ⁺ primary ions and delayed extraction.....	61
Table 3.5: Detector configurations used during NanoSIMS analyses of presolar SiC grains.....	63
Table 6.1: Carbon, nitrogen and silicon isotope ratios of 10 presolar SiC grains, later analysed with TOF-SIMS.....	114
Table 6.2: Elemental abundances of Na, Mg, K, Ti, Cr, Mn, Fe and Sr for grain AC-KJG-2.....	120
Table 6.3: Elemental abundances of Li, O, Na, Mg, Al and Ca for grain AC-KJG-3.....	121

The Extraction and Study of Interstellar Grains

Alex Clarke

The University of Manchester

Submitted for the Degree of Doctor of Philosophy, March 2018

The aim of this thesis is to comprehensively analyse presolar silicon carbide (SiC) grains from several primitive meteorites in order to investigate their complicated history. During their residence in the interstellar medium, presolar grains are predicted to be affected by many processes which may modify their original elemental and isotopic composition.

Presolar SiC grains from three acid residues and two polished meteorite sections were analysed for their carbon, nitrogen and silicon isotope ratios with high spatial resolution, in order to compare the distribution of $^{14}\text{N}/^{15}\text{N}$ ratios compared to those found in the literature. As a result of this work, isotopic fractionation effects caused by the distortion of the electric field around the grain topography were identified. These effects have the potential to cause differential transmission of atomic and molecular secondary ions, particularly when small slits and apertures are selected during NanoSIMS analyses.

The measured $^{14}\text{N}/^{15}\text{N}$ ratios of the presolar SiC grains analysed in this work match well with existing literature data, although many grains cluster at relatively low $^{14}\text{N}/^{15}\text{N}$ values. These low ratios do not appear to be the result of either terrestrial contamination or isotopic dilution, and may instead represent real differences between the SiC grain populations of different meteorites.

The majority of mainstream SiC grains analysed in this work lie on a slope with a gradient of ~ 1.3 on a Si 3-isotope plot, in agreement with literature data. SiC grains from the JA-MM and JA-MM2 acid residues appear to lie on shallower slopes, although these samples show significant scatter in the data. Neither terrestrial contamination nor isotopic dilution can explain the apparent fractionation of silicon isotopes in these samples. It is possible that these ratios may represent a difference in the Si ratios of grain populations of different meteorites, although fractionation during the sample preparation phase cannot be excluded.

Ten presolar SiC grains from the KJG and JA-MM2 acid residues are comprehensively analysed for their trace element compositions using Time-of-Flight Secondary Ion Mass Spectrometry. The majority of analyses are significantly affected by the proximity of neighbouring grains, leading to high background counts which prevent the reliable determination of elemental abundances for many elements. Depth profiles of several elements are determined for two grains from the KJG residue. Each of the measured elements displays approximately homogeneous profiles through the grains, with abundances in agreement with existing literature data. The uniform depth profiles may represent formation in a stellar envelope with a stable composition, although homogenisation by secondary alteration processes cannot be ruled out.

Declaration

No portion of the work referred to in the thesis has been submitted in support of an application for another degree or qualification of this or any other university or other institute of learning.

Copyright Statement

- i. The author of this thesis (including any appendices and/or schedules to this thesis) owns certain copyright or related rights in it (the “Copyright”) and s/he has given The University of Manchester certain rights to use such Copyright, including for administrative purposes.
- ii. Copies of this thesis, either in full or in extracts and whether in hard or electronic copy, may be made **only** in accordance with the Copyright, Designs and Patents Act 1988 (as amended) and regulations issued under it, or where appropriate, in accordance with licensing agreements which the University has from time to time. This page must form part of any such copies made.
- iii. The ownership of certain Copyright, patents, designs, trademarks and other intellectual property (the “Intellectual Property”) and any reproductions of copyright works in the thesis, for example graphs and tables (“Reproductions”), which may be described in this thesis, may not be owned by the author and may be owned by third parties. Such Intellectual Property and Reproductions cannot and must not be made available for use without the prior written permission of the owner(s) of the relevant Intellectual Property and/or Reproductions.
- iv. Further information on the conditions under which disclosure, publication and commercialisation of this thesis, the Copyright and any Intellectual Property and/or Reproductions described in it may take place is available in the University IP Policy (see <http://documents.manchester.ac.uk/DocuInfo.aspx?DocID=24420>), in any relevant Thesis restriction declarations deposited in the University Library, The University Library’s regulations (see <http://www.library.manchester.ac.uk/about/regulations/>) and in The University’s policy on Presentation of Theses.

*This thesis is dedicated to my grandad,
Michael Colby*

Acknowledgments

Firstly, I would like to express my sincere thanks to my supervisors, Ian Lyon and Torsten Henkel. Despite the many setbacks throughout this project, their enthusiasm, support and encouragement never wavered. I am particularly grateful for the knowledge and learning experiences they provided, particularly in the NanoSIMS and TOF-SIMS laboratories, where they ensured I really 'got to know' each instrument. Their contrasting approaches to working in the lab always kept me entertained, and meant they always had suggestions and advice when things went wrong.

Without the patience and support of Katie Moore and Greg McMahon, my time on the NanoSIMS would have been considerably more difficult. Both provided me with extensive training, and assisted with many of my early analyses. My thanks must also go to John Cowpe, Jon Fellowes, Karen Theis, and Cath Davies, who provided excellent technical and Health & Safety assistance throughout this PhD.

My thanks also go to the Isotope Geochemistry and Cosmochemistry group, who were always on hand to provide assistance, encouragement, distractions, and most importantly, cake. In particular, I'd like to extend my gratitude to Nat Curran, Katie Street, Sam Bell, Gemma Coleman, Katie Joy, Lisa Jepson, Fran McDonald, Mark Nottingham and Amy Kelly, who all ensured I stayed on track in their own way, for which I will always be grateful.

Completing this PhD would not have been possible without the love and support of my immediate family- Paula, Chris and Charlotte. Your motivational speeches, 'banter' and cups of tea were much appreciated, and I am thankful to have such supportive people in my life. My mum continues to be my biggest role model, with her seemingly endless patience and kindness, whilst Chris has been the best dad I could have ever asked for (although the jokes could use a little work). I hope to one day repay them for all they've done for me over the years. Finally, this PhD would never have even been started were it not for the encouragement of my sister, Charlotte. She will always be my biggest motivator, mostly out of sibling rivalry. As she heads towards the finish of her own PhD, I hope I can be there for her as much as she has been there for me.

About the Author

The author graduated from the University of Bristol in 2013 with an upper second class (2:1) honours in MSci Geology. Since September 2013, the author has been engaged with the research reported in this thesis.

Chapter 1

Introduction

1.1 Context of the Project

Presolar grains are stellar condensates which formed in the outflows and ejecta of late-stage stars, prior to the formation of the solar system. They are identified by their highly anomalous isotope ratios, which vary by up to several orders of magnitude relative to solar compositions (Zinner et al., 1987; Hoppe et al., 1994; Nittler, 2006). Since their discovery in the later 1980s (Lewis et al., 1987), many types of presolar grain have been discovered, including nanodiamonds, graphite, silicon carbide, oxides, silicates, silicon nitride, and refractory carbides (Bernatowicz et al., 1987; Lewis et al., 1987; Amari et al., 1990; Hutcheon et al., 1994; Nittler et al., 1994; Nittler et al., 1995; Choi et al., 1998; Nittler and Alexander, 1999; Zinner et al., 2003; Nittler et al., 2005b; Floss et al., 2008; Nittler et al., 2008).

Silicon carbides are the best studied presolar grains, with over 17,000 grains analysed to date (Hynes and Gyngard, 2009). Their popularity for analysis is due to their relatively high abundance (up to 150 ppm, although typically <40 ppm) (Huss and Lewis, 1995; Lodders and Amari, 2005; Floss and Stadermann, 2009; Leitner et al., 2012) in primitive meteorites, high abundance of trace elements, and relatively large size (many are 0.5-1 μm) compared to other presolar phases (Amari et al., 1994; Leitner et al., 2012).

Although well studied, the majority of analysed grains were extracted from their host meteorites using the 'Chicago Procedure' (Amari et al., 1994), which uses a series of harsh acid treatments to produce a nearly pure SiC residue. The procedure has been shown to damage and alter the surface of SiC grains (Stephan et al., 1997; Bernatowicz et al., 2003; Henkel et al., 2007a), resulting in the loss of important information about a grain's history.

The majority of SiC grains in the Presolar Grain Database were analysed using instruments with low spatial resolution, such as the older Cameca IMS 3f and 6f ion probes. It is shown here (see Chapter 5, this thesis) that SiC grains measured at high spatial resolution in the

Presolar Grain Database have, on average, higher $^{14}\text{N}/^{15}\text{N}$ ratios than the average of those recorded in the literature data (Hynes and Gyngard, 2009). This suggests that older, lower spatial resolution analyses may have been affected by contamination. A bias in measurements of $\delta^{13}\text{C}$, $\delta^{15}\text{N}$ or $\delta^{29,30}\text{Si}$ would lead to misinterpretation of astrophysical models of stellar nucleosynthesis, which to date have been unable to resolve the range of $^{14}\text{N}/^{15}\text{N}$ compositions seen in SiC grains (Amari et al., 2001c).

Despite their high abundances of trace elements, relatively few comprehensive studies have been carried out for presolar SiC grains. Many works used ion probes, such as the NanoSIMS, to determine abundances and isotope ratios of trace elements (Virag et al., 1992; Hoppe et al., 1994; Amari et al., 1995; Hoppe et al., 1996b; Gyngard et al., 2006; Huss and Smith, 2007; Marhas et al., 2007; Marhas et al., 2008; Groopman et al., 2015; Hoppe et al., 2015). However, as these analyses are highly destructive and can only measure a few ionic species at once, it is difficult to determine the composition of more than a few trace elements in each grain. Techniques such as Resonance Ionization Mass Spectrometry (RIMS) are less destructive, and able to measure many elements from a single grain. However, presently the technique is limited by analytical capability; RIMS instruments such as CHILI (Chicago Instrument for Laser Ionization) (Stephan et al., 2016b) can currently only measure Sr, Ba, Fe and Ni isotopes. Although not used extensively in presolar grain research, TOF-SIMS (Time-of-Flight Secondary Ion Mass Spectrometry) has been used to determine trace element abundances for many elements (Henkel et al., 2007a; Lyon et al., 2007; King et al., 2012). The technique is able to analyse the full mass spectrum in a single measurement, although with lower sensitivity and precision than other techniques.

1.2 Project Aims

The aim of this project is to comprehensively analyse presolar SiC grains from several primitive meteorites in order to investigate their complicated history. Presolar grains are expected to have been altered by many processes in the interstellar medium, solar nebula, and parent asteroids; analysing the distribution of elements within those grains with high resolution and precision may allow these effects of these processes to be determined.

As the use of acid treatments has been shown to alter the surface of grains, several sample preparation methods were used in this work. Grains from acid residues are compared with pristine grains extracted with a 'gentle separation' technique (Tizard et al., 2005), and also those measured *in-situ* from polished meteorite sections.

In this work, SiC grains were analysed with high spatial resolution, in order to determine the distribution of $^{14}\text{N}/^{15}\text{N}$ ratios compared to those found in the literature data (Hynes and Gyngard, 2009). If these ratios replicate those measured in other high spatial resolution studies, it will have important implications for astrophysical models of stellar nucleosynthesis.

Isotopic fractionation effects were discovered which were caused by the distortion of the electric field from the topography of analysed grains during NanoSIMS analysis. These isotopic fractionation effects were investigated in order to determine whether grain topography could induce significant errors into the measurement of isotope ratios in presolar SiC grains.

Eight presolar SiC grains were comprehensively analysed for both their major and trace element compositions using TOF-SIMS, whilst isotope ratios of the major elements, which are used to determine a grain's stellar origin, were determined using the NanoSIMS.

1.3 Thesis Outline

This thesis is presented in journal format, with several chapters prepared in a format suitable for publication.

Chapter 2: A review of the relevant literature related to this project, including stellar evolution and nucleosynthesis, presolar grains, and more specifically, an overview of the current understanding of presolar SiC grains.

Chapter 3: An outline of the methodology and analytical techniques used during this study, including the three sample preparation techniques, as well as an overview of the ESEM (Environmental SEM), TOF-SIMS and NanoSIMS instruments.

Chapter 4: Presented as a paper ready for submission. An analysis of the potential measurement artefacts produced during NanoSIMS analyses. The effects of secondary ion selection and grain topography on isotopic fractionation are investigated and discussed.

Chapter 5: Presented as a paper ready for submission. Compares the carbon, nitrogen and silicon isotope ratios of presolar SiC grains measured *in-situ* with those from acid residues. Grains are measured with high spatial resolution, and the potential effects of terrestrial contamination are discussed.

Chapter 6: A comprehensive analysis of ten presolar SiC grains from an acid residue. Isotope ratios of major elements are measured with high precision using the NanoSIMS, whilst depth profiles of several trace elements are determined using TOF-SIMS.

Chapter 7: A summary of the findings covered in this thesis, and suggestions for future work.

Chapter 2

Literature Review

Approximately 4.6 billion years ago, the solar system formed from the collapse of its parent molecular cloud, creating a proto-Sun surrounded by a flattened disk of gas and dust. The gravitational collapse of the molecular cloud is thought to have been caused by a supernova explosion in the local environment (Cameron and Truran, 1977; Boss, 1995; Boss et al., 2009).

As the disk cooled, solids began to condense from the gases, resulting in the formation of CAIs (calcium-aluminium-rich inclusions) and chondrules. These particles accreted together, along with a fine-grained matrix of metals and silicates, to form planetesimals (large, rocky bodies, >1 km in diameter). Further accretion of the planetesimals produced the planets, asteroids, comets, and other solar system bodies.

For many years, it was believed that these processes had homogenised the gas and dust from the presolar molecular cloud (Cameron, 1962; Suess, 1965), removing any evidence of material's origin, and creating uniform isotope ratios across all solar system bodies. However, the discovery of xenon and neon isotopic anomalies in primitive meteorites (Reynolds and Turner, 1964; Black and Pepin, 1969) suggested inhomogeneity remained, as well as the possibility that presolar material may have survived solar system formation.

The first presolar grains were isolated by Lewis et al. (1987), using the anomalous Xe signature as a tracer to locate presolar nanodiamonds. This discovery was followed by those of silicon carbide (Bernatowicz et al., 1987) and graphite (Amari et al., 1990), along with many others (see Section 2.2.4, this thesis). These grains have provided valuable information on stellar environments, as well as interstellar and meteorite parent body processing.

2.1 Stellar Formation, Evolution, and Nucleosynthesis

Models of the Big Bang suggest that the early universe was formed entirely of hydrogen, helium and lithium ($\sim 75\%$ H, $\sim 25\%$ He, minor ${}^7\text{Li}$) (Alpher et al., 1948). Due to the rapidly

falling temperatures, heavier elements couldn't be formed at this stage, and were instead produced later by nucleosynthesis in stars.

Evidence for stellar nucleosynthesis comes from astronomical observations. The surfaces of stars are typically enriched in the products of hydrogen- and helium-burning, as well as s-process elements (see Section 2.1.2.1, this thesis), and r-process nuclides from previous generations of stars. Additionally, supernova ejecta show enrichments in short-lived radioactive isotopes, which are produced by the r-process during the explosion (see Section 2.1.2.2, this thesis).

2.1.1 Stellar Evolution

2.1.1.1 Main Sequence

The majority of stars begin their lifetimes on the Main Sequence, a phase where a star gets progressively hotter and brighter, moving towards the upper-left of the Hertzsprung-Russell diagram (Figure 2.1). The Main Sequence is the longest phase of a star's lifetime, and is driven along by hydrostatic equilibrium- a balance between a star's high temperature gas pressure (from nuclear reactions) and gravitational collapse. Larger stars contain more fuel (for nuclear reactions) than smaller stars, but have shorter lifetimes, as the fuel is consumed faster in order to maintain hydrostatic equilibrium, which prevents a star from collapsing. For example, the Sun will have a lifetime of around 10 billion years, whilst high mass stars ($>10 M_{\odot}$) will expend their fuel in under 100 million years (Bertelli et al., 2009).

The Main Sequence is characterised by hydrogen-burning in the core of a star. Hydrogen-burning is the biggest source of energy for a star, and results in the creation of ^4He atoms. Helium is produced by two main processes- the proton-proton (p-p) chain, and the CNO cycle.

The p-p chain is dominant in low metallicity and low mass stars, where the core temperature is $<2 \times 10^7$ K. Three fusion pathways are possible, of which PPI is the most common- the PPII and PPIII chains do not become active until sufficient ^3He has been formed. The PPI chain forms ^4He via ^2D and ^3He , although ^3He abundances must initially be built up to increase the probability of two nuclei colliding and fusing together.

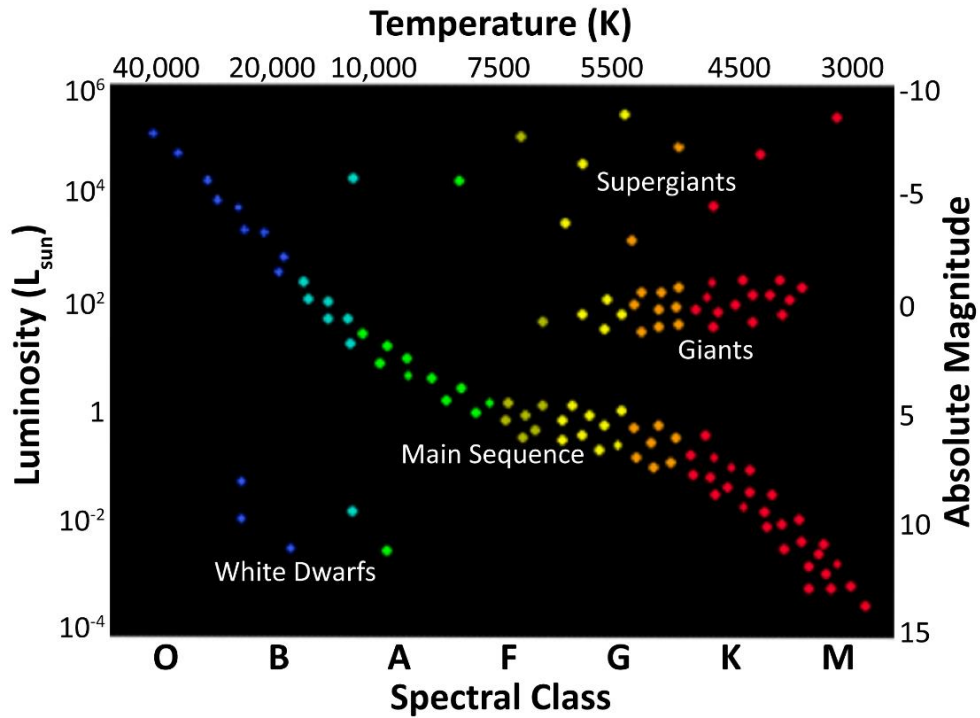


Figure 2.1: The Hertzsprung-Russell diagram, which plots the relationship between a star's surface temperature, luminosity, and spectral class. Around 90% of stars are on the Main Sequence. Adapted from

http://www.astro.cornell.edu/academics/courses/astro201/hr_diagram.htm.

Many stars are second generation or higher, and so have a higher initial metallicity. The presence of ^{12}C in these stars allows ^4He to be created by using C, N and O as catalysts. As with the p-p chain, there are several possible pathways which become active at different temperatures. Throughout the chain, the $^{12}\text{C}/^{13}\text{C}$ and $^{14}\text{N}/^{15}\text{N}$ ratios vary depending on which reactions are dominant, which affects the isotopic composition of any condensing dust grains.

In larger stars ($>8 M_{\odot}$) the Mg-Al cycle may also occur, providing temperatures exceed $\sim 1 \times 10^9$ K. This fusion pathway produces ^{26}Al , and so affects the initial $^{26}\text{Al}/^{27}\text{Al}$ measured in presolar grains.

As the availability of H decreases in a star's core, the p-p chain and CNO cycle reaction rates are slowed. As less energy is produced by the star, the gas pressure drops, causing the star to contract under gravity as it is no longer in hydrostatic equilibrium. As the star contracts, the core begins to heat up, which triggers H-burning in a shell surrounding the core.

The onset of hydrogen-burning in the shell increases the gas pressure, causing the star to expand (up to $50 R_{\odot}$), and trigger convection in the outer envelope. The star moves onto the Red Giant Branch (RGB) (see Figure 2.1); it increases in luminosity, but its surface temperature decreases due to its greatly increased surface area.

2.1.1.2 Red Giant Branch

During the RGB phase, stars continue to undergo hydrogen-burning in a shell surrounding the He-rich core. As the H-burning shell progresses away from the core, the convecting envelope begins to interact with it, bringing nucleosynthetic products to a star's surface, in a process known as the first 'dredge-up' (Iben and Renzini, 1983; Boothroyd and Sackmann, 1999). These products typically include ^4He , ^3He and ^2D , but C, O and N isotopes may also be present in stars which have undergone the CNO cycle during H-burning. These changes in the isotopic composition at the surface can be observed by astronomers (Busso et al., 1999; Abia et al., 2008).

As a result of H-burning in the shell, ^4He builds up in the star's core. The temperature and density of the star continue to rise, until He-burning in the core is triggered (at $\sim 10^8$ K). During helium-burning, ^4He atoms are fused together to form ^{12}C through the 'triple-alpha' process.

The triple- α process first involves fusing two ^4He atoms to form ^8Be - a highly unstable isotope, which is expected to decay before a ^4He atom can collide with it. However, it was discovered that ^8Be can form in a resonance state (Hoyle et al., 1953; Hoyle, 1954; Fowler and Greenstein, 1956; Burbidge et al., 1957; Cook et al., 1957), increasing its half-life by a factor of ~ 100 , allowing a third ^4He to fuse with it and form ^{12}C before it decays.

During He-burning, no elements between He and C are synthesised, as there are no stable isotopes of masses 5 or 8 (from adding either a proton or ^4He atom to another ^4He atom). As a result, Li, Be and B are found in low abundances across the universe, including in presolar grains (Figure 2.2).

Once ^{12}C has been formed, further ^4He atoms may be added to form ^{16}O , ^{20}Ne , ^{24}Mg , ^{28}Si , ^{32}S and ^{40}Ca . These are known as ‘primary’ isotopes, and are the most abundant isotopes of each element.

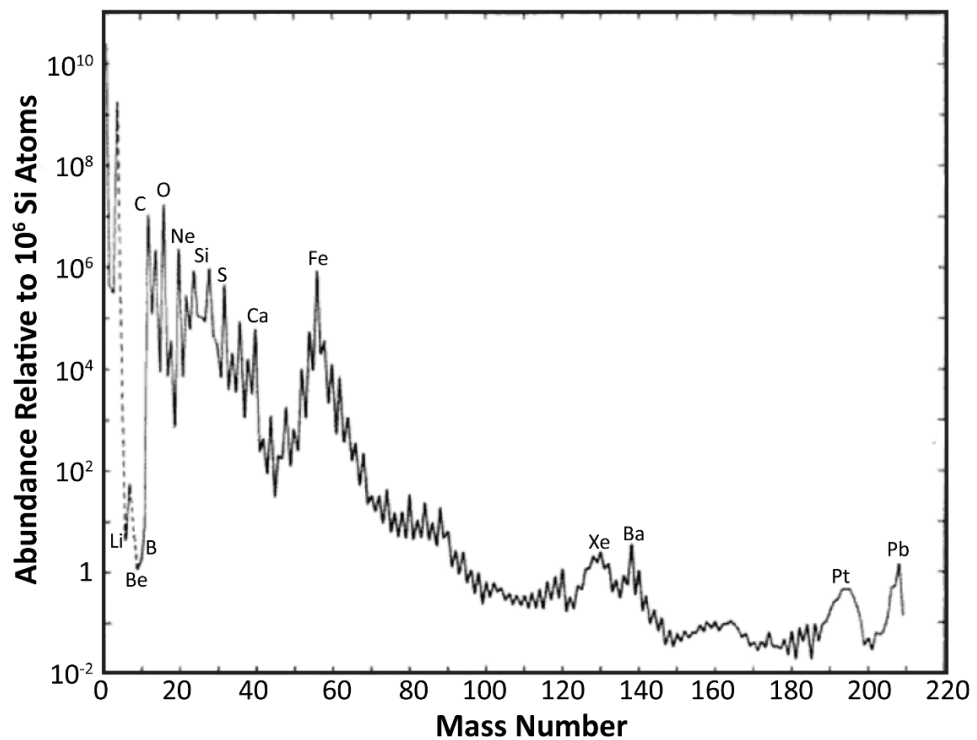


Figure 2.2: The abundance of elements in the solar system relative to 10^6 Si atoms.

Adapted from Cameron (1982).

As He is used up in the core, the core begins to contract and heat up as a result of the reduced gas pressure. The contraction brings the convecting envelope into contact with the H-burning shell, triggering a second dredge-up, which again brings newly synthesised elements to the star's surface.

2.1.1.3 Asymptotic Giant Branch

During the Asymptotic Giant Branch (AGB) phase, convection subsides, causing hydrogen-burning to begin in a shell surrounding the He-rich core. Hydrogen-burning increases the temperature of the star, triggering helium-burning in the He-rich shell surrounding the core. The helium is rapidly exhausted in a ‘helium-flash’, creating a thermal pulse which mixes material between different shells.

The intense heat of the thermal pulse creates thermal instability in the star. The structure of the star adjusts to radiate the excess heat, enabling convection to extend down to the

C-O-rich He-shell. The nucleosynthetic products are mixed to the surface in the third dredge-up, increasing the abundances of ^{12}C and ^{16}O at the star's surface. The star may experience up to 100 thermal pulse cycles during the AGB phase.

As a result of the large stellar radius, the gravity is lower at the surface of AGB stars, creating strong stellar winds. The winds cause extensive mass loss from the star, which creates a suitable environment for dust condensation. As a result, dust from AGB stars makes up the largest proportion of known presolar grain types (Alexander, 1997). The majority of presolar SiC grains are thought to condense around AGB stars, including mainstream, type Y and type Z grains (see Section 2.3.1, this thesis) (Hoppe and Ott, 1997; Nicolussi et al., 1997; Amari et al., 2001b).

Towards the end of the AGB phase, the H-burning shell gets close to the star's surface. The surface temperature may reach nearly 25,000 K, and the luminosity of the star greatly increases. The increased radiation illuminates the dust surrounding the star to form a planetary nebula. This phase may last for $\sim 10,000$ years, during which time the surface temperature continues to increase. In intermediate mass stars ($4-8 M_{\odot}$), the core may get hot enough to initiate carbon-burning and produce an O-Ne-Mg-rich core.

In stars $< 8 M_{\odot}$, the fuel in the core is exhausted towards the end of the planetary nebula phase, as the star cannot reach the temperature required for oxygen-burning. The star cools and contracts to form an electron degenerate White Dwarf. These stars are small, faint, and hot, and are found to the bottom left of the Hertzsprung-Russell diagram (Figure 2.1). White Dwarfs do not generate any energy, so continue to cool and contract, eventually becoming Black Dwarfs.

Massive stars, those $> 8 M_{\odot}$, are able to maintain high temperatures in their cores, enabling them to continue producing energy. These stars predominantly evolve into novae and supernovae.

2.1.1.4 Novae and Supernovae

The high temperatures in the cores of massive stars mean elements other than H, He and C can undergo fusion. As carbon is exhausted in the core, the star gravitationally collapses and heats up, initiating neon-burning when temperatures reach 1×10^9 K. Neon-burning

further increases the temperature in the star, triggering C-burning in the shell surrounding the core, along with He- and H-burning shells. These shells propagate outwards in the star, creating an 'onion-shell' structure (Figure 2.3).

Neon-burning is followed by oxygen-, magnesium- and silicon-burning. These fusion reactions have progressively shorter lifetimes as less energy is produced, meaning the fuel is used up faster. Eventually an iron-rich core remains, surrounded by shells of Si-, Mg-, O-, Ne-, C-, He-, and H-burning (Figure 2.3) (Woosley and Weaver, 1995). Elements heavier than Fe are not synthesised by fusion in the core as the reactions are endothermic. As a result, energy production in the star ends, causing the star to collapse under gravity.

As the star's core is electron degenerate it is initially able to withstand gravitational collapse. However, the core eventually exceeds the $1.4 M_{\odot}$ Chandrasekhar limit, and is no longer able to support itself. Iron nuclei in the core disintegrate into protons and electrons, before combining to form neutrons. This creates a neutron degenerate core, forming a neutron star.

The neutron star is able to withstand further collapse, causing the surrounding layers to 'bounce' off at supersonic speeds. The shockwave forms a hot, neutron-rich plasma, allowing heavier elements to be synthesised by the r-process (see Section 2.1.2.2, this thesis). Explosive H-burning (or 'hot CNO burning') may also occur during the explosion as the core temperature reaches 10^8 - 10^9 K. Nuclear reaction rates are much faster at these temperatures, allowing unstable nuclei to capture protons before they decay. This runaway nucleosynthesis generates large amounts of energy which powers the stellar explosion (as a Type II supernova).

During the explosion, material is ejected into the interstellar medium. This material, rich in nucleosynthetic products, seeds new interstellar clouds throughout the galaxy. Type II supernovae are thought to be the source of presolar SiC type C and type X grains (see Sections 2.3.1.3 and 2.3.1.4, this thesis).

Around 40% of stars $<10 M_{\odot}$ exist in binary systems, where one star is typically larger than the other, so evolves faster. The more evolved star transitions into a White Dwarf

and can gravitationally accrete material from the envelope of the neighbouring RGB star. The new material causes the star to increase in temperature and density, triggering explosive fusion reactions. If these reactions extend all the way to the core, the star explodes as a Type Ia supernova. However, if the reactions only involve the surface layers of the star, a nova outburst will occur. It is thought that some unusual presolar SiC grains may originate in nova outbursts (see Section 2.3.1.7, this thesis).

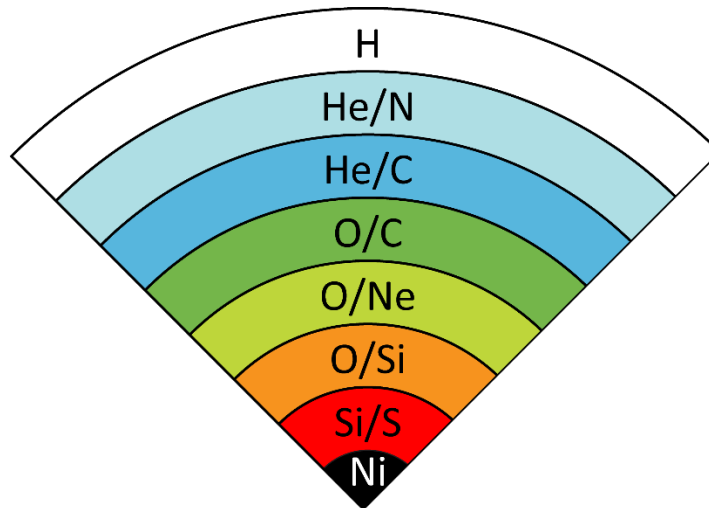


Figure 2.3: Cross-section of a star during a supernova explosion, showing the ‘onion shell’ structure. Each shell is named after the most abundant elements found in each layer.

Adapted from Zinner (2014).

2.1.2 S- and R-Process Nucleosynthesis

Elements and isotopes heavier than ^{56}Fe cannot be formed by fusion as the reactions are endothermic. Instead, they are predominantly produced by neutron-capture reactions. Free neutrons are produced during nuclear reactions and can be captured by seed nuclei (Burbidge et al., 1957) in reactions known as s- or r-process nucleosynthesis. These processes produce distinct nucleosynthetic components, which can be identified in presolar grains, and used to determine the astrophysical site in which the grains formed. Presently, the contributions from the s- and r-processes are approximately equal, although this has changed over time due to Galactic Chemical Evolution.

Some light, neutron-deficient isotopes are produced by the p-process. This process is not well understood, and will be discussed in Section 2.1.2.3.

2.1.2.1 S-Process

The s-process (or 'slow' process) occurs in regions with a low neutron density (Lugaro et al., 2003), mainly in the He-shells of thermally-pulsing AGB stars. The neutron fluxes are sufficiently low in these regions to allow nuclei to exist for 10^4 - 10^5 years before another neutron is captured. As a result, any unstable nuclei will decay before a neutron-capture reaction takes place (see Figure 2.4). Due to the low neutron-capture rate, these astrophysical sites must be stable for over 100 Myr for heavy elements to be produced by the s-process.

S-process elements are brought to a star's surface by convection, before being ejected into the interstellar medium by stellar winds. Presolar grains condense in these outflows, with the grain composition reflecting the contribution of the s-process component. For example, presolar silicon carbide grains contain Xe-S and Kr-S, components which are enriched in the s-process nuclides of Xe and Kr.

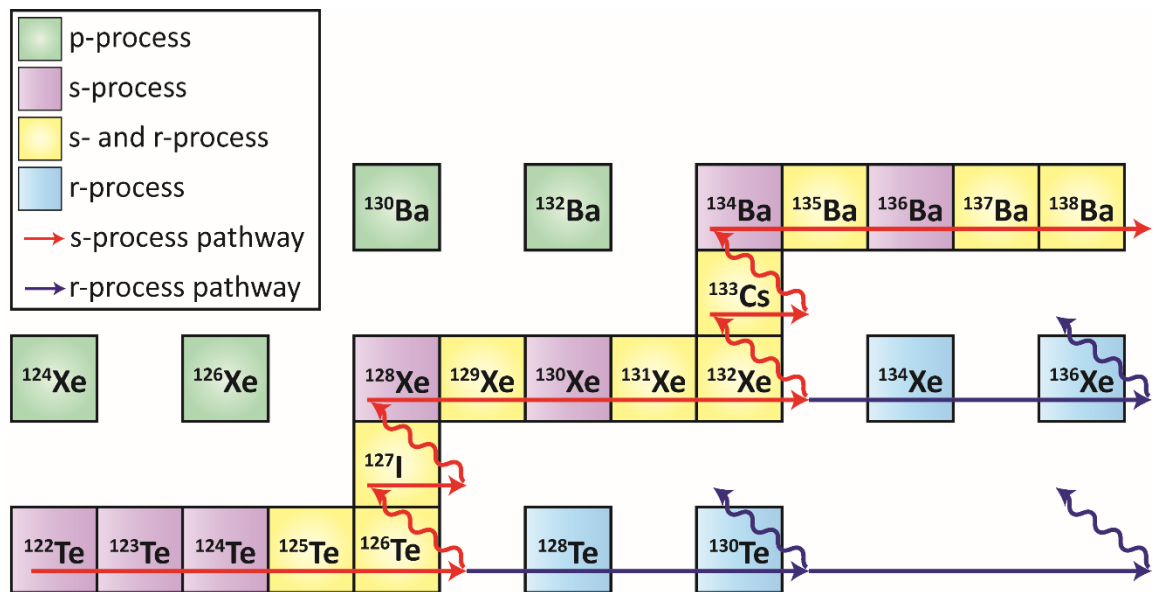
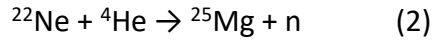
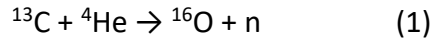


Figure 2.4: The s- and r-process nucleosynthesis pathways around Xe. P-process process nuclides are not well understood, but it is thought they may be formed by proton-capture reactions.

Free neutrons are unstable, with a half-life of ~15 minutes. As the s-process is so slow, neutrons must be produced *in-situ* to ensure they can be captured before they decay. Neutrons are mainly produced by two helium-burning reactions, shown below. The fusion

of carbon and helium (equation 1) is the most dominant, whilst equation 2 is a weak reaction which occurs in massive stars (Burbidge et al., 1957).



The probability of a nucleus capturing a neutron is determined by that atom's neutron-capture cross-section. If the resulting nucleus is stable, it can capture another neutron. However, if the neutron is unstable, it will decay before another neutron is captured, typically by β -decay. As ^{209}Bi is the heaviest stable nuclei, no heavier isotopes can be created by the s-process.

The s-process operates in a dynamic equilibrium between a nuclide's production (from neutron-capture on a seed nuclide) and destruction (from β -decay and neutron-capture) rates. Isotope abundances are determined by a nuclide's rate of destruction- for a stable nuclide, this is determined by its neutron-capture cross-section.

Some stable isotopes are shielded from the s-process due to the presence of unstable isotopes which come before them in the chain. These isotopes, such as $^{84,86}\text{Kr}$ and $^{134,136}\text{Xe}$, must instead be produced by the r-process (see Section 2.1.2.2, this thesis). As a result, enrichments of these isotopes in presolar grains can be used to determine the conditions in the parent star.

If a nuclei's β -decay half-life is similar to the rate of neutron-capture, branching may occur (Gallino et al., 1997; Lugaro et al., 2003), where both the β -decay and neutron-capture paths are followed. The abundances of isotopes along each path can be used to determine neutron densities at the astrophysical site. It is possible for branching to occur where an isotope can be produced in either a ground or metastable state. Each state has a different half-life, which potentially allows metastable isotopes to capture neutrons before they decay. At higher temperatures, the probability of forming a metastable isotope is greater, which is reflected in the isotopic abundances along each branch.

Both methods of branching produce distinctive isotopic components, which allow the temperature, pressure and neutron density of the star to be accurately determined.

These signatures can be measured in presolar grains (Lewis et al., 1990, 1994) and are used to determine the source of different presolar grain types.

Along the s-process pathway, several ‘Magic Numbers’ of nucleons are present (see Figure 2.5). Magic nuclides have stable configurations of nucleons, and as a result, they have small neutron-capture cross-sections. At the Magic Numbers, neutron-captures result in immediate β -decay, until a new stable nucleon configuration is reached. This process builds up abundances of ‘magic’ nuclei such as ^{88}Sr , ^{138}Ba and ^{208}Pb (see Figure 2.2).

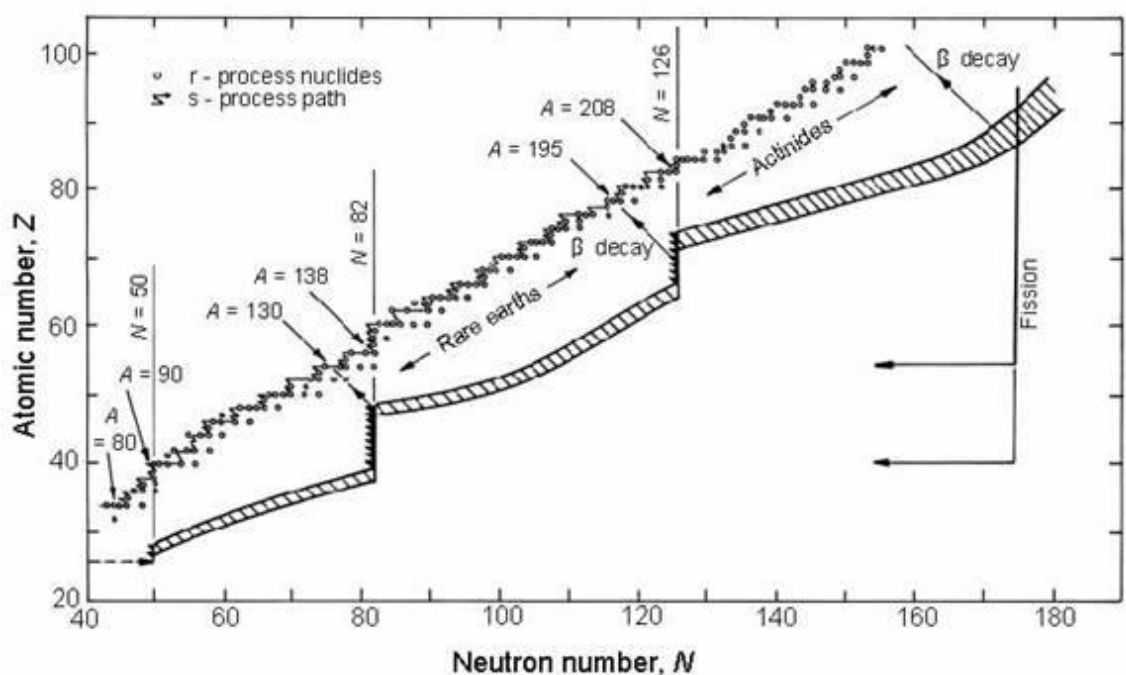


Figure 2.5: The pathways of the s-process and r-process on a chart of the nuclides (Seeger et al., 1965). S-process ‘Magic Numbers’ and r-process ‘Waiting Points’ are shown. The s-process produces nuclides around the valley of stability, whilst the r-process forms neutron-rich nuclei, away from the valley.

2.1.2.2 R-Process

The r-process occurs in regions with very high neutron densities, typically 10^{20} - 10^{23} cm^{-3} . The high neutron flux means neutron-capture rates are high, allowing unstable nuclei to capture neutrons before they decay. The r-process builds up abundances of neutron-rich nuclei, far from the valley of stability (Figure 2.5), which typically decay after a few microseconds. The r-process is also the only way elements and isotopes heavier than ^{209}Bi

can be created. The r-process overwrites the s-process signature for many elements, as the isotopes are used as seed nuclei.

The high neutron densities mean the r-process only occurs in extreme astrophysical environments, such as Type II supernovae. During the supernova explosion, material is ejected into the interstellar medium, where circumstellar grains carrying the r-process signature may condense. Based upon models of galactic chemical evolution, it has been suggested that either each supernova only ejects a small amount of r-process material, or only a fraction of supernovae eject material into the ISM (Thielemann et al., 2011).

Stable neutron configurations, known as 'waiting points', are reached along the r-process pathway. At the waiting points, additional neutrons cannot be captured without the nuclide immediately decaying by γ -ray dissociation. The stable configuration of neutrons means the nuclides have longer half-lives; as a result, their isotopic abundances build up (Figure 2.2). After successive neutron-captures and decays, the neutron configuration alters, allowing the waiting point to be passed. Waiting points occur at lower atomic masses than the s-process magic numbers (see Figure 2.5); waiting points occur at certain neutron numbers, whilst magic nuclei occur at specific nucleon numbers.

The neutron flux may be shut off when the supernova expands, decreasing the temperature, pressure and density. If this occurs, neutron-capture reactions will stop, and all unstable isotopes will undergo β -decay towards the valley of stability, until they reach a stable configuration. Some nuclei are shielded from the decay of r-process nuclides, and so can only be produced by the s-process, with their signatures able to be seen in presolar grains. For example, the Xe-S component in presolar SiC grains consists of the s-process isotopes ^{128}Xe and ^{130}Xe , which are shielded from the r-process by ^{128}Te and ^{130}Te (see Figure 2.4).

The initial composition of the star has no effect on the final composition from the r-process, as the nuclear reactions rates are fast enough to produce the same composition each time. Once β -decay has occurred, the same pattern of r-process isotopes is left each time.

2.1.2.3 P-Process

Compared to the s- and r-processes, p-process nucleosynthesis is vastly understudied, and as a result it is not well understood. The p-process is invoked as the method of producing the light, neutron-deficient isotopes of many elements, such as ^{124}Xe and ^{126}Xe (see Figure 2.4), which are bypassed by the s- and r-process pathways. There are 35 stable p-nuclides beyond Fe (Cameron, 1957; Rauscher et al., 2013), with each typically 10-1000 times less abundant than the neutron-rich isotopes (Pignatari et al., 2016).

Several reactions have been suggested for the production of p-nuclides, such as spallation reactions in the ISM (Audouze, 1970; Hainebach et al., 1976); photonuclear reactions during the H-burning cycle (Harrison, 1978); proton-capture reactions (Burbidge et al., 1957; Cameron, 1957; Arnould and Goriely, 2003); and photodisintegration of heavier nuclides, known as the γ -process (Arnould, 1976; Woosley and Howard, 1978; Rayet et al., 1995; Rauscher et al., 2002; Pignatari et al., 2016). Of these, the γ -process is the most likely reaction pathway for producing p-nuclides, as the other reactions are not predicted to occur with enough efficiency or in the correct astrophysical environments (Arnould and Goriely, 2003).

2.2 Presolar Grains

Presolar grains are sub-micron to micron-sized dust grains which formed as condensates in the outflows and ejecta of late-stage stars, prior to solar system formation. They are characterised by their highly anomalous isotope ratios for many elements relative to solar compositions, which can vary by several orders of magnitude (Zinner et al., 1987; Zinner et al., 1989; Alexander, 1993; Hoppe et al., 1994; Nittler, 2006). These isotopic anomalies cannot be produced by any physical process in the solar system (radioactive decay, cosmic-ray induced spallation, mass fractionation etc.) and are only explained by stellar nucleosynthesis. As a result, their elemental and isotopic compositions can be used to study nucleosynthetic processes and the stellar environments in which the grains formed.

Following their formation, the grains passed through the interstellar medium (ISM) into the presolar molecular cloud. As the solar system formed, the grains became incorporated into solar system bodies; to date, they have been found in primitive meteorites, interplanetary dust particles (IDPs), and cometary material (Huss and Lewis, 1995; Messenger et al., 2003; Messenger et al., 2005; McKeegan et al., 2006). Their

complicated history means they can be used to study processing in the interstellar medium, Galactic Chemical Evolution (GCE), the conditions of solar system formation, and the alteration history of their parent asteroids (Huss and Lewis, 1995; Jones et al., 1997; Alexander and Nittler, 1999; Ehrenfreund and Charnley, 2000; Verchovsky et al., 2001; Bernatowicz et al., 2003; Verchovsky et al., 2003; Lyon et al., 2007; Herbst and Van Dishoeck, 2009).

Prior to the discovery of presolar grains, all knowledge of stars and interstellar dust was determined from astronomical observations. However, this data is usually low resolution, meaning models of stellar processes cannot be accurately constrained. Analyses of presolar grains yield higher precision isotopic data, allowing astrophysical models to be tested and refined (Koehler et al., 1998; Lin et al., 2010; Lugaro et al., 2017).

2.2.1 Formation

Presolar grains formed in the stellar outflows and ejecta of late-stage stars. The isotopic composition of each grain reflects the composition of its parent star, allowing the source of each grain to be determined. The range of isotopic compositions found in presolar grains indicates a variety of stellar sources, including AGB stars, supernovae, and novae.

The composition of a star is important in determining the type of condensates which will form. Carbonaceous phases, such as SiC and graphite, form in carbon-rich stars, with $C/O > 1$ (Treffers and Cohen, 1974). Silicates and oxides form around oxygen-rich stars, where $C/O < 1$.

Astronomical observations have identified the presence of dust around AGB stars and in supernova ejecta (Lagadec et al., 2007; Sloan et al., 2016), suggesting the physical and chemical conditions in these regions are favourable for dust condensation. Modelling suggests that dust should condense in the outer shells of stars, where temperatures are < 2000 K, and pressures are between 10^{-3} and 10^{-7} bar (Lodders and Fegley, 1995). For grains to form in these regions, the density must be high enough to promote grain nucleation and growth.

2.2.2 Processing in the Interstellar Medium

Following their formation, presolar grains were driven into the interstellar medium by the stellar winds of their parent stars. The ISM is comprised of 99% ions and molecules (as gas), with a minor amount of dust, and has many regions of differing temperature, density, and composition. Presolar grains are expected to have resided in the ISM for >500 Myr (Jones et al., 1997; Hirashita et al., 2016; Wright et al., 2016), enabling many processes to affect them during their passage.

Whilst in the ISM, dust grains may be subjected to collisions (both with gas molecules and other dust grains), interaction with Galactic Cosmic Rays and UV radiation, vaporisation and recondensation, ion/atom implantation, surface ice formation, and supernovae shockwaves. Each of these processes would be expected to at least partially alter a grain, with the effects seen on the grain surfaces, rims, coatings, or composition. Each presolar grain has a complicated alteration history, with the effects of individual processes overlapping with each other.

Supernovae shockwaves can accelerate particles in the ISM up to 1000 km/s (Jones et al., 1997), resulting in the implantation of ions/atoms into the surfaces of dust grains. Analysis of individual presolar SiC grains has found elevated abundances of both Li and B in the grain exteriors, suggesting implantation in the ISM (Lyon et al., 2007). It has also been argued that the high abundances of noble gases in presolar grains may be a result of implantation by supernovae shockwaves (Verchovsky et al., 2001). Shockwaves can also shock dust grains, causing them to vaporise in the ISM, before recondensing again (Jones et al., 1994; Bocchio et al., 2014).

Collisions between individual grains are expected to result in the formation of pits and craters on the grain surfaces (Jones et al., 1997). However, a study of 81 pristine presolar SiC grains found no evidence of this (Bernatowicz et al., 2003). It is possible that these grains were protected by coatings during their residence in the ISM, as around 60% of the grains were found to be covered in a thin rim (~100 nm) of amorphous material (Bernatowicz et al., 2003).

Astronomical observations of clouds in the ISM have previously shown that many dust grains are covered by icy mantles (Ehrenfreund and Charnley, 2000). It is possible for

simple ices, such as H₂O, CO₂, CO, CH₃ and CH₃OH, to accrete onto the grains by surface absorption of atoms and molecules (Sandford and Allamandola, 1993; Messenger et al., 2006; Nuth et al., 2006). These icy mantles could then be processed by UV radiation and cosmic rays to produce organic coatings. The coatings seen on pristine presolar SiC grains are formed of an unknown material, but an organic nature has yet to be ruled out (Bernatowicz et al., 2003).

2.2.3 Processing in the Solar Nebula and Solar System

The presence of presolar material in solar system bodies (primitive meteorites, IDPs and comets) indicates that they must have survived the harsh environment of the early solar nebula. The nebula environment was potentially very destructive, with significant temperatures and cosmic radiation. All material in the nebula was subjected to extensive processing and homogenisation, and the remaining presolar material demonstrates the effects of this. By studying the size, mineralogy, and abundances of presolar grains, it is possible to investigate processes which occurred in the early solar system.

The fact that presolar material survived through the formation of the solar system means physical limitations can be placed on the conditions at this time. Modelling and experimental data have been used to test the survival of presolar grains in a range of conditions (Cassen and Chick, 1997). It is suggested that refractory material could survive at distances >1 AU, whereas volatiles would only survive beyond the orbits of Uranus and Neptune (20-30 AU). As the nebula cooled, these grains would have been able to migrate towards the Sun, explaining their incorporation in inner-solar system bodies.

In addition to being processed in the solar nebula, many presolar grains likely experienced alteration within their parent bodies. Presolar grains are dominantly found in primitive meteorites, within the fine-grained matrix, and underwent the same thermal or aqueous alteration that their parent asteroids did. As a result, many presolar grains were likely destroyed, resulting in a clear correlation between a meteorite's metamorphic grade and the matrix-normalised abundance of presolar grains (Huss, 1997).

2.2.4 Discovery and Isolation from Meteorites

As far back as the 1950's, it was known that material from many different stellar origins had contributed to the solar nebula (Burbidge et al., 1957; Cameron, 1957) but it was

assumed that this material was homogenised in the hot early nebula environment (Cameron, 1962; Suess, 1965). Analysis of solar system materials appeared to confirm this, with uniform isotopic compositions found across all measured samples, although these studies did not have the analytical capability to determine such small isotopic differences.

Isotope anomalies in hydrogen (Boato, 1954), xenon (Reynolds and Turner, 1964), and neon (Black and Pepin, 1969) were identified in meteorites, but largely ignored until anomalies were discovered for oxygen (Clayton et al., 1973), a major rock-forming element. Other anomalies were later discovered for Mg, Si, Ca, Ti, Cr, Ni, Sr and Ba in CAIs from primitive meteorites (a review of which can be found in Clayton (1988)), but identification of presolar phases took time due to their low abundances.

The first presolar grains were identified by using exotic noble gas components as tracers through a series of chemical and physical separation steps (Amari et al., 1994). The Xe-HL component, dominated by both the light ($^{124,126}\text{Xe}$, from the p-process) and heavy ($^{134,136}\text{Xe}$, from the r-process) Xe isotopes, was found to be hosted by presolar nanodiamonds (Lewis et al., 1987). Presolar SiC grains were identified by the Xe-S (s-process component, see Section 2.1.2.1, this thesis), Ne-E(H) and Kr-S (s-process component) signatures (Bernatowicz et al., 1987). Presolar graphite grains were discovered to carry the Ne-E(L) component (Amari et al., 1990).

Many subsequent discoveries were made using ion microprobes, particularly the NanoSIMS (see Section 3.3.1, this thesis). Along with silicon nitride grains, many oxides were identified from acid residues, including spinel, corundum, hibonite, chromite, Ti-oxide, Fe-oxide (Hutcheon et al., 1994; Nittler et al., 1994; Choi et al., 1998; Nittler and Alexander, 1999; Zinner et al., 2003; Nittler et al., 2005b; Floss et al., 2008; Nittler et al., 2008) (see Table 2.1). Other oxides, sulfides, metals, and Ti-, Zr- and Mo-rich carbides have been found as sub-grains within presolar SiC and graphite grains (Bernatowicz et al., 1991; Bernatowicz et al., 1996; Croat et al., 2003; Croat et al., 2008; Croat et al., 2010; Hynes et al., 2010; Croat et al., 2011a, b; Hynes et al., 2011; Croat et al., 2013; Haenecour et al., 2016). Within SiC grains, it is possible for TiC sub-grains to form by exsolution (Bernatowicz et al., 1992), but any sub-grains within graphite must have formed earlier.

Grain Type	Size	Abundance
Diamond	1-2 nm	1500 ppm
Silicon Carbide	0.1-10 μm	10-150 ppm
Graphite	1-20 μm	1-2 ppm
Corundum	0.2-3 μm	100 ppb
Spinel	0.1-20 μm	1.2 ppm
Hibonite	1-5 μm	20 ppb
Silicon Nitride	0.3-1 μm	1-20 ppb
Silicates	0.2-1 μm	200-3600 ppm
Refractory Carbides	10-200 nm	-

Table 2.1: Typical sizes and abundances of known presolar grain types. Accurate abundances have yet to be determined for presolar refractory carbides.

Presolar silicates were discovered in IDPs (Messenger et al., 2003; Nguyen et al., 2014) and primitive meteorites (Nagashima et al., 2004; Nguyen and Zinner, 2004; Yada et al., 2008) using isotope imaging on the NanoSIMS. The search for presolar silicates was complicated by the high abundance of silicates in extraterrestrial materials and the fact that the majority of silicates in meteorites are solar in origin. Automated imaging on the NanoSIMS enabled large areas of meteoritic samples to be analysed for isotope anomalies, leading to the discovery of around 1000 presolar silicate grains to date, according to the Presolar Grain Database (Hynes and Gyngard, 2009).

Several methods were developed to isolate presolar grains from their host meteorites (and other extraterrestrial materials). The ‘Chicago Procedure’ is the best known and most commonly used, and involves removing minerals one phase at a time, in a series of increasingly harsh chemical and physical disaggregation steps (Anders and Zinner, 1993; Amari et al., 1994). Whilst the original method utilised HCl and HF to remove the silicates from the meteorite matrix, subsequent studies have used CsF (Nittler and Alexander, 2003). The presolar SiC grains from the residues produced with CsF displayed markedly different $^{12}\text{C}/^{13}\text{C}$ ratios compared to those from Amari et al. (1994)’s residues, suggesting that some SiC populations may be destroyed by HCl-HF (Nittler and Alexander, 2003).

Whilst chemical separation methods are useful in that they provide a nearly pure mineral separate (Amari et al., 1994), there is also evidence to suggest that the harsh acids may damage the surfaces of the grains (Stephan et al., 1997; Henkel et al., 2007a). In particular, Henkel et al. (2007a) noted the loss of inclusions from near the surface of

presolar SiC grains, as well as the increased abundances of Mg, K and Ca at the surface, likely a result of matrix material being deposited in defects from acid etching.

Alternative separation procedures have also been developed, which avoid the use of harsh chemical treatments whilst still increasing the abundance of presolar grains in the mineral separates. Bernatowicz et al. (2003) used both ultrasonification and size separation to produce a fraction with increased abundance of SiC grains (compared to the bulk abundance). A different approach, known as 'gentle separation', was used by Tizard et al. (2005). This method uses freeze-thaw disaggregation to break apart the meteorite before size and density separation is carried out, which increases the presolar SiC abundance by several orders of magnitude (Tizard et al., 2005). With each of these methods, the resulting separates can be mapped with a technique such as EDX on an SEM in order to locate individual SiC grains.

In-situ analysis of presolar grains, particularly using elemental and isotope mapping is currently a very popular technique (Besmehn and Hoppe, 2003; Nittler and Alexander, 2003; Nagashima et al., 2004; Nguyen and Zinner, 2004; Nittler, 2006; Yada et al., 2008; Hoppe et al., 2010; Zinner et al., 2010; Hoppe et al., 2012; Leitner et al., 2012; Leitner et al., 2016; Groopman and Nittler, 2018; Hoppe et al., 2018) as it eliminates the need for extracting grains with harsh chemical treatments. However, locating some presolar grains types (SiC, oxides, graphites etc.) is more time-consuming compared with analysing acid residues. The majority of material in a polished meteorite section has a solar system origin, with presolar grains found in very low abundances.

2.2.5 Analysis

Despite their small size, presolar grains have been analysed with a wide range of techniques in order to determine their elemental and isotopic compositions, as well as their internal structure and morphology. Isotope ratios are the most important measurements as these provide information on a grain's stellar origin, and complement astronomical observations and models.

Analyses have been carried out for both bulk samples and individual grains. Bulk analysis is useful for grains which are too small for individual analysis (such as presolar nanodiamonds) or for measuring trace elements which are present in low abundances.

However, as bulk analysis can only determine average isotope ratios, and therefore cannot be used to determine a grain's source, the analyses of individual grains is preferred.

Individual presolar grains have been analysed with a wide range of techniques, including SIMS (Secondary Ion Mass Spectrometry), RIMS (Resonance Ionization Mass Spectrometry), SEM (Scanning Electron Microscopy), TEM (Transmission Electron Microscopy), and more recently, APT (Atom Probe Tomography).

SIMS is the most widely used technique for determining the isotopic composition of presolar grains, and has been extensively used in the discovery of presolar oxides, silicon nitride, silicates and rare SiC sub-groups (Amari et al., 1992; Nittler et al., 1994; Nittler et al., 1995; Nittler et al., 1997; Messenger et al., 2003; Nagashima et al., 2004; Nguyen and Zinner, 2004; Yada et al., 2008; Nguyen et al., 2014). Early work used relatively low resolution SIMS instruments, such as the Cameca IMS-3f, -6f, and -1270. The Cameca NanoSIMS is now the most widely used instrument, as its high spatial resolution has allowed grains down to ~100 nm to be analysed. It has proven particularly useful for identifying new, rare presolar grain types (such as silicates, oxides, and rare SiC sub-groups), as large areas of a sample can be automatically searched. Whilst the NanoSIMS is capable of achieving good mass and spatial resolution, it is not without its limitations. The technique is destructive, and only able to measure 5-7 ionic species at once, which limits analyses to the major elements, or means larger (>1 μm) grains are required for trace element analysis, resulting in a size bias to the data. Although it has not been used extensively in presolar grain research, TOF-SIMS (Time-of-Flight Secondary Ion Mass Spectrometry) offers a way around this, as it can analyse the entire mass spectrum in a single measurement, meaning the isotopic composition of both major and trace elements can be determined (Stephan and Jessberger, 1996; Stephan et al., 1997). The technique uses a pulsed primary ion beam, which allows isotope and element depth profiles to be determined (Lyon et al., 2007; King et al., 2012). However, TOF-SIMS also has its drawbacks- although the entire mass spectrum can be analysed, the low signal rate of the technique means that the precision and mass resolution is lower than conventional SIMS techniques. Additionally, the spatial resolution is typically lower than that of the NanoSIMS (depending on the primary ion source), preventing small presolar grains from being analysed.

RIMS has been widely used to measure heavy elements in individual presolar grains. Heavy elements are of particular importance in presolar grain research as they provide information on s- and r-process nucleosynthesis in stars. The technique uses lasers to resonantly ionise specific element(s), which increases sensitivity, and avoids issues with isobaric interferences- a common issue with heavy element analysis. A new RIMS instrument, CHILI (Chicago Instrument for Laser Ionization), has recently been developed specifically for presolar grain research (Stephan et al., 2016b), and has so far been used to analyse the isotopic composition of Fe, Ni, Sr, Zr, Mo and Ba in presolar SiC grains (Davis et al., 2015; Stephan et al., 2015a; Stephan et al., 2015b; Stephan et al., 2016a; Trappitsch et al., 2016a; Trappitsch et al., 2016b; Stephan et al., 2017).

TEM has proven to be a valuable method for understanding the internal structure of presolar grains, and has led to the discovery of many sub-grains within SiC and graphite grains (Bernatowicz et al., 1991; Croat et al., 2003; Croat et al., 2010; Croat et al., 2011a, b), including TiC, kamacite, rutile and cohenite. The technique is particularly useful for determining the crystal structure and interior morphology of grains (Bernatowicz et al., 1991; Bernatowicz et al., 1996; Daulton et al., 2002, 2003; Daulton et al., 2009; Kodolányi et al., 2016; Stroud et al., 2017; Groopman and Nittler, 2018).

A promising technique for the future is APT (Heck et al., 2014), which is able to identify individual atoms and their location within small samples (Heck et al., 2010; Lewis et al., 2014b). To date, the atom probe has predominantly been used to analyse nanodiamonds- grains which have previously only be measured in bulk due to their small size (Heck et al., 2010; Stadermann et al., 2010; Heck et al., 2011a; Heck et al., 2011b; Heck et al., 2011c; Stadermann et al., 2011; Heck et al., 2012; Heck et al., 2014; Lewis et al., 2014a; Lewis et al., 2015; Lewis et al., 2016; Lewis et al., 2017), although some analyses have been carried out on presolar SiC grains (Heck et al., 2010; Stadermann et al., 2010; Stadermann et al., 2011; Lewis et al., 2014b). Although promising, the technique has its drawbacks, as the measurement times are much longer than other techniques, and it can presently only analyse samples <100 nm in size (Cerezo et al., 2007; Heck et al., 2014; Lewis et al., 2014a; Lewis et al., 2014b).

2.3 Presolar SiC

Presolar silicon carbide grains have been identified in nearly all primitive chondrite classes, in abundances up to ~150 ppm (Huss and Lewis, 1995; Lodders and Amari, 2005; Floss and Stadermann, 2009; Zhao et al., 2011; Leitner et al., 2012). Most presolar SiC grains are <0.5 μm in size, but rare grains up to 50 μm have been identified (Amari et al., 1994). Presolar SiC grains were discovered in 1987 due to the exotic noble gas components which they carry- Xe-S, Kr-S and Ne-E(H) (Bernatowicz et al., 1987; Lewis et al., 1990).

SiC grains are the best studied presolar grains, with over 17000 grains analysed to date (Hynes and Gyngard, 2009). SiC grains are relatively large compared to other presolar grain types, are relatively abundant (up to 150 ppm, although typically <50 ppm), and contain high abundances of trace elements.

2.3.1 Presolar SiC Sub-Groups

Presolar SiC grains are classified into several sub-groups based upon their $^{12}\text{C}/^{13}\text{C}$, $^{14}\text{N}/^{15}\text{N}$, $\delta^{29,30}\text{Si}$, and initial $^{26}\text{Al}/^{27}\text{Al}$ ratios, which vary by several orders of magnitude relative to solar compositions (Figures 2.6, 2.7, and 2.8), with each sub-group related to a different stellar source.

2.3.1.1 Mainstream Grains

Mainstream grains, around 90% of all presolar SiC grains, are defined as having $^{12}\text{C}/^{13}\text{C}$ ratios between 10 and 100, with over 70% of grains being sub-solar in composition (Hynes and Gyngard, 2009). Many mainstream grains are depleted in ^{15}N ($^{14}\text{N}/^{15}\text{N} = 50\text{--}19,000$), ^{29}Si ($\delta^{29}\text{Si} = -210$ to $+330$), and ^{30}Si ($\delta^{30}\text{Si} = -180$ to $+240$) (Hoppe et al., 1994; Lugaro et al., 1999; Hynes and Gyngard, 2009).

The isotopic composition of C and N, as well as s-process enrichments in many other elements, suggests that mainstream grains formed around 1-3 M_{\odot} AGB stars of ~solar metallicity (Iben and Renzini, 1983; Hoppe and Ott, 1997; Nicolussi et al., 1997; Nicolussi et al., 1998; Lugaro et al., 2003). In contrast, the enrichments in ^{29}Si and ^{30}Si appear to disagree with this assessment. Models of Galactic Chemical Evolution suggest that $^{30}\text{Si}/^{28}\text{Si}$ and $^{29}\text{Si}/^{28}\text{Si}$ should increase over time (Clayton, 1988; Gallino et al., 1994; Timmes and Clayton, 1996; Clayton and Timmes, 1997), meaning presolar grains (which

formed before the solar system, should be depleted in these isotopes, relative to solar compositions. It is possible that either our Sun has an atypical Si isotope composition (Alexander and Nittler, 1999), or chemical evolution may be heterogeneous across the interstellar medium (Lugaro et al., 1999).

2.3.1.2 Type AB Grains

Around 3-4% of presolar SiC grains are type AB, and are characterised by their extreme enrichments in ^{13}C , with $^{12}\text{C}/^{13}\text{C} < 10$. Many AB grains have extremely low $^{14}\text{N}/^{15}\text{N}$ ratios, with many grains sub-solar in composition (Hoppe et al., 1995; Hoppe et al., 1996a; Huss et al., 1997; Amari et al., 2001c; Nittler and Alexander, 2003; Hynes and Gyngard, 2009), which cannot be explained by astrophysical models (Huss et al., 1997; Amari et al., 2001c; Hedrosa et al., 2013; Zinner, 2014; Pignatari et al., 2015). Type AB grains have similar Si isotopic compositions to mainstream grains, with many showing enrichments in both ^{29}Si and ^{30}Si (Figure 2.7), but typically show enrichments in ^{26}Al relative to mainstream grains (Figure 2.8).

The unusual isotopic composition of AB grains means that their stellar origin is not well known or understood. Their extremely low $^{12}\text{C}/^{13}\text{C}$ ratios, combined with their formation around a C-rich star, suggests that the parent star must have experienced He-burning followed by limited H-burning. The astrophysical environment for this process is not well known. A recent study by Pignatari et al. (2015) suggested that these conditions could occur in a core collapse supernovae, where the shockwave hits the He-shell whilst some H is still present.

Around two thirds of AB grains have enrichments in their trace elements which are characteristic of s-process nucleosynthesis (Amari et al., 1995). It has been suggested that these grains could have condensed around post-AGB stars which experienced a late thermal pulse (Asplund et al., 1998; Herwig, 2001; Herwig et al., 2011), as these stars show enrichments in ^{13}C and many s-process elements, although they cannot explain the low $^{14}\text{N}/^{15}\text{N}$ ratios.

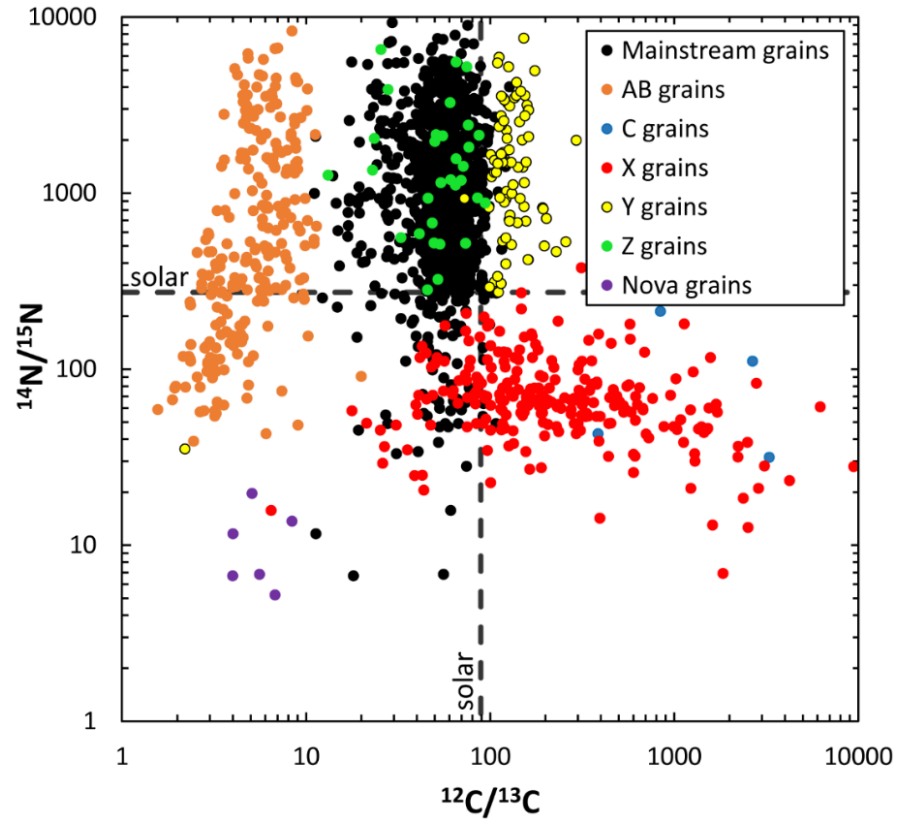


Figure 2.6: Plot showing the variation in $^{12}\text{C}/^{13}\text{C}$ and $^{14}\text{N}/^{15}\text{N}$ in presolar SiC sub-groups.

Data are from the Presolar Grain Database (Hynes and Gyngard, 2009).

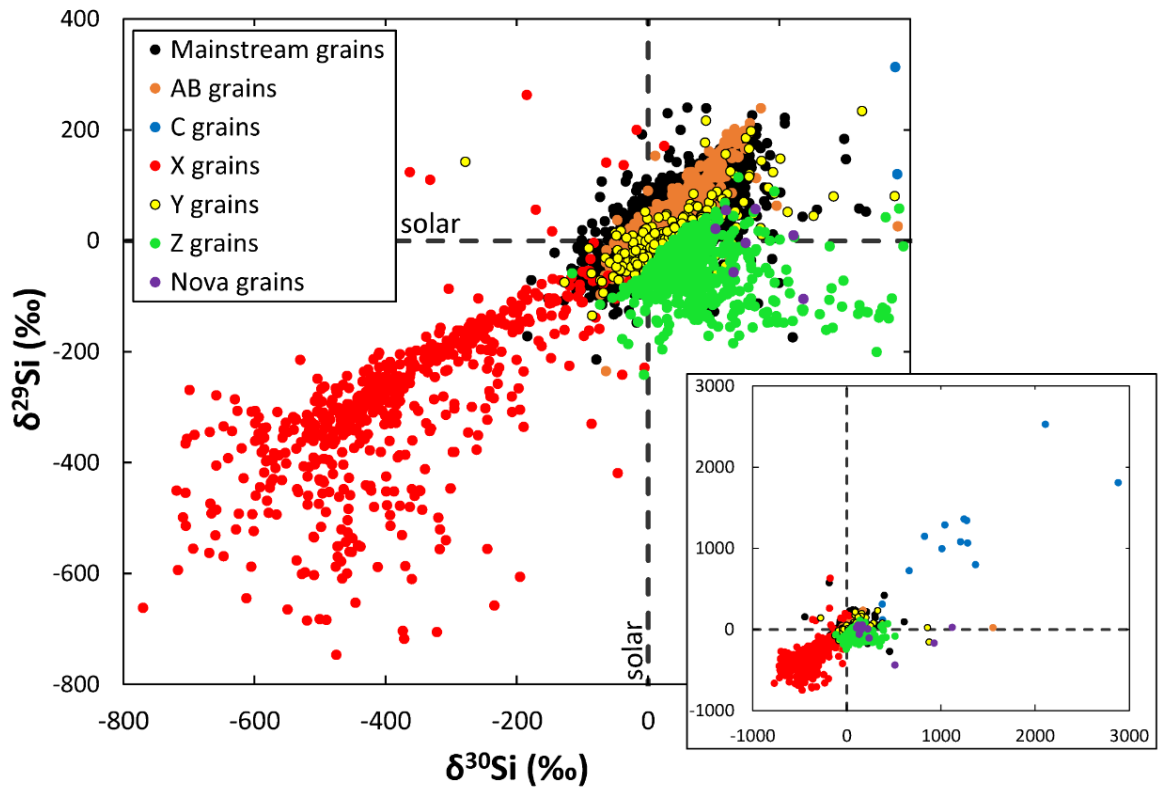


Figure 2.7: Variation in $\delta^{29}\text{Si}$ and $\delta^{30}\text{Si}$ in presolar SiC sub-groups. The inset shows the extreme $\delta^{29}\text{Si}$ and $\delta^{30}\text{Si}$ ratios of the nova grains. The dashed lines illustrate the solar $\delta^{29}\text{Si}$ and $\delta^{30}\text{Si}$ ratios. Data are from the Presolar Grain Database (Hynes and Gyngard, 2009).

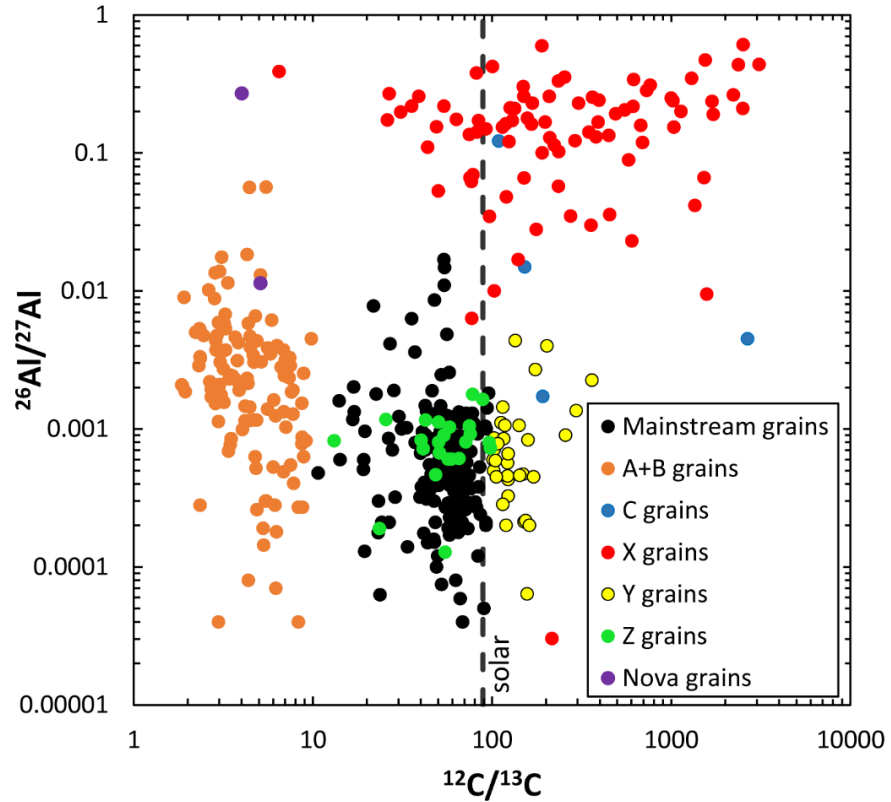


Figure 2.8: Plot showing the variation in $^{26}\text{Al}/^{27}\text{Al}$ and $^{12}\text{C}/^{13}\text{C}$ in presolar SiC sub-groups. The dashed line indicates the solar $^{12}\text{C}/^{13}\text{C}$ ratio. Data are from the Presolar Grain Database (Hynes and Gyngard, 2009).

The remaining 1/3 of AB grains show no s-process enrichments in their trace elements (Amari et al., 1995; Pellin et al., 2000; Savina et al., 2003; Nguyen et al., 2018). It has been suggested that they may originate from J-type stars with low $^{12}\text{C}/^{13}\text{C}$ ratios (Lambert et al., 1986), however models suggest that these stars cannot account for AB grains which have both low $^{12}\text{C}/^{13}\text{C}$ and low $^{14}\text{N}/^{15}\text{N}$ ratios.

2.3.1.3 Type C Grains

Type C grains are rare, making up only 1% of all presolar SiC grains (Hynes and Gyngard, 2009), and are characterised by large ^{29}Si and ^{30}Si excesses. Additionally, many grains are enriched in ^{12}C and ^{15}N relative to solar compositions (Figure 2.6). As a relatively recent discovery (Croat et al., 2010), very few type C grains have been discovered to date, of which only a handful have been analysed for their trace elements (Hynes and Gyngard, 2009). Of those which have been analysed, several show evidence for initial enrichments in the short-lived isotopes ^{26}Al and ^{44}Ti (Hoppe et al., 2012). All of these isotopic characteristics suggest that type C grains condensed from supernova ejecta.

Six type C presolar SiC grains have large ^{32}S excesses (Hoppe et al., 2012)- in supernovae, only the Si/S zone produces a ^{32}S excess, but this would also result in ^{28}Si excesses. However, many studies have not taken explosive burning into account when modelling nucleosynthesis in supernovae. A recent study by Pignatari et al. (2013b), which included explosive burning calculations in the simulation, suggested that the ^{32}S excesses could result from the decay of short-lived ^{32}Si , which is formed by r-process nucleosynthesis in the He/C zone of supernovae. ^{32}Si builds up in this zone as the neutron-capture rate to form ^{33}Si is very low during explosive burning.

2.3.1.4 Type X Grains

Type X grains, around 1% of presolar SiC, are characterised by ^{12}C , ^{15}N and ^{28}Si excesses (Amari et al., 1992; Hoppe et al., 1996b, 2000). Additionally, X grains also have the highest $^{26}\text{Al}/^{27}\text{Al}$ ratios out of all presolar SiC grains (Figure 2.8).

Many type X grains show variations in their Ti abundance with depth, suggesting the presence of Ti-rich sub-grains, likely to be TiC, which is expected to condense in similar conditions to SiC (Lodders and Fegley, 1995; Besmehn and Hoppe, 2003; Lin et al., 2010). Many type X grains contain elevated abundances of ^{44}Ca , from the decay of ^{44}Ti (Amari et al., 1992; Hoppe et al., 1996b; Nittler et al., 1996; Hoppe et al., 2000; Besmehn and Hoppe, 2003; Lin et al., 2010), whilst ^{49}Ti excesses result from the decay of ^{49}V (Amari et al., 1992; Nittler et al., 1996; Hoppe and Besmehn, 2002; Lin et al., 2010). Both ^{44}Ti and ^{49}V are only thought to form in supernovae (Timmes et al., 1996), suggesting the X grains condense in the ejecta of these stellar explosions.

Type II supernovae are the most likely source, matching the high $^{12}\text{C}/^{13}\text{C}$, low $^{14}\text{N}/^{15}\text{N}$ and high $^{26}\text{Al}/^{27}\text{Al}$ compositions, whilst also producing ^{44}Ti and ^{49}V . However, material from both the interior and exterior zones of the supernova would have to be mixed to fulfil all of these criteria, which would require deep, inhomogeneous mixing. As C/O must be >1 for carbonaceous grains to condense (Larimer and Bartholomay, 1979; Lodders and Fegley, 1995), this scenario also requires limited input from the intermediate, O-rich zones of the supernova. Astronomical observations suggest this is possible (Ebisuzaki and Shibasaki, 1988; Hughes et al., 1999; Kifonidis et al., 2003), but it is unclear whether this can happen on a microscopic scale.

The heavy elements in X grains show enrichments which fall short of matching r-process nucleosynthesis, but can be explained by a neutron burst (Meyer and Clayton, 2000). An intense neutron burst is predicted to occur in the O/C zone of Type II supernovae (Rauscher et al., 2002), which could explain these heavy element compositions. Alternatively, it has been suggested by Pignatari et al. (2013a) that the isotopic compositions of the X grains can be matched by nucleosynthesis in the He-burning C/Si shell of a core-collapse supernova. Unlike earlier models, those used by Pignatari et al. (2013a) include calculations of explosive burning, meaning grains with previously unexplained origins can now be accounted for.

2.3.1.5 Type Y Grains

Type Y presolar SiC grains are characterised by $^{12}\text{C}/^{13}\text{C} > 100$, and greater than solar $^{14}\text{N}/^{15}\text{N}$ compositions (Amari et al., 2001b). On a three-isotope plot of Si, Y grains plot slightly to the right of the line defined by mainstream grains (Figure 2.7) (Hoppe et al., 1994; Amari et al., 2001b; Nittler and Alexander, 2003).

Comparisons of their C, Si, and Ti isotopic compositions with stellar models suggests that Y grains formed in low- to intermediate-mass AGB stars, with a metallicity around half that of the Sun (Amari et al., 2001b). These stars dredge up higher abundances of ^{12}C , along with neutron-capture Si and Ti, from the He-burning shell (Lugaro et al., 1999).

2.3.1.6 Type Z Grains

Type Z grains have $^{12}\text{C}/^{13}\text{C} < 100$ and have greater than solar $^{14}\text{N}/^{15}\text{N}$ (Alexander, 1993; Hoppe et al., 1997; Nittler and Alexander, 2003). They have larger ^{30}Si excesses relative to ^{29}Si , indicating formation in low mass AGB stars with a metallicity $\sim 1/3$ solar (Hoppe et al., 1997).

Depletions in ^{46}Ti , ^{47}Ti and ^{49}Ti , relative to ^{48}Ti , are correlated with ^{29}Si depletions, as is expected for low mass AGB stars (Amari et al., 2005; Zinner et al., 2007). Additionally, excesses in ^{30}Si and ^{50}Ti are explained by neutron-capture nucleosynthesis, which is stronger in low metallicity AGB stars (Zinner et al., 2006; Zinner et al., 2007). The low C ratio of Z grains indicates that the parent star underwent cool-bottom processing (Wasserburg et al., 1995; Nollett et al., 2003; Karakas et al., 2010) during its RGB and AGB phases (Nittler et al., 2005a; Zinner et al., 2006).

2.3.1.7 Nova Grains

Several unusual presolar SiC grains have also been discovered, with low $^{12}\text{C}/^{13}\text{C}$ and $^{14}\text{N}/^{15}\text{N}$ ratios (both <20), large ^{30}Si excesses, and high inferred $^{26}\text{Al}/^{27}\text{Al}$ ratios. These compositions are expected to be produced by explosive, high temperature hydrogen-burning in novae (Kovetz and Prialnik, 1997; Starrfield et al., 1998; José et al., 1999; José et al., 2003; José et al., 2004; José and Hernanz, 2007). However, models predict much larger anomalies than are found in SiC nova grains, suggesting the ejecta was mixed with another component, closer to solar in composition (Amari et al., 2001a; José and Hernanz, 2007). Recent studies have suggested that several of the ‘nova’ grains can instead be explained by formation in the ejecta of core collapse supernovae which experienced explosive H-burning (Pignatari et al., 2015; Liu et al., 2016).

2.3.2 Trace Elements

Many trace elements are highly abundant in presolar SiC grains, making SiC popular for analysis. The abundances and isotopic compositions of trace elements in these grains is a reflection of the condensation process, the composition of the parent star’s envelope, and implantation in the interstellar medium.

As predicted by models (Lodders and Fegley, 1995, 1997, 1999), refractory trace elements such as Al, Ti, V and Zr, are enriched in presolar SiC grains (Amari et al., 1995), whilst volatile elements are depleted.

Some refractory phases, such as TiC, condense at similar temperatures to SiC (Lodders and Fegley, 1995). As they condense, the composition of the stellar envelope changes, which causes elements to become depleted in SiC grains. These grains may also be incorporated into the SiC grains, with many refractory sub-grains having been identified (Bernatowicz et al., 1992; Stroud and Bernatowicz, 2005; Hynes et al., 2010).

Some trace elements show enrichments in SiC grains due to implantation of atoms/ions in the interstellar medium, likely by supernova shockwaves. Shockwaves can accelerate material up to 1000 km/s (Jones et al., 1997), causing material to be implanted into dust grains when they collide. Due to the small size of presolar grains, it is thought that implantation may play a much greater role in determining the abundances of trace elements than the condensation process (Verchovsky et al., 2003; Verchovsky et al.,

2004). Elevated abundances of Li and B have been identified in the surfaces of presolar SiC grains (Lyon et al., 2007), whilst the isotopic composition of noble gases is seen to vary with grain size, as a result of implantation (Verchovsky et al., 2004).

Due to their low abundances, and the small size of presolar SiC grains, the measurement of trace elements is limited by analytical capability. As a result, there is a size bias to the available data, with the largest SiC grains selected for analysis. Many techniques are also unable to identify the presence of sub-grains in presolar SiC, meaning only bulk trace element abundances can be determined.

2.3.3 Morphology

The majority of presolar SiC grains are euhedral- over 80% are cubic (polytype 3C), 3% are hexagonal (polytype 2H), and the remaining ~17% are intergrowths between the two structures (Daulton et al., 2002; Bernatowicz et al., 2003; Daulton et al., 2003). Terrestrial SiC grains have over 250 known polytypes, suggesting that presolar SiC grains form in a limited range of conditions. The 3C and 2H polytypes are almost non-existent in terrestrial SiC grains as the formation conditions do not typically occur. The 3C and 2H polytypes require low temperatures (<1633 K), low pressures ($<10^{-4}$ bar), and $C/O > 1.05$ (Daulton et al., 2002, 2003), which is predicted to occur in the stellar outflows of C-rich AGB stars.

Over 60% of pristine presolar SiC grains, those separated without the use of harsh chemical treatments, exhibit amorphous coatings on the grain surfaces (Bernatowicz et al., 2003), which could be silica rims, formed by oxidation in the early solar nebula (Mendybaev et al., 2002). Silica rims have also been identified on other presolar SiC grains (Stroud and Bernatowicz, 2005), although as these rims were not amorphous, they may not be comparable. Alternatively, the amorphous coatings could be icy mantles, which were irradiated in the interstellar medium (Messenger et al., 2006; Nuth et al., 2006).

Sub-grains of AlN and TiC have been found in many presolar SiC grains of all sub-groups (Bernatowicz et al., 1992; Stroud and Bernatowicz, 2005; Gyngard et al., 2006; Hynes et al., 2010). It is possible that these sub-grains formed before or at the same time as SiC (Lodders and Fegley, 1995), although TiC could form by exsolution.

Chapter 3

Experimental Methods

Presolar silicon carbide grains from three meteorites were analysed during this project, using a range of analytical techniques. The majority of analyses were carried out using the NanoSIMS, whilst the TOF-SIMS and SEM provided supplementary data.

3.1 Sample Preparation

Three sample preparation techniques were used during this project, with each detailed below. Presolar SiC grains from the acid residues and polished sections were identified and analysed, whilst no gently separated grains were identified due to experimental issues.

3.1.1 Gently Separated Grains

Two meteorites, Murchison (CM2 chondrite) and GRA 95229 (CR2 chondrite) were processed using a modified 'gentle separation' procedure (Tizard et al., 2005), in order to isolate and identify presolar silicon carbide grains for analysis. Murchison (sample number Murchison 1970-6) was selected for this study as material was readily available, and gently separated grains from Murchison had previously been analysed (Lyon et al., 2007). GRA 95229 (sample number GRA 95229,94) was selected due to the high reported abundance (~55 ppm) of presolar silicon carbide grains (Davidson et al., 2009), and was provided by the Meteorite Working Group, which distributes Antarctic meteorites collected by the ANSMET (Antarctic Search for Meteorites) program.

Small chips of each meteorite, 130 mg of Murchison and 110 mg of GRA 95229, were crushed using a stainless steel pestle and mortar. The mortar was sealed with Teflon tape (see Figure 3.1) in order to prevent any fine dust from escaping during the crushing process. Once crushed, the powder was added to 2 cm³ deionised water in a stainless steel tube. The material was dispersed by ultrasonification for 10 minutes.

The crushed material was broken up into individual grains by freeze-thaw disaggregation. The stainless steel tube, containing the sample/water mixture, was alternately dipped

into liquid nitrogen ($\sim -195^{\circ}\text{C}$) and warm water ($\sim 60^{\circ}\text{C}$) for two minutes each. The water was kept at a constant temperature on a hot plate to ensure the sample completely thawed during each cycle.



Figure 3.1: The stainless steel pestle and mortar used to crush each meteorite chip prior to freeze-thaw disaggregation. The mortar consists of two pieces, which were sealed with Teflon tape to ensure no fine dust could escape.

After 300 cycles, an aliquot of the sample was extracted and distributed onto a piece of gold foil. The grains were examined on an Environmental Scanning Electron Microscope (ESEM) to determine the progress of the disaggregation. Secondary Electron (SE) images were used to identify any grain clusters, whilst EDX (Energy Dispersive X-Ray) spot analyses were used to determine if large grains had varying elemental compositions, which would suggest they were grain aggregates. During this analysis, several large grains with heterogeneous compositions were identified, meaning disaggregation had not yet been successful. A further 50 freeze-thaw cycles were carried out before another aliquot was examined using the ESEM. After a total of 350 cycles, it was determined that no grain aggregates remained.

Following disaggregation, the grain/water mixture was split into two centrifuge tubes, with isopropanol added to each to form a 1:1 water-isopropanol mixture. The grains were dispersed throughout the liquid by ultrasonification for 5 minutes. The grains were

separated into three size fractions- $<1\ \mu\text{m}$, $1\text{-}20\ \mu\text{m}$, and $>20\ \mu\text{m}$. These fractions were selected as presolar SiC grains over $20\ \mu\text{m}$ are rare, and those smaller than $1\ \mu\text{m}$ are too small for analysis with TOF-SIMS (Time-of-Flight Secondary Ion Mass Spectrometry).

Sedimentation rates, SR , for the two largest fractions ($1\text{-}20\ \mu\text{m}$ and $>20\ \mu\text{m}$) were calculated using Stokes' Law (see equation 3.1). Presolar SiC grains have a limited density range of $3.1\text{-}3.2\ \text{gcm}^{-3}$, so an average grain density, ρ_g , of $3.15\ \text{gcm}^{-3}$ was used in the calculations. Other variables include the grain diameter, d ($1\ \mu\text{m}$ and $20\ \mu\text{m}$), solution density, ρ_s ($0.85\ \text{gcm}^{-3}$), and solution viscosity, ν_s ($0.0038\ \text{Nsm}^{-2}$).

$$SR = \frac{gd^2(\rho_g - \rho_s)}{18\nu_s} \quad (3.1)$$

As small grains near the bottom of the centrifuge tube may settle at the same time as large grains from the top of the tube, each step was repeated 5 times in order to sharpen the fraction boundaries (see Figure 3.2). The settling time, t , for each fraction was calculated based upon 50% of grains at the lower boundary having been sedimented after 5 repeats (see equation 3.2). The settling times for the $<1\ \mu\text{m}$ and $1\text{-}20\ \mu\text{m}$ fractions were unreasonably long, so a fixed-angle rotor centrifuge was used to reduce the settling times of the $1\text{-}20\ \mu\text{m}$ fraction, whilst the $<1\ \mu\text{m}$ fraction was left to settle in the laboratory, as it would not be used for analysis. The settling times and g-forces used are detailed in Table 3.1.

$$0.5 = \left(\frac{SR \cdot t}{h} \right)^5 \quad (3.2)$$

Following size separation, the $1\text{-}20\ \mu\text{m}$ fraction was sub-divided into three density fractions of $<3.05\ \text{gcm}^{-3}$, $3.05\text{-}3.24\ \text{gcm}^{-3}$, and $>3.24\ \text{gcm}^{-3}$. These boundaries were selected as presolar SiC grains have a limited density range of $3.1\text{-}3.2\ \text{gcm}^{-3}$, meaning they can be concentrated into one fraction whilst removing many of the silicate minerals which make up the bulk of meteorite matrix material.

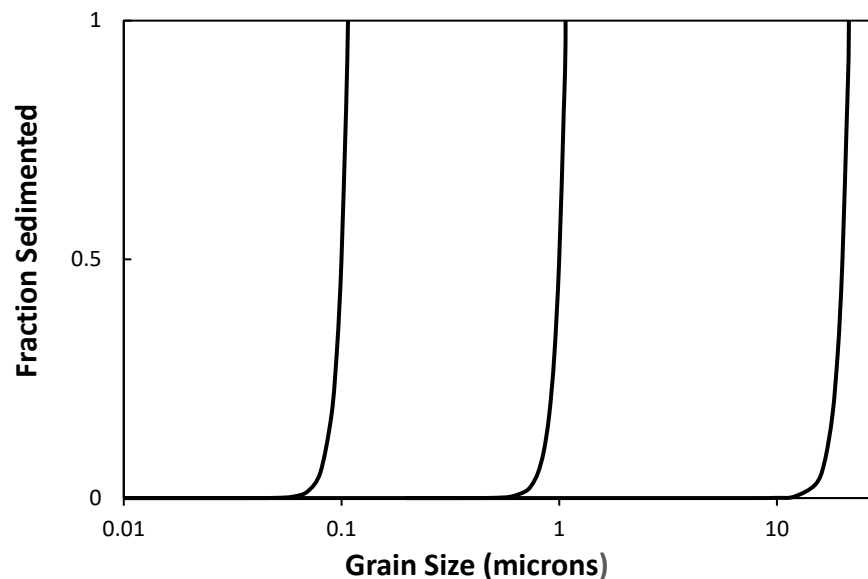


Figure 3.2: The expected size distributions of each fraction following size separation, as calculated using Stokes' Law.

Fraction	G-Force, g	Settling Time, t
>20 μm	1 g	198 s
1-20 μm	131 g	604 s
<1 μm	-	Left to settle

Table 3.1: Settling times and g-forces used during the size separation process. The <1 μm fraction was left to settle in the laboratory due to the settling rate being impractically long.

The density separation was carried out using two organic heavy liquids (Cargille Laboratories) with densities of 3.05 and 3.24 gcm^{-3} . As with the size separation, the settling times (Table 3.2) for each density fraction were calculated using Stokes' Law- Figure 3.3 shows the expected size-density distribution of the final fraction. A fixed-angle rotor centrifuge was used to speed up the process, as without it the settling times were impractically long. The 1-20 μm grains were suspended first in $\sim 1 \text{ cm}^3$ of the 3.05 gcm^{-3} liquid and ultrasonicated for 15 minutes to ensure the grains were completely dispersed, before being placed into the centrifuge to allow the grains to settle.

Once the required settling time has elapsed, the sample should consist of a sediment at the base of the tube (grains >3.05 gcm^{-3}), as well as material floating on the surface of the liquid (grains <3.05 gcm^{-3}). The sediment would be removed using a pipette, and the

process would be repeated until no floating grains were present. This final sediment would then be separated using the heavier liquid (3.24 gcm^{-3}) to produce the final fraction of $1\text{-}20 \mu\text{m}$ grains in the $3.05\text{-}3.24 \text{ gcm}^{-3}$ density range.

Organic Heavy Liquid	G-Force, g	Settling Time, t
3.05 gcm^{-3}	3287 g	681 s
3.24 gcm^{-3}	4293 g	1385 s

Table 3.2: Settling times and g-forces used on the $1\text{-}20 \mu\text{m}$ grains during density separation.

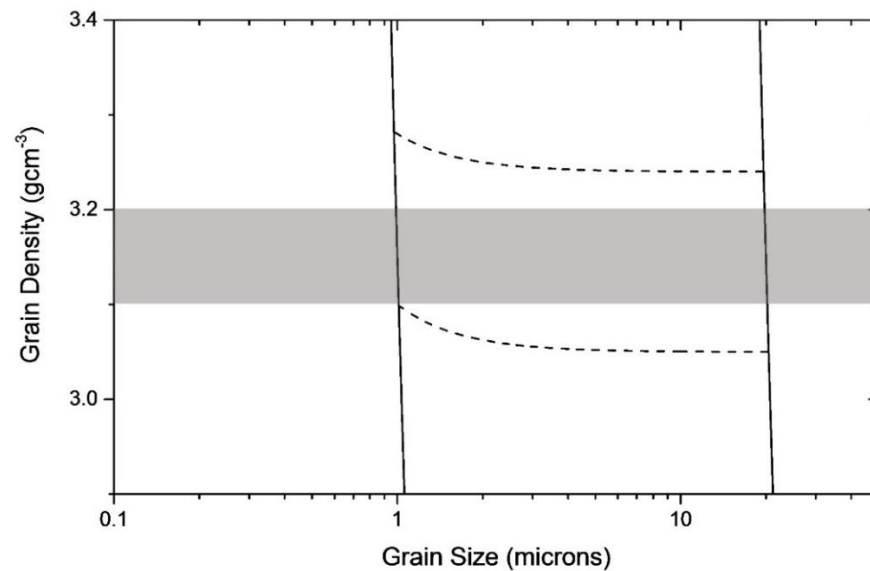


Figure 3.3: Predicted size-density distribution of the $1\text{-}20 \mu\text{m}$ size fraction, once density separation has been completed. The grey region denotes the density range in which presolar SiC grains are found.

However, during the separation process using the 3.05 gcm^{-3} liquid, it was noted that only a small amount of sediment formed at the base of the tube, whilst the majority of the grains were found to be floating at the surface of the liquid. The matrix material of meteorites is predominantly formed of silicates, of which the majority have densities $>3.05 \text{ gcm}^{-3}$, meaning they should not be floating on the liquid surface. Close analysis revealed that the grains at the surface had formed small clumps, and were likely trapping small amounts of either air or isopropanol between them, causing the bulk density of each clump to be less than that of the liquid.

Prior to adding the organic heavy liquid, the 1-20 μm fraction had been dried to remove the remaining water-isopropanol mixture, so as not to affect the density of the liquid during density separation. As the grains dried, it is possible that they stuck together, forming small aggregates. To determine if this was the cause of the clumping, the grains were once again disaggregated using the freeze-thaw process.

The water in which the grains were disaggregated was removed and replaced with acetone, so as to ensure the grains did not dry out. Acetone was selected as the heavy liquid did not mix with either water or isopropanol. The 3.05 g cm^{-3} heavy liquid was added to the grain-acetone mixture, and vigorously ultrasonicated for 30 minutes, to ensure the grains were dispersed. Following separation, the majority of grains were still found floating on the surface of the heavy liquid, though the aggregates were smaller than the previous attempt. The method was repeated several times, each producing similar results. Consequently, the density separation was abandoned, and a decision was made to use the bulk 1-20 μm size fraction from GRA 95229.

A small aliquot of the fraction was mixed with a 1:1 mixture of deionised water and isopropanol, and ultrasonicated for 5 minutes to ensure even grain dispersal. The sample, GRA-1 (Figure 3.4), was produced by dispersing a 1 μL drop of the grain solution onto a 7x7 mm piece of high-purity gold foil, which had been imprinted with a finder grid (copper H315, Agar Scientific). The finder grid allows grains to be easily located when being analysed using multiple techniques.

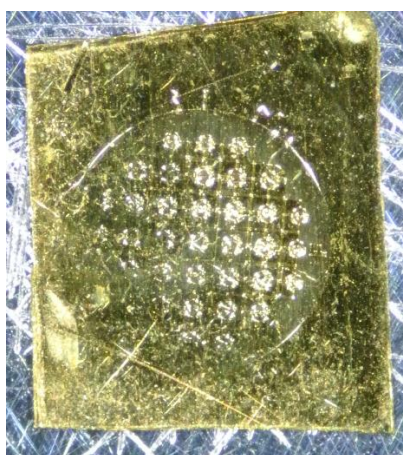


Figure 3.4: Optical image of sample GRA-1, which consists of grains in the 1-20 μm size range from GRA 95229. The finder grid imprint (copper H315, Agar Scientific) allows the grains to be located on multiple instruments.

3.1.2 Acid Residue Grains

Presolar silicon carbide grains were analysed from three different acid residues, KJG, JA-MM and JA-MM2, which were produced from pieces of Murchison meteorite (CM2 chondrite). Each of the residues have slightly different compositions, due to slight differences in the final steps of the methodology.

The KJG residue was produced by following the 'Chicago Procedure', which is detailed in Figure 3.5 (Amari et al., 1994). An 83 g chip of Murchison was treated with HF-HCl in order to dissolve the silicates, which make up the bulk of the meteorite, after which kerogen and sulfur were removed using Cr_2O_7 , KOH and H_2O_2 . A colloid containing nanodiamonds was removed from the residue, which was then separated by size and density to remove graphite. Finally, the material was treated with H_2SO_4 in order to dissolve the spinel and chromite. The final residue, KJ, consisted of a mixture of silicon carbide, hibonite, and corundum. This material was then size separated in order to produce the KJG fraction, containing grains in the 1.5-3 μm size range, of which 73% are silicon carbide grains (Amari et al., 1994).

The KJG residue was provided by Roy Lewis as grains distributed over a 4x4 cm gold foil. From this larger foil, a smaller sample was made for the purpose of this study. RL-1 (see Figure 3.6) was prepared by imprinting a 7x7 mm piece of high-purity gold foil with a finder grid (copper H315, Agar Scientific). This foil was then pressed against the KJG foil in order to transfer grains over to the new sample. The grains were pressed into the foil using a titanium carbide block, in order to prevent them from falling from the mount.

Both JA-MM and JA-MM2 were produced by Russell et al. (1996) following the methodology of Amari et al. (1994). As with the KJG residue, a piece of Murchison was treated with HCl-HF to remove refractory material, before Cr_2O_7 . KOH and K_2O_2 were used to remove kerogen. Nanodiamonds were removed from the sample as a colloid. The JA-MM residue was produced at this stage of the method, meaning it contains spinel and graphite in addition to the SiC, hibonite and corundum that make up the KJG residue. The JA-MM2 residue is more similar to KJG, as it was produced after the Chicago Procedure had been completed, and so comprises of SiC, hibonite and corundum.

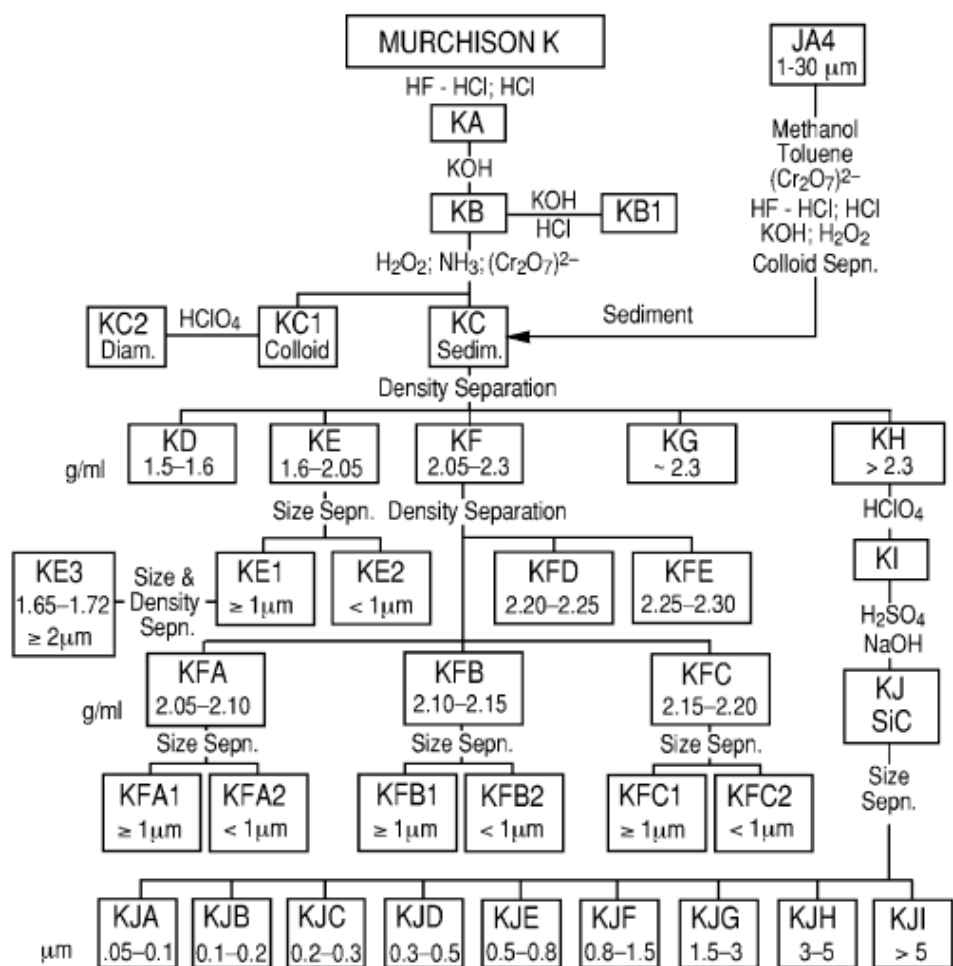


Figure 3.5: Overview of the 'Chicago Procedure' (Amari et al., 1994). The KJG residue, at the bottom of the diagram, comprises of SiC grains in the 1.5-3 μm size range.

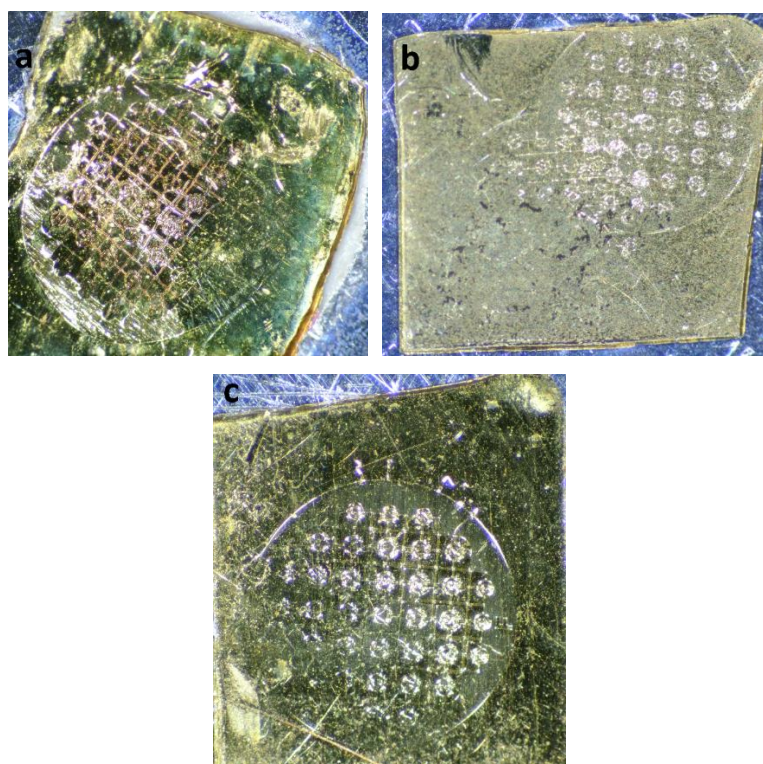


Figure 3.6: Optical images of the acid residue samples: a) RL-1, b) JA-MM, and c) JA-MM2.

Both the JA-MM and JA-MM2 residues were provided by John Arden as powders. A small aliquot of each powder was mixed separately with a 1:1 mixture of isopropanol and deionised water, and ultrasonicated for 5 minutes to disperse the material throughout the liquid. An aliquot ($\sim 1 \mu\text{L}$) of each solution was distributed over separate 7x7 mm pieces of high-purity gold foil, each of which had been imprinted with a finder grid (copper H315, Agar Scientific). A titanium carbide block was used to press the grains of each sample into the gold foil, to ensure they did not fall from the mounts.

3.1.3 In-situ Grains

Presolar silicon carbide grains were analysed in-situ from two polished meteorite sections- Acfer 094 and GRA 95229 (see Figure 3.7). Acfer 094 is an ungrouped type 2 carbonaceous chondrite, and was provided by Addi Bischoff. GRA 95229 (sample number GRA 95229,94) is a CR2 chondrite which was provided by the Meteorite Working Group, who distribute Antarctic meteorites collected by the ANSMET missions.

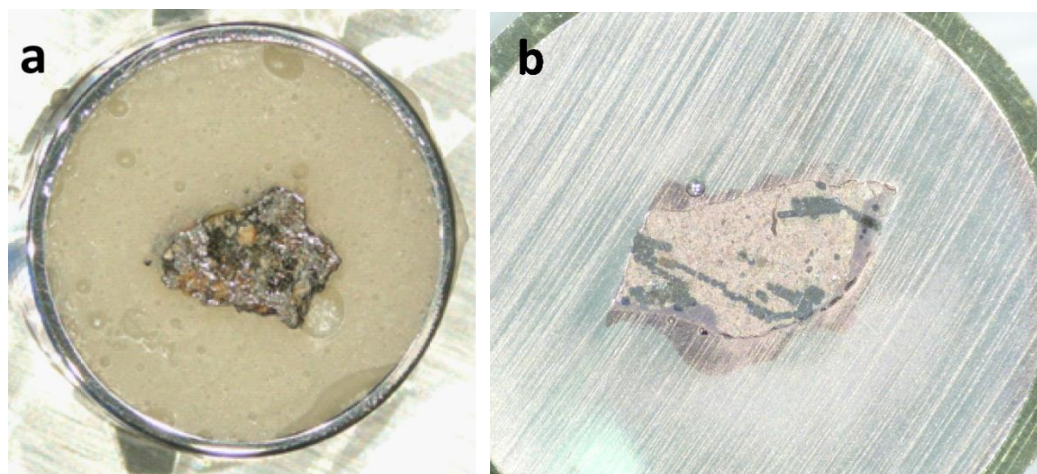


Figure 3.7: Optical images of the a) GRA 95229, and b) Acfer 094 polished sections. Each section sits in a 10 mm stainless steel embedding ring. GRA 95229 was photographed prior to being coated, whilst Acfer 094 was photographed following NanoSIMS analysis.

Small chips of around 200 mg of each meteorite were set into 10 mm embedding rings using epoxy resin, which was left to cure for 48 hours. Once solidified, each meteorite was polished with corundum polishing powders ($9 \mu\text{m}$, $5 \mu\text{m}$, $1 \mu\text{m}$ and $0.05 \mu\text{m}$) until a mirror polish was achieved. Corundum powders were used to avoid any potential contamination issues from either silicon carbide or diamond polishing mediums. Each meteorite section was ultrasonicated for 10 minutes in isopropanol between each powder size, in order to prevent any larger grains being left on the surface. Once

polished, the sections were thoroughly cleaned with isopropanol in the ultrasonic bath, before a 10 nm platinum coat was applied to prevent any charging during analyses.

3.2 Scanning Electron Microscopy (SEM)

During this study, many presolar SiC grains were identified using a FEI XL30 ESEM (Environmental SEM) at The University of Manchester, which is equipped with Secondary Electron (SE), Backscattered Electron (BSE), and Energy Dispersive X-ray (EDX) detectors. Large areas of the acid residue samples (JA-MM and KJG) were searched, with each grain subject to an EDX spot analysis. SiC grains were selected on the presence of Si and C peaks, with the absence of all other peaks.

High resolution SE and BSE images were obtained for many of the presolar SiC grains, using either the ESEM, or a Zeiss Sigma SEM in the Photon Science Institute at The University of Manchester.

3.3 Secondary Ion Mass Spectrometry (SIMS)

Throughout this work, presolar SiC grains were extensively analysed using Secondary Ion Mass Spectrometry (SIMS). The technique measures secondary ions which are sputtered from a sample following an impact from primary ions. Two different SIMS instruments were used during this study; high precision isotope ratios were measured using a Cameca NanoSIMS 50L, whilst trace element depth profiles were determined using a Time-of-Flight Secondary Ion Mass Spectrometer (TOF-SIMS).

A beam of high energy primary ions (such as Ar^+ , O^- , Cs^+ , Ga^+ , Au^+ etc) is produced inside an ion gun, and is focused using a series of lenses and apertures. The ions impact the sample, causing positive and negative secondary ions (~1%), secondary neutrals, and secondary electrons to be sputtered. Several processes affect the sputtering of secondary ions at the sample surface, resulting in elemental and isotopic fractionation.

The sputtering of secondary ions is also affected by the matrix effect, which arises as a result of a sample's chemistry. For a particular element, the probability of forming a secondary ion is related to the element's ionisation energy, the chemical composition of the sample and to a lesser extent, the crystallographic structure of the sample. As a

result, some elements ionise more readily, leading to artificially high elemental abundances being determined.

The matrix effect can be corrected for by applying Relative Sensitivity Factors (RSFs) to the measured abundances of each element. RSFs are determined by analysing standards with known compositions, and are quoted relative to a reference element (Si for this work) to account for any differences in the sputter rate which may arise due to the crystallographic structure of a sample. By comparing the measured and known elemental abundances, RSFs can be calculated:

$$RSF_{(E)} = \frac{I(E)/I(E_{ref})}{A(E)/A(E_{ref})}$$

where E is the element of interest, E_{ref} is a reference element (Si for this work), I is the measured secondary ion intensity, and A is the atomic abundance.

As the chemical composition affects the ionisation efficiency of an element, the standards must be similar in composition to the sample (SiC, in the case of this work). SiC standards are rare and only NIST SRM 112b could be acquired for this work, for which the abundances of relatively few elements have been quantified. As a result, eight silicate standards with well quantified elemental abundances (Jochum et al., 2000; Jochum et al., 2006; Jochum et al., 2011) were also analysed: NIST SRM 610/611 (identical compositions provided with different sample thicknesses; 610 was crushed into micron-sized grains for this study, whilst 611 is a polished section), GOR128-G, GOR132-G, T1-G, KL2-G, ML3-B, ATHO-G, and StHs6/80-G. The calculated RSF values used in this work are documented in Table 3.3.

‘Gardening’ effects are produced at the sample surface during the sputtering process. As a primary ion hits the sample, its high energy causes it bury deep into the sample. Secondary ions are produced as a result of collision cascades, with atoms hitting each other until one is ejected from the sample. The collision cascade causes atoms to be ‘turned over’ in the first few atomic layers of a sample, degrading the depth resolution of an analysis.

The sputtering process produces secondary ions with a spread of energies (see Figure 3.8), and therefore a range of velocities. The ions spread out from the sample surface to form a cosine-shaped angular distribution; secondary ions with higher velocities spread out faster than those with lower velocities, moving away from the extraction field. As a result, fewer high-energy ions are detected by the mass spectrometer.

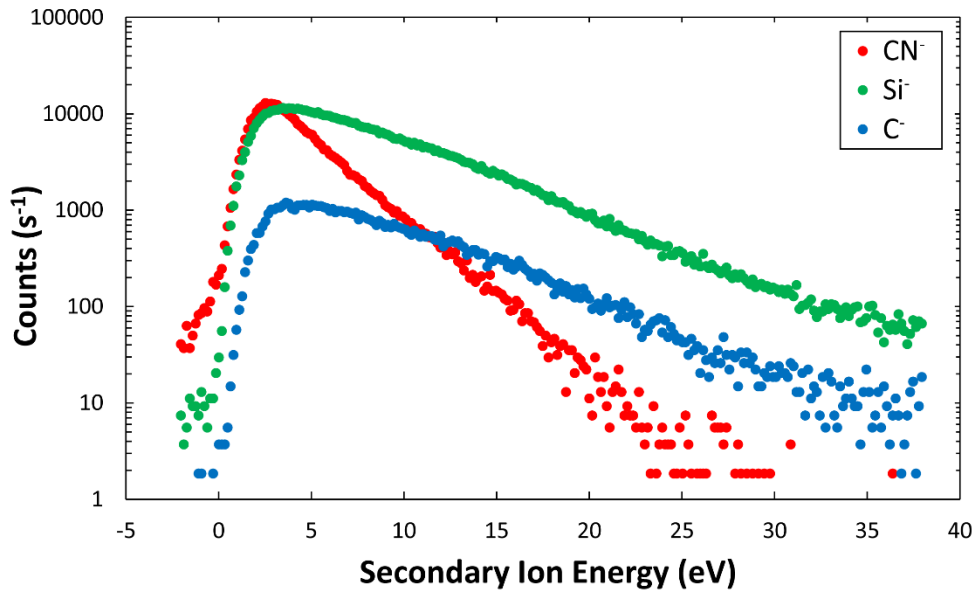


Figure 3.8: Kinetic energy spread of CN^- , Si^- and C^- secondary ions produced during the sputtering process.

Once sputtered, either positive or negative secondary ions are extracted with the use of an electric potential. The ions pass through a mass spectrometer, which uses electrostatic and/or magnetic fields to separate the ions by mass, into a detector where their abundances can be measured.

Instrumental isotopic mass fractionation may also be generated during a SIMS analysis. The fractionation can be quantified by analysing standards, in a similar way to the determination of RSFs, and applied to any measured isotope ratios. As the SiC and silicate standards are terrestrial, their isotope ratios are well known, meaning any deviation can be attributed to instrumental fractionation. The calculated values for instrumental mass fractionation using delayed analysis on the TOF-SIMS are given in Table 3.4 for selected isotope ratios.

Element	Silicate	SiC
Li	4.69	32.8
B	0.26	1.82
C	0.000529	0.0037
O	0.000529	0.0037
Na	13.2	92.1
Mg	7.72	54
Al	7.77	54.4
Si	1	1
K	59.9	419
Ca	12.5	87.3
Ti	7.56	52.9
V	4.9	34.3
Cr	5.86	41.1
Mn	3.85	26.9
Fe	6.17	43.2
Co	1.94	13.6
Ni	1.61	11.3
Cu	2.87	20.1
Rb	27.37	192
Sr	6.06	42.4

Table 3.3: The Relative Sensitivity Factors (RSFs) for selected elements, used in this work. RSFs were calculated by analysing 1 SiC and 8 silicate standards using the TOF-SIMS with delayed extraction.

Isotope Ratio	Instrumental Mass Fractionation
$^6\text{Li}/^7\text{Li}$	-166 ‰
$^{10}\text{B}/^{11}\text{B}$	-79.3 ‰
$^{25}\text{Mg}/^{24}\text{Mg}$	+20.4 ‰
$^{26}\text{Mg}/^{24}\text{Mg}$	-12.4 ‰
$^{29}\text{Si}/^{28}\text{Si}$	+91.7 ‰
$^{30}\text{Si}/^{28}\text{Si}$	-35.2 ‰
$^{42}\text{Ca}/^{40}\text{Ca}$	-48.9 ‰
$^{43}\text{Ca}/^{40}\text{Ca}$	-7.79 ‰
$^{44}\text{Ca}/^{40}\text{Ca}$	-62.2 ‰

Table 3.4: Instrumental mass fractionation values for selected elements. Mass fractionation was determined by analysing 8 silicate standards using the TOF-SIMS with delayed extraction.

3.3.1 NanoSIMS

High precision isotope ratios of carbon, silicon and nitrogen in presolar SiC grains were determined using a Cameca NanoSIMS 50L at The University of Manchester. The NanoSIMS is a commercial instrument and has been widely used in cosmochemistry due to its ability to achieve high spatial resolution, transmission and sensitivity.

The NanoSIMS equipped with two primary ion sources: a Cs^+ microbeam source, which can achieve a spatial resolution of ~ 50 nm (~ 100 nm typically), and an O^- duoplasmatron source, which can produce a spot size of ~ 150 nm (300-500 nm typically). The primary ion beam is passes through a series of apertures, slits and lenses inside the primary ion column (see Figure 3.9), which determine the spot size on the sample surface.

Unlike other SIMS instruments, the NanoSIMS has co-axial primary and secondary ion beams (see Figure 3.9). This enables the instrument to achieve high spatial resolution but means the instrument can only extract secondary ions of the opposite polarity to the primary ions. During this work, Cs^+ primary ions were used, allowing negative secondary ions to be extracted and detected. After being sputtered, the negative secondary ions are extracted by a -8 kV electric potential, before passing into the mass spectrometer.

The NanoSIMS uses a double-focusing magnetic sector mass spectrometer to separate the secondary ions according to their mass, before being detected in the multicollector. The NanoSIMS 50L has 7 detectors, each of which can be operated as either electron multipliers or Faraday cups. Six of the detectors are moveable inside the multicollector, whilst the seventh is fixed.

During this work, two different detector setups were used for the analysis of presolar SiC grains (see Table 3.4). SiC grains from the two polished sections (Acfer 094 and GRA 95229) and two of the acid residues (JA-MM and KJG) were measured using the first configuration, which analysed the atomic ions of carbon ($^{12}\text{C}^-$ and $^{13}\text{C}^-$). Grains from the JA-MM2 residue were analysed with the second configuration (Table 3.5), which was used to detect the molecular ions of C ($^{12}\text{C}_2^-$ and $^{12}\text{C}^{13}\text{C}^-$). This second configuration was selected in order to increase the yield of ^{13}C secondary ions, and is explored in more detail in Chapter 4 of this thesis. Nitrogen does not readily produce an atomic negative

secondary ion, so nitrogen isotopes were determined by analysing CN^- ions ($^{12}\text{C}^{14}\text{N}^-$ and $^{12}\text{C}^{15}\text{N}^-$) in both detector configurations.

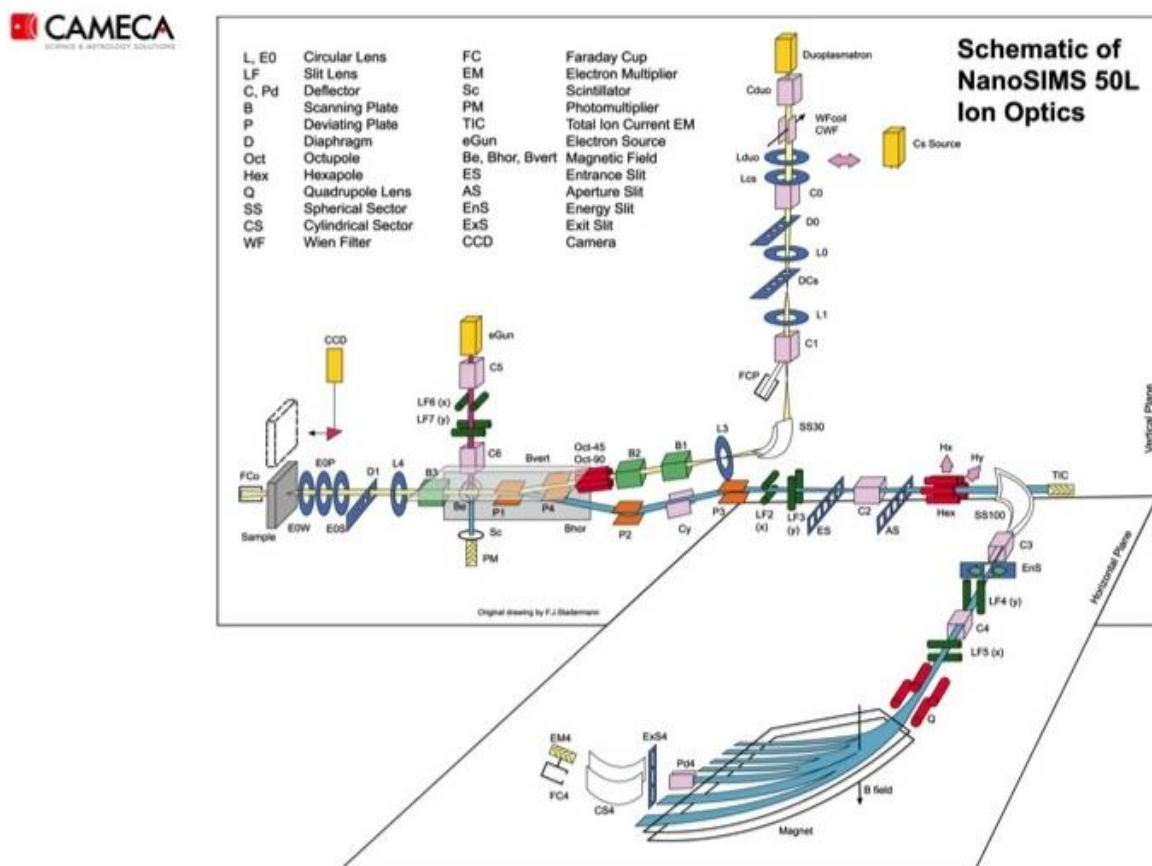


Figure 3.9: Overview of the Cameca NanoSIMS 50L.

Detector	Configuration 1	Configuration 2
	1	2
EM1	$^{12}\text{C}^-$	$^{12}\text{C}_2^-$
EM2	$^{13}\text{C}^-$	$^{12}\text{C}^{13}\text{C}^-$
EM3	$^{12}\text{C}^{14}\text{N}^-$	$^{12}\text{C}^{14}\text{N}^-$
EM4	$^{12}\text{C}^{15}\text{N}^-$	$^{12}\text{C}^{15}\text{N}^-$
EM5	$^{28}\text{Si}^-$	$^{28}\text{Si}^-$
EM6	$^{29}\text{Si}^-$	$^{29}\text{Si}^-$
EM7	$^{30}\text{Si}^-$	$^{30}\text{Si}^-$

Table 3.5: Table showing the two detector configurations used during the analysis of presolar SiC grains. Configuration 1 was used to measure grains from Acfer 094, GRA 95229, KIG and JA-MM, whilst configuration 2 was used to analyse grains from JA-MM2.

Prior to an analysis, samples are pre-sputtered using a high current (~ 1.5 nA) Cs^+ beam, in order to reach a sputtering equilibrium. As Cs^+ ions are implanted in the sample, the work function of the sample surface is reduced, meaning the secondary ion yield increases. The sample is pre-sputtered until a steady-state is reached, ensuring the secondary ion yields (and therefore element and isotope ratios) are stable during a measurement.

During a measurement, the primary ion beam is rastered across the sample to produce secondary ion images for each detector. The NanoSIMS data acquisition software allows the number of frames and pixels of these images to be determined.

NanoSIMS data is processed using the L'Image software (Larry Nittler, Carnegie Institution of Washington). The software allows the individual frames of an analysis to be aligned, in order to correct for the instrumental drift occurs during a measurement. The aligned ion images can be combined to produce isotope ratio images (see Figure 3.10), and Region(s) of Interest (ROIs) can be defined.

As with all SIMS instruments, mass fractionation effects are produced during a measurement. To quantify these effects, terrestrial silicon carbide grains (commonly used as a polishing powder) were periodically analysed. These corrections were then applied to the measured isotope ratios of each sample.

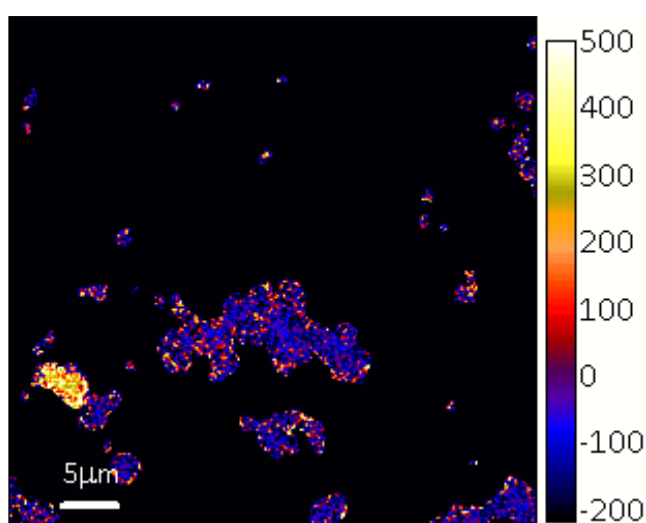


Figure 3.10: Example isotope ratio image produced using L'Image. A presolar SiC grain is identified by its $\delta^{13}\text{C}$ anomaly.

3.3.2 TOF-SIMS

3.3.2.1 Primary Ion Gun

Trace element depth profiles of presolar SiC grain were determined using IDLE-3 (Interstellar Dust Laser Explorer-3), a TOF-SIMS instrument at The University of Manchester (see Figure 3.11) (Henkel et al., 2006; Henkel et al., 2007b). A beam of primary Au^+ ions are produced using a 25 kV Au_n^+ liquid metal ion gun (LMIG), before passing through an aperture (typically 100-200 nm) and a series of lenses, which determine the focus and beam spot size on the sample.

Unlike conventional SIMS instruments, such as the NanoSIMS, TOF-SIMS uses a pulsed primary ion beam which is achieved with the use of two blanking plates inside the ion gun. The pulsing allows the entire mass spectrum to be analysed in a single measurement, but gives the instrument a low duty cycle, meaning analyses must run over several hours to achieve good counting statistics. Pulsing can cause the primary ion beam to move on the sample surface, resulting in lower spatial resolution. 'Minimum motion', whereby the beam movement on the sample is minimised, requires the beam focus to be optimally set between the two blanking plates. Once this has been achieved, the focus on the sample can be adjusted and stigmatism corrections applied. Minimum motion corrections decrease the beam current but return the spatial resolution to that of a DC beam.

3.3.2.2 Secondary Ion Extraction

Secondary ions are extracted from the sample surface by a ± 2 kV electric potential; a positive potential allows positive secondary ions to be extracted, whilst a negative potential allows negatively charged secondary ions to be analysed. The electric potential can be applied either before or after the primary ion beam has impacted the surface, to give either 'normal' or 'delayed' extraction. The use of either normal or delayed extraction affects the mass resolution, $m/\delta m$, which determines the ability to separate two peaks in a mass spectrum. High mass resolution is required in order to distinguish elements and isotopes from other interferences- typically hydrides, hydroxides, hydrocarbons, and isobaric interferences (nuclides of the same mass from different elements).

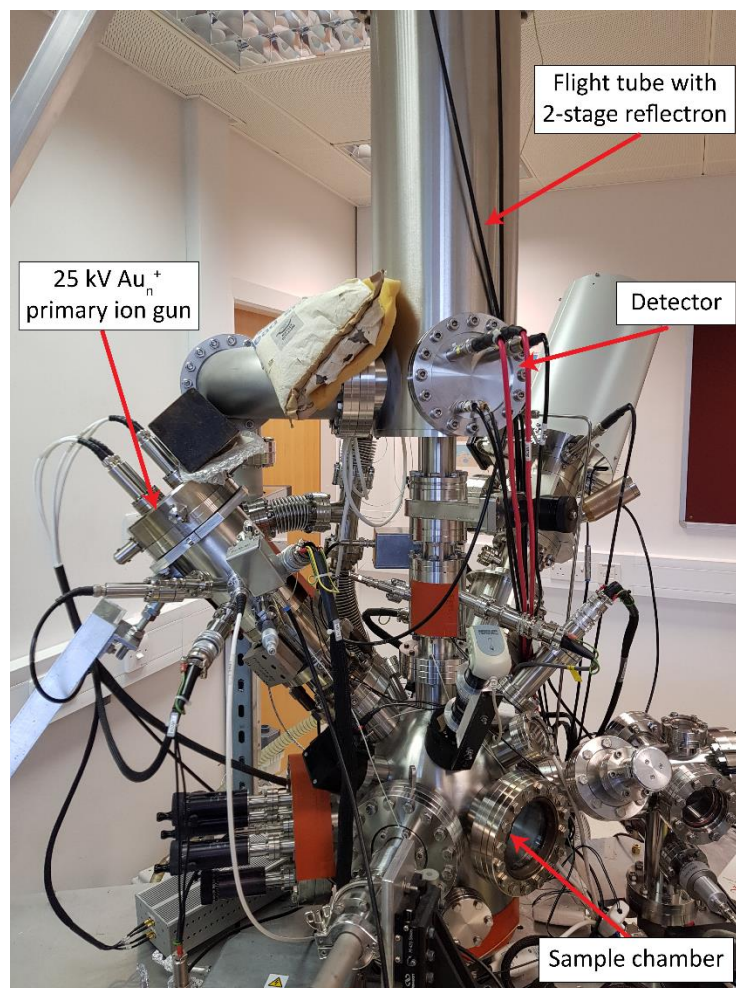


Figure 3.11: Overview of IDLE-3, a TOF-SIMS instrument at The University of Manchester.

During normal extraction, the electric potential on the sample stage is applied before the primary ions hit the sample surface. Throughout the length of the primary ion pulse, any secondary ions are immediately accelerated away from the sample. Secondary ions are produced during the whole length of the pulse, resulting in a large spread in arrival times at the detector, which lowers the mass resolution. The mass resolution can be increased by using shorter primary ion pulse lengths, typically of a few nanoseconds, to reduce the time spread of the secondary ions which are sputtered from the sample. The mass resolution increases with increasing mass, up to a maximum which is determined by the resolution of the detector.

With delayed extraction, the electric potential is switched on after the primary ion beam has hit the sample. Secondary ions which form at the beginning of the pulse move further from the sample than those which form later; when the potential is applied, ions closer to the sample are accelerated more than those which have travelled further. Delayed extraction helps to correct the time distribution of secondary ions, meaning longer

primary ion pulse lengths can be used compared to normal extraction, increasing secondary ion yields. In comparison to normal extraction, delayed extraction optimises the mass resolution over a limited mass range. Within this range, the mass resolution is better than that of normal extraction, but outside the mass resolution is relatively poor in comparison. For the purpose of this project, the mass resolution was optimised towards the low mass end of the spectrum, giving good mass resolution for the major elements in presolar SiC grains.

Delayed extraction also causes elemental and isotopic mass fractionation to develop, as lighter elements and isotopes travel further from the sample stage during the length of the primary ion pulse. When the stage voltage is applied, many of these lighter ions have travelled beyond the extraction cone, resulting in proportionally fewer light secondary ions being extracted and detected. These mass fractionation effects are determined by analysing the SiC and silicate standards, which are terrestrial and so have known isotope ratios.

3.3.2.3 Flight Tube and Detector

Following extraction, secondary ions pass into the flight tube where they are separated according to their time-of-flight. IDLE-3 uses a two-stage reflectron with a graduated electric field. The electric field opposes that of the extraction field, causing the secondary ions to decelerate until their flight paths are inverted. The reflectron compensates for the energy spread (see Figure 3.8) of the secondary ions; high velocity ions penetrate deeper into the electric field, increasing the length of their flight path compared to low velocity ions. As a result, the flight time of both high and low energy secondary ions is the same, so they arrive at the detector together, producing a higher mass resolution.

Once the flight paths have been inverted, the secondary ions arrive at the detector. IDLE-3 has a multi-channel plate (MCP) detector with a scintillator and photomultiplier. As each secondary ion hits the detector, an electrical pulse is generated; this pulse is input into a Time-to-Digital Converter (TDC), and converted into a flight time for the secondary ion. Mass spectra for each pixel in a scan are produced by combining the flight times of secondary ions from multiple primary ion shots.

If multiple secondary ions arrive at the detector simultaneously, dead time effects arise. In order to eliminate background noise, the detector operates with a threshold limit; if two secondary ions arrive in rapid succession, they register as a single ion, as the signal does not have sufficient time to drop below the threshold level before the second ion arrives. On IDLE-3, the dead time is ~5 ns. Dead time effects are typically a problem for highly abundant elements, and those with a high ionisation efficiency.

3.3.2.4 Data Analysis

During an analysis, the primary ion beam is rastered across the sample surface, with multiple scans acquired (typically >500 per measurement). Data are acquired using the Bio-TOF software, which allows the number of pixels and primary ion shots per pixel to be set, with a complete mass spectrum saved for each pixel in a scan. During a measurement, the emission from the primary ion gun occasionally stops, resulting in empty pixels until the emission stabilises again. As each scan is saved separately, scans with empty pixels can be removed; typically, less than 1% of scans are thrown out.

The data from each measurement are reduced using ToFCmd (Detlef Rost and Torsten Henkel) and TSTSpec (Thomas Stephan, University of Chicago). In ToFCmd, unusable scans are removed, and an instrumental drift correction is applied; drift occurs throughout a measurement as a result of temperature changes as the ion source warms up. A Region of Interest (ROI) is defined around the grain, with a mass spectrum generated for each ROI.

Each mass spectrum is analysed using TSTSpec; a mass calibration is applied by selecting at least two known mass peaks and assigning secondary ion species to them, with the calibration averaged between the selected peaks. A statistical dead time correction (5 ns) is applied to the mass spectrum (Stephan et al., 1994) to account for simultaneous arrivals of secondary ions. Peaks (and the background) are selected across the mass spectrum, allowing elemental and isotope ratios to be determined.

A file containing the Relative Sensitivity Factors (see Section 3.3, this thesis) is imported into TSTSpec in order for elemental abundances to be determined. Isotope ratios are calculated by 'peak fitting', where peaks of minor isotopes are compared to the major isotope, before mass fractionation corrections are applied.

Chapter 4

This chapter contains a draft of a multi-author paper to be submitted to a journal. I am the first author. Within this I was responsible for data collection and analysis, interpretation of the results, and writing the paper as presented.

Isotopic Fractionation Induced by Sample Topography During SIMS Analysis

A. Clarke¹, T. Henkel¹, K. L. Moore², G. McMahon² and I. C. Lyon¹

¹School of Earth and Environmental Sciences, The University of Manchester, Williamson Building, Oxford Road, Manchester, M13 9PL

²School of Materials and Photon Science Institute, The University of Manchester, Alan Turing Building, Oxford Road, Manchester, M13 9PL

We present the effects of sample topography on the extraction and transmission of atomic and molecular secondary ions in the NanoSIMS. The topography of a sample creates distortions in the local electric field, which affect the trajectories of secondary ions as they are sputtered. As atomic secondary ions typically have higher kinetic energy, they are able to ‘punch through’ the distorted local field, forming a homogeneous beam at the D1 aperture. Molecular ions, with a lower kinetic energy on average, are strongly affected by the local electric field, which results in a heterogeneous beam distribution at the D1 aperture. These differences mean there is the potential for differing rates of transmission between atomic and molecular secondary ions, which could cause fractionation of molecular ions.

4.1 Introduction

In separate work (see Chapter 5, this thesis), presolar SiC grains were analysed using a Cameca NanoSIMS 50L- a secondary ion mass spectrometer (SIMS) capable of measuring samples with high sensitivity and spatial resolution. Each grain was analysed at high spatial resolution (~100 nm) to produce secondary ion images of $^{12}\text{C}^-$, $^{13}\text{C}^-$, $^{12}\text{C}^{14}\text{N}^-$, $^{12}\text{C}^{15}\text{N}^-$, $^{28}\text{Si}^-$, $^{29}\text{Si}^-$ and $^{30}\text{Si}^-$. Each grain showed homogeneous distributions for the carbon and

silicon ions, whilst heterogeneous distributions were seen for the CN⁻ ions for many grains, with enrichments at the grain edges (see Figure 4.1).

As heterogeneity can inform on the processing history of the SiC grains (Stephan et al., 1997; Verchovsky et al., 2001; Bernatowicz et al., 2003; Verchovsky et al., 2004; Stroud and Bernatowicz, 2005; Henkel et al., 2007a; Lyon et al., 2007; King et al., 2012), it is important to determine whether the enrichments of nitrogen at the grain edges are real, or whether measurement artefacts can create apparent heterogeneity. Heterogeneity is only observed in the CN⁻ ions, and only in SiC grains from the acid residues (rather than those from the polished meteorite sections), suggesting that grain topography may affect the extraction and flight paths of molecular secondary ions inside the mass spectrometer.

Secondary ions are produced with a spread of kinetic energies (see Figure 4.2); direct impact from a primary ion will typically produce high energy secondary ions, whilst glancing impacts or collision cascades will typically transfer less kinetic energy into a sputtered secondary ion. On average, molecular secondary ions have a lower kinetic energy than atomic secondary ions (Figure 4.2). Molecular secondary ions peak at an energy of ~2.5 eV, with a half-width of around 2 eV. In contrast, atomic secondary ions peak at ~4 eV, with a half-width of 5 eV. The peak for molecular secondary ions is much sharper, whilst atomic secondary ions have a broad energy distribution, with significant numbers of ions sputtered at energies >10 eV. The differences between these energy distributions is caused by the way in which energy is transferred following a collision with a primary ion. The energy is converted into the rotational, vibrational and kinetic energy of a molecular secondary ion; with atomic ions, the energy is predominantly transferred as kinetic energy.

As sample topography distorts the local electric field, the region of the field which directly interacts with the sample, the flight paths of secondary ions may be affected. This has the potential to result in the beams of atomic and molecular ions being focused at different positions on the apertures and slits through the mass spectrometer. The relative transmission of atomic and secondary ions may be affected, resulting in elemental and isotopic fractionation. Related work (Lyon et al., 2015; Lyon et al., 2016) examined this effect by scanning the beam focus across the entrance slit of the NanoSIMS spectrometer by altering the Cy, one of the slits inside the spectrometer, which causes the beam focus

point to move across the slit. As the focus is shifted, atomic secondary ions continue to produce homogeneous images (see Figure 4.3), although the ion intensity decreases as the beam is shifted away from its optimum position. In contrast, the molecular secondary ion images vary considerably as the beam is altered, with regions of high intensity shifting from left to right across the secondary ion images (see Figure 4.3), suggesting that the molecular secondary ion beam is heterogeneous, and resulting in differential transmission of atomic and molecular secondary ions.

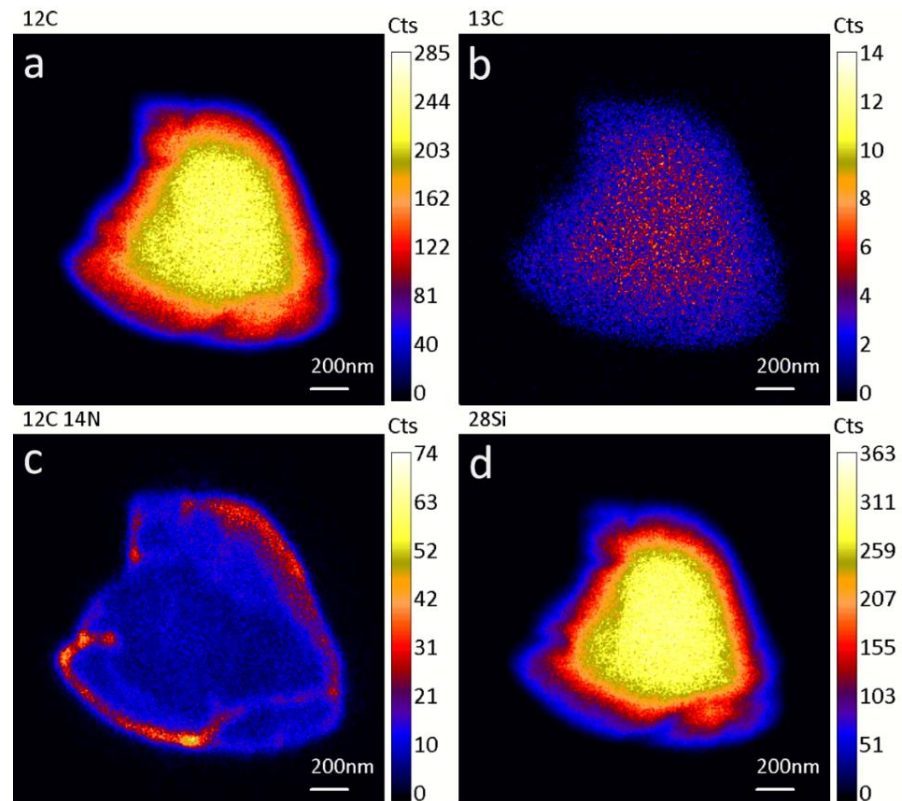


Figure 4.1: Secondary ion images of a) ^{12}C , b) ^{13}C , c) $^{12}\text{C}^{14}\text{N}$, and d) $^{28}\text{Si}^-$ from grain AC-KJG-1, a presolar SiC grain from the KJG residue (Amari et al., 1994). The C and Si isotopes have homogeneous distributions within the grain, whilst CN^- is enriched near the edge of the grain.

In this work, we examine the effect of sample topography on the extraction and transmission of atomic and molecular secondary ions. The flight paths of high (atomic) and low (molecular) secondary ions are examined by simulating their trajectories through the NanoSIMS optics, in order to determine if element and isotope fractionation may be affected by topography. Additionally, this fractionation is studied by analysing terrestrial SiC grains using the NanoSIMS; the beam focus is scanned across the optics of the mass spectrometer by adjusting Cy.

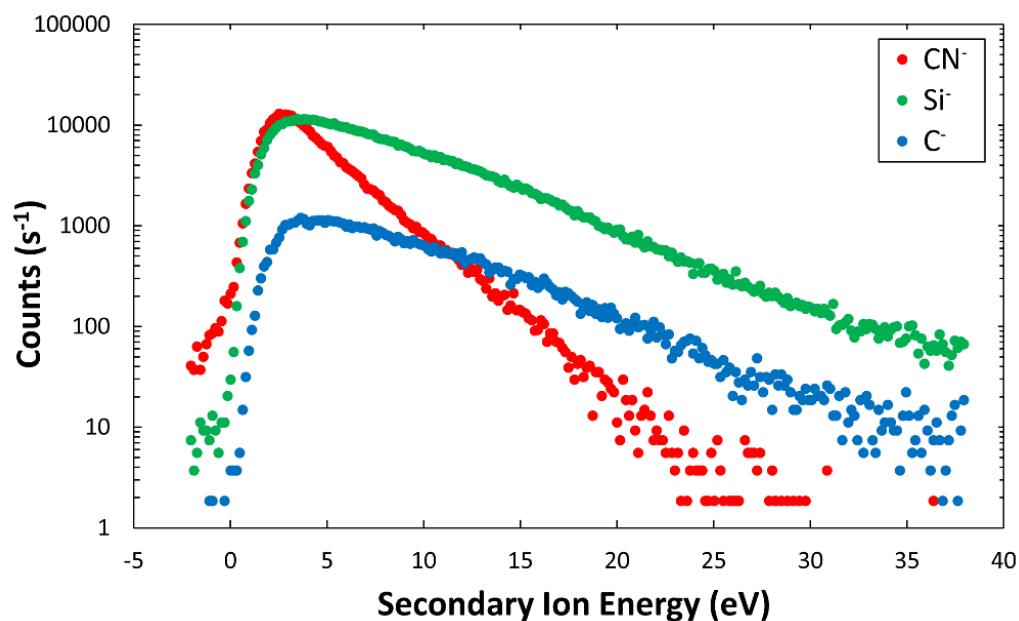


Figure 4.2: Kinetic energy spread of Si^- , C^- and CN^- secondary ions. Molecular secondary ions display a peak at 2.5 eV, with a half-width of 2 eV. The atomic secondary ions peak at ~4 eV with a half-width of ~5 eV. The peak for molecular ions falls away rapidly, whilst there are still significant numbers of atomic secondary ions at energies >10 eV.

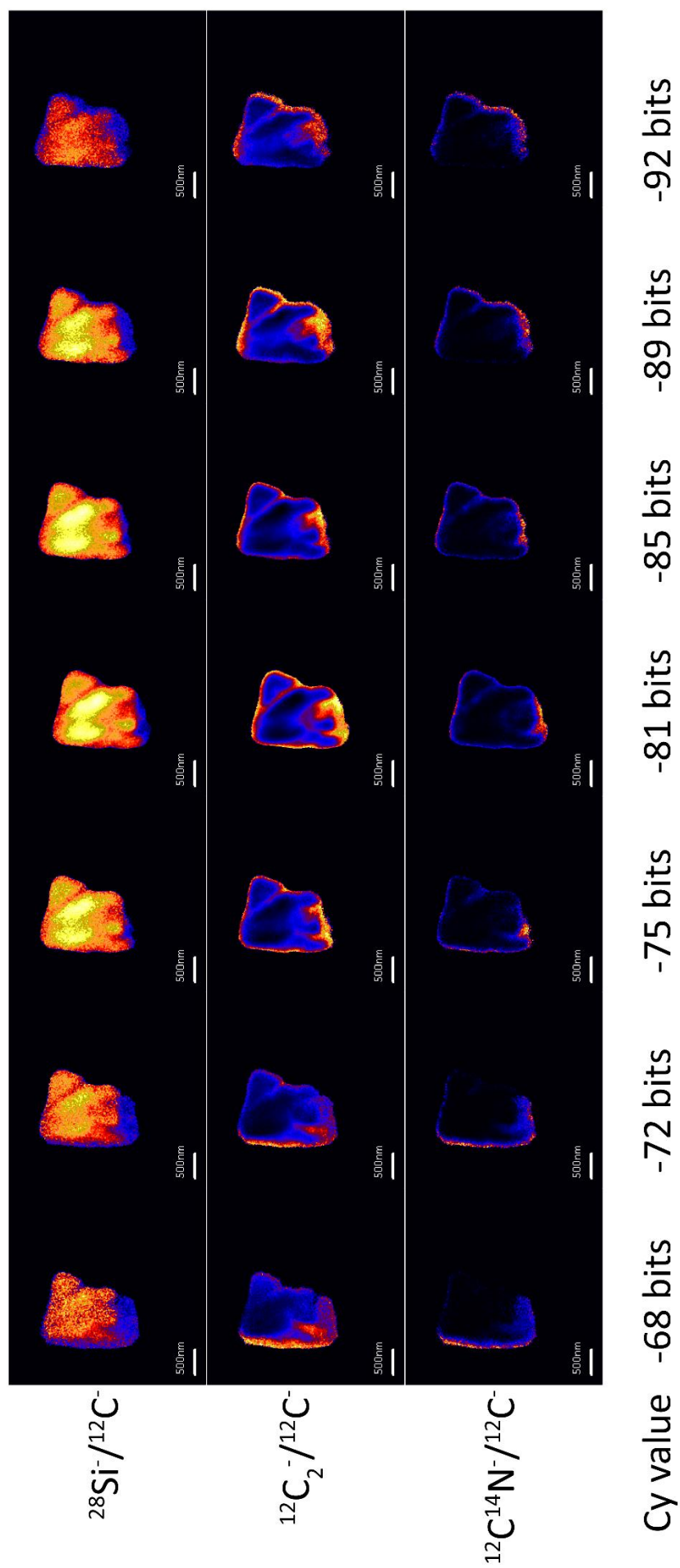


Figure 4.3: NanoSIMS isotope ratio images of $^{28}\text{Si}^-/^{12}\text{C}^-$, $^{12}\text{C}_2^-/^{12}\text{C}^-$, and $^{12}\text{C}^{14}\text{N}^-/^{12}\text{C}^-$ at varying Cy values. Altering Cy scans the beam focus across the entrance slit of the mass spectrometer. At the time of analysis, the optimum Cy value was -81 bits (centre image).

4.2 Methods

4.2.1 SIMION Modelling

The flight paths of different secondary ions in the NanoSIMS were simulated using SIMION software (Scientific Instrument Services). The software models the propagation of charged particles (for which the mass, charge, energy etc. can be altered) through a series of pre-defined electrodes.

A potential array, defining the shape, size, and position of the electrodes inside the mass spectrometer must first be created. This work uses the NanoSIMS array produced by Bernheim et al. (2008), altered to include the addition of a small grain ($\sim 5 \mu\text{m}$) on the sample surface, in order to determine the effects of topography on secondary ion extraction. Ideally, a smaller grain would be modelled, to better represent the size of the presolar SiC grains, but the spatial resolution of the SIMION software limited this.

The array includes the section of the ion optics closest to the sample surface (Figure 4.4). EOP and EOS focus the primary and secondary ion beams respectively, whilst EOW extracts secondary ions from the sample surface. Whilst there is no potential difference between EOW and the sample surface, the potential between EOW and EOP causes the field lines to penetrate through the EOW aperture (see Figure 4.5), resulting in secondary ions being extracted away from the sample surface.

Equipotential surfaces, contours of equal electric potential, were determined using the 'relaxation' method in the software. During this process, a test voltage ($\sim 1 \text{ V}$) was applied to each of the electrodes. Each pixel in empty space is individually examined, with its voltage adjusted based on the surrounding pixels. This protocol continues until smooth voltage gradients have been determined; an example of the equipotential surfaces over the pre-defined grain can be seen in Figure 4.6.

Once the equipotential surfaces have been calculated, the correct voltages are applied to each electrode. The NanoSIMS can be set up to analyse either positive or secondary ions; the same numerical voltages are used in each case, but opposite polarities are required. As this work is concerned with the analysis of negative secondary ions, negative voltages were applied to EOS (-6950 V), EOW and the sample (both -8000 V), whilst a positive potential was applied to EOP ($+8500 \text{ V}$), as it is used to focus the positively charged

primary ions (Cs^+). The process of applying the correct voltages is significantly faster than the 'relaxation' phase; as the potential gradients have already been determined, the applied voltage is simply scaled over these.

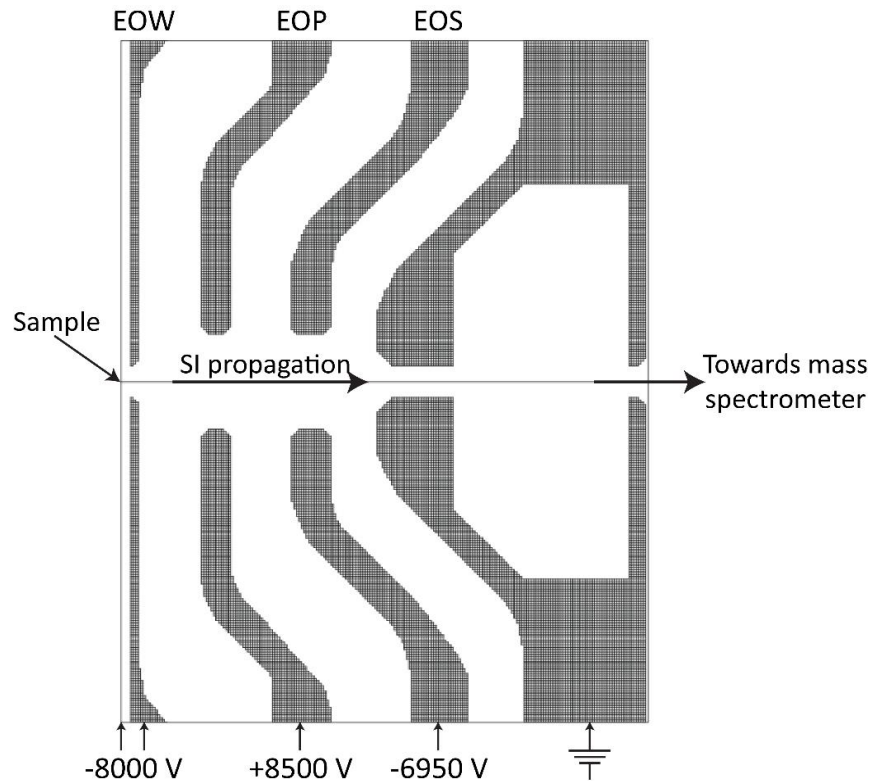


Figure 4.4: The potential array of the lenses closest to the sample surface in the Cameca NanoSIMS. EOP and EOS focus the primary and secondary ion beams respectively, whilst EOW is the extraction lens. Image is adapted from Bernheim et al. (2008).

Simulated secondary ions can be fired from selected locations on the sample; for this work, ions were extracted from the centre (on-axis) and edges of the simulated grain. The mass, energy range, charge, and angle of extraction of the secondary ions can be easily altered using the software. For this work, $^{12}\text{C}^-$ ions with a moderate angular distribution were extracted. The choice of secondary ion has no effect on the results, as it is the ion's energy which ultimately affects its flight through the electric field; atomic and molecular ions with the same kinetic energy will behave in the same way. Twenty one secondary ion energies were modelled, from 0.1 eV to 50 eV, with the secondary ion beam width at the D1 aperture determined for each ion energy. The modelled beam widths were weighted and combined according to the measured kinetic energy spectra of $^{12}\text{C}^-$, $^{28}\text{Si}^-$ and $^{12}\text{C}^{14}\text{N}^-$ (Figure 4.2), in order to calculate secondary ion beam widths for each secondary ion

species. This allowed the transmission of both atomic and molecular secondary ions to be modelled through the NanoSIMS optics.

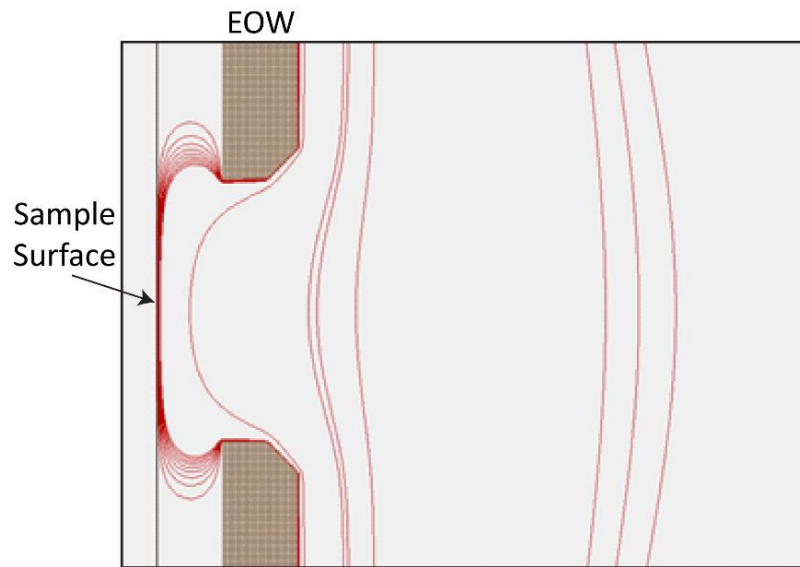


Figure 4.5: The calculated equipotential surfaces which penetrate through the EOW aperture to the sample surface, resulting in flat field lines at the sample surface.

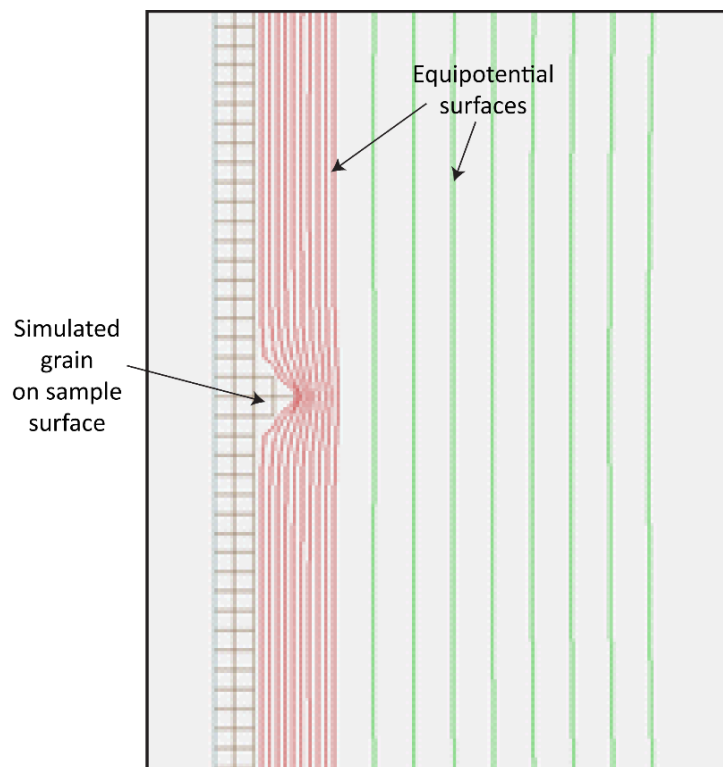


Figure 4.6: The calculated equipotential surfaces over a simulated 5 μm grain on the sample surface. The field lines are generally parallel to the sample surface, although the local electric field is distorted by the grain's topography. The red equipotential surfaces are 1 V apart, whilst the green lines are 5 V intervals.

4.2.2 NanoSIMS Analysis

Terrestrial silicon carbide grains, commonly used as a polishing powder, were analysed using a Cameca NanoSIMS 50L at The University of Manchester. The grains were dispersed over a 7x7 mm piece of high purity gold foil, before being pressed using a titanium carbide block to ensure they did not fall from the mount.

In order to identify any isotopic fractionation effects which may occur when measuring molecular ions, carbon isotopes were detected as both atomic ($^{12}\text{C}^-$ and $^{13}\text{C}^-$) and molecular ($^{12}\text{C}_2^-$ and $^{12}\text{C}^{13}\text{C}^-$) ions. As ^{13}C can be sputtered as either $^{12}\text{C}^{13}\text{C}^-$ or $^{13}\text{C}^{12}\text{C}^-$ secondary ions, the $^{12}\text{C}/^{13}\text{C}$ ratio of the molecular ions is half that of the atomic ions. In addition to carbon isotopes, secondary ions of nitrogen (as $^{12}\text{C}^{14}\text{N}^-$ and $^{12}\text{C}^{15}\text{N}^-$) and silicon ($^{28}\text{Si}^-$) were analysed.

A 50x50 μm field with high grain density was pre-sputtered for ~5 minutes with a ~1.5 nA Cs^+ beam (D1-0 aperture) to ensure a sputtering equilibrium was reached. From this field, a group of grains with reasonable topography were selected (see Figure 4.7). The grains, centred in a 12x12 μm field-of-view, were rastered using a Cs^+ beam (D1-4 aperture, ~130 nm spatial resolution) to produce secondary ion images, each 512x512 pixels and 20 frames.

Five measurements of the terrestrial SiC grains were acquired at Cy values of -370, -374, -378 (the optimum setting), and -386 bits. Adjusting the Cy value shifts the position of the beam focus across the slit inside the mass spectrometer; the optimum value (-378 bits) should result in the beams passing through the centre of the mass spectrometer optics.

The L'Image software (Larry Nittler, Carnegie Institution of Washington) was used to reduce the data collected during these analyses. The individual frames of each measurement were aligned to correct for instrumental drift, which occurs as a result of the beam and/or stage shifting during an analysis. Individual ion images were combined to produce isotope ratio images, before Regions of Interest (ROIs) were selected for each grain in the field, allowing the isotope ratios of each grain to be determined.

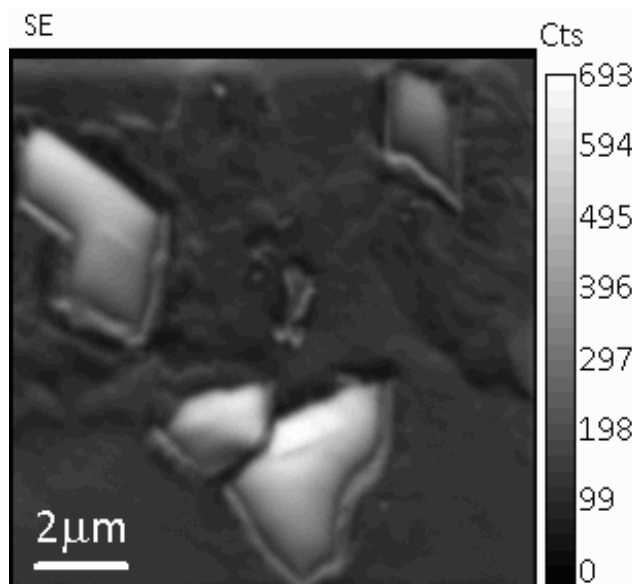


Figure 4.7: Secondary electron (SE) image of a group of terrestrial silicon carbide grains. The grains were analysed at varying Cy values to determine any fractionation effects between atomic and molecular secondary ions.

4.3 Results and Discussion

4.3.1 SIMION Modelling

4.3.1.1 High Energy Secondary Ions

High energy secondary ions produced from the centre and edge of the grain are extracted from the sample surface with a wide angular distribution (see Figure 4.8). Secondary ions from both the centre and edges are extracted parallel to the direction of primary ions. The trajectories of secondary ions do not differ across the grain, suggesting that the topography of a sample has little influence on the extraction of high energy ions. The large relative energy of the ions, compared to the sample surface, means they can effectively ‘punch through’ the local electric field.

The flight paths of ions from different parts of the grain cross over as the ions are extracted, due to their wide angular distribution (see Figure 4.9). Ions arrive at the exit slit of the optics as a wide, diffuse beam. The resulting image bears no resemblance to the grain, with each ion having lost spatial coherence with its original location. The resulting ion images are homogeneous- as is seen with the C and Si ion images from the analysis of presolar SiC grains (see Figure 4.1).

The diffuse beam of atomic ions may be wider than the slits and apertures through the mass spectrometer, resulting in lower transmission through the instrument. All atomic ions would be affected in this case, so should not cause any element or isotope fractionation with other atomic ions.

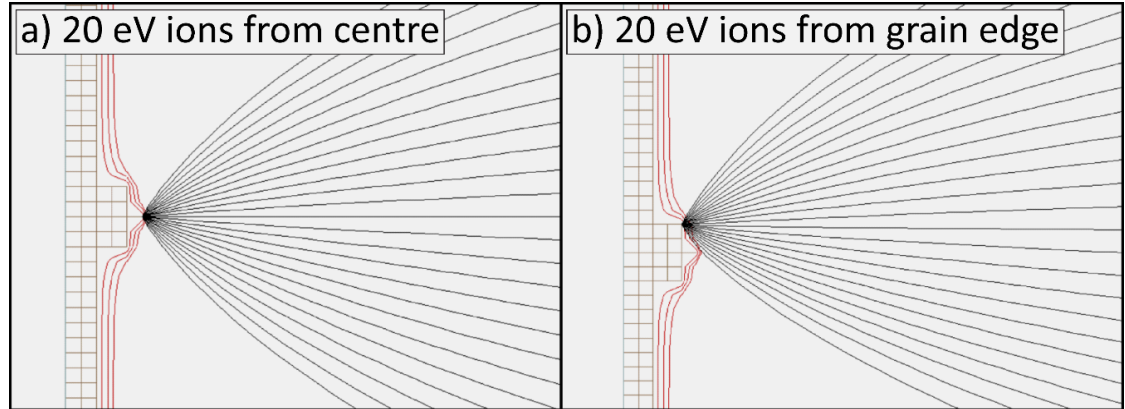


Figure 4.8: Simulated trajectories of high energy (20 eV) secondary ions originating from the a) centre, and b) edge of a 5 μm grain. Black lines are secondary ion trajectories, whilst red lines define the equipotential surfaces.

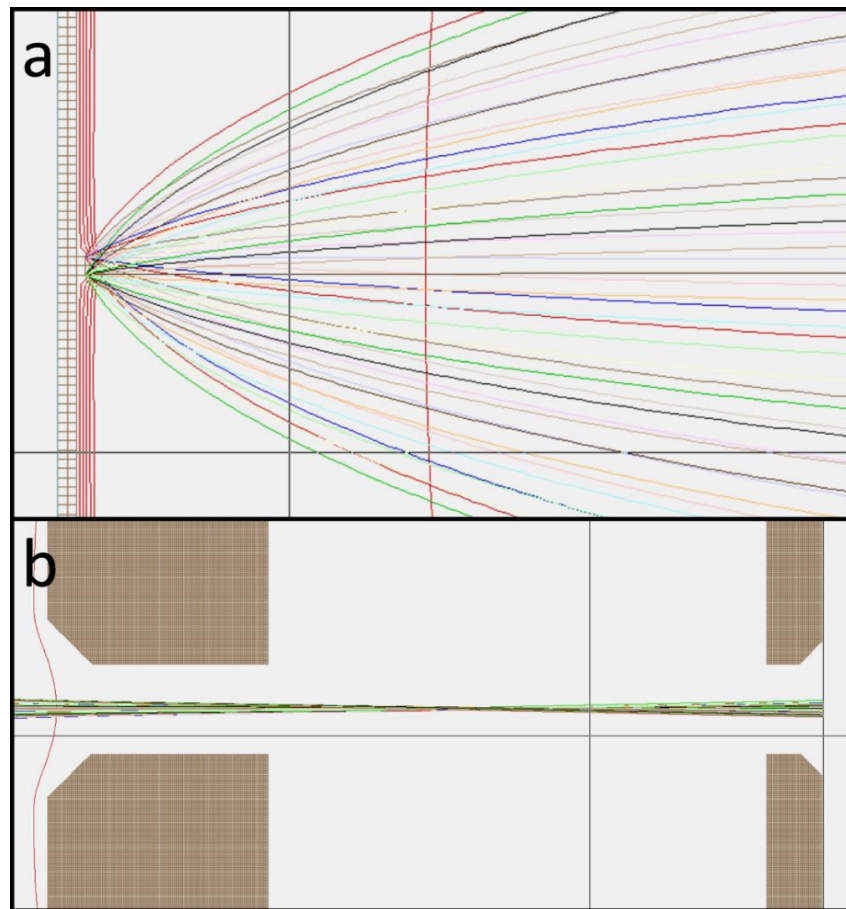


Figure 4.9: Trajectories of 20 eV secondary ions from across the grain a) at the sample surface, and b) at the exit slit of the optics.

4.3.1.2 Low Energy Secondary Ions

As Figure 4.10 shows, low energy (molecular) ions are extracted with a narrower angular distribution than high energy ions. The energy spread of molecular ions is smaller than that of atomic ions, allowing them to be more easily focused through the extraction optics.

Whilst ions from the centre of the grain are extracted normal to the sample surface, along the spectrometer axis, ions from the edge of the grain follow a more curved trajectory. The low energy of the ions means they are more strongly influenced by the distortions in the local electric field, produced by the topography at the sample surface. As a result, the ions are initially pulled off-axis by the local field, before following a trajectory approximately perpendicular to the sample surface.

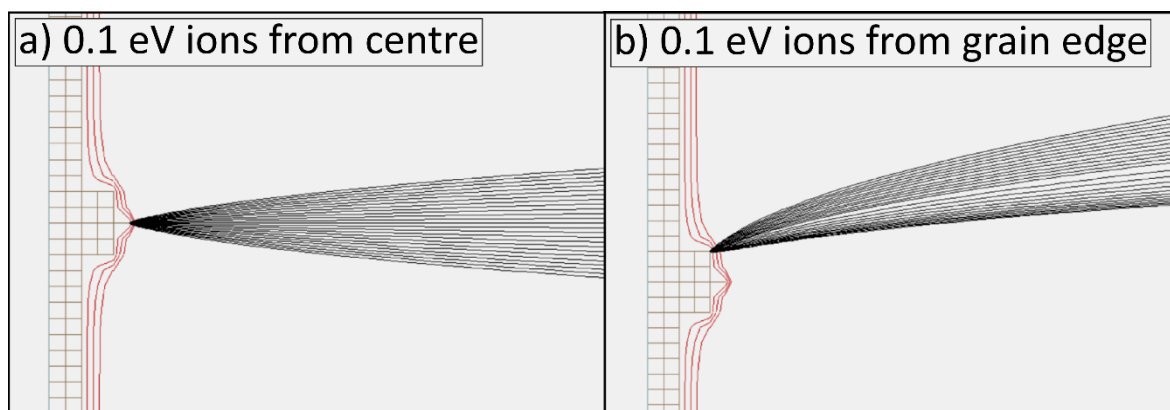


Figure 4.10: Simulated trajectories of low energy (0.1 eV) secondary ions from a) the centre, and b) the edge of a 5 μm grain. Black lines indicate secondary ion trajectories, whilst red lines define the equipotential surfaces.

The low energy ions from the edges of the grain follow this trajectory to the exit slit of the optics, arriving as distinct beams from different regions of the grain (see Figure 4.11). As a result, molecular ions project an 'image' of the grain onto the slit, unlike the high energy ions.

These results suggest that the heterogeneous ion images of CN^- from presolar SiC grains are caused by the topography of the acid residue grains. The apparent enrichments of nitrogen towards the edges of the grains likely just reveal the topography of the sample, rather than representing real isotopic heterogeneity.

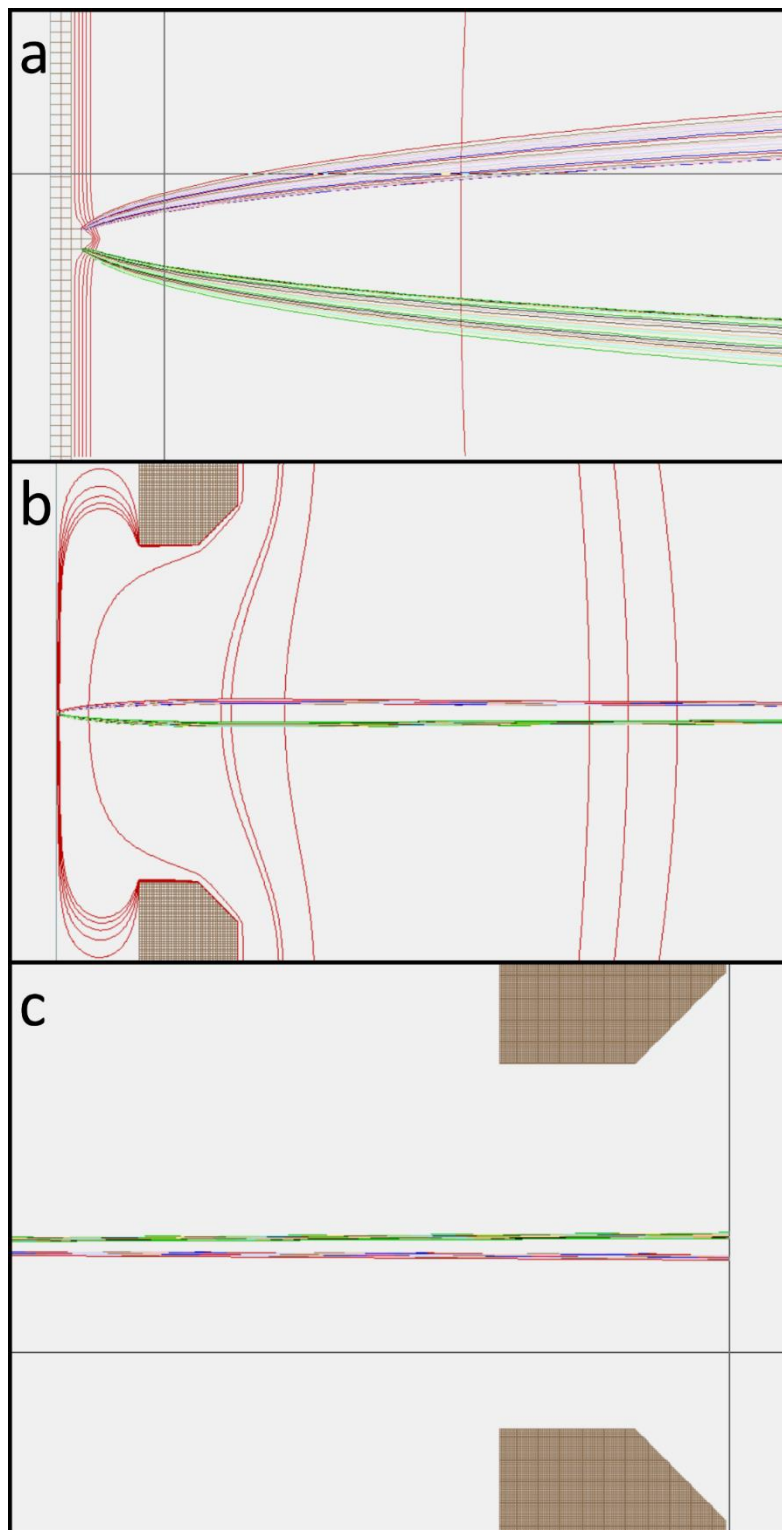


Figure 4.11: Simulated trajectories of low energy (0.1 eV) secondary ions from across the grain a) at the sample surface, b) through the mass spectrometer, and c) at the exit slit of the optics.

Modelled cumulative ion currents as a function of slit width, for secondary ions with a cosine angular distribution and the energy spectrum shown in Figure 4.2, are shown in Figure 4.12. The data suggest that the atomic secondary ion beams are wider at the D1 aperture than the molecular secondary ion beams, with potential for reduced

transmission when using smaller apertures such as D1-4 (150 nm) and D1-5 (100 nm). Although the molecular ion beam benefits from higher transmission through smaller apertures when the instrument is properly aligned, the steep curve means that improper alignment could result in a disproportionate loss of transmission compared to atomic secondary ions, resulting in elemental and isotopic fractionation.

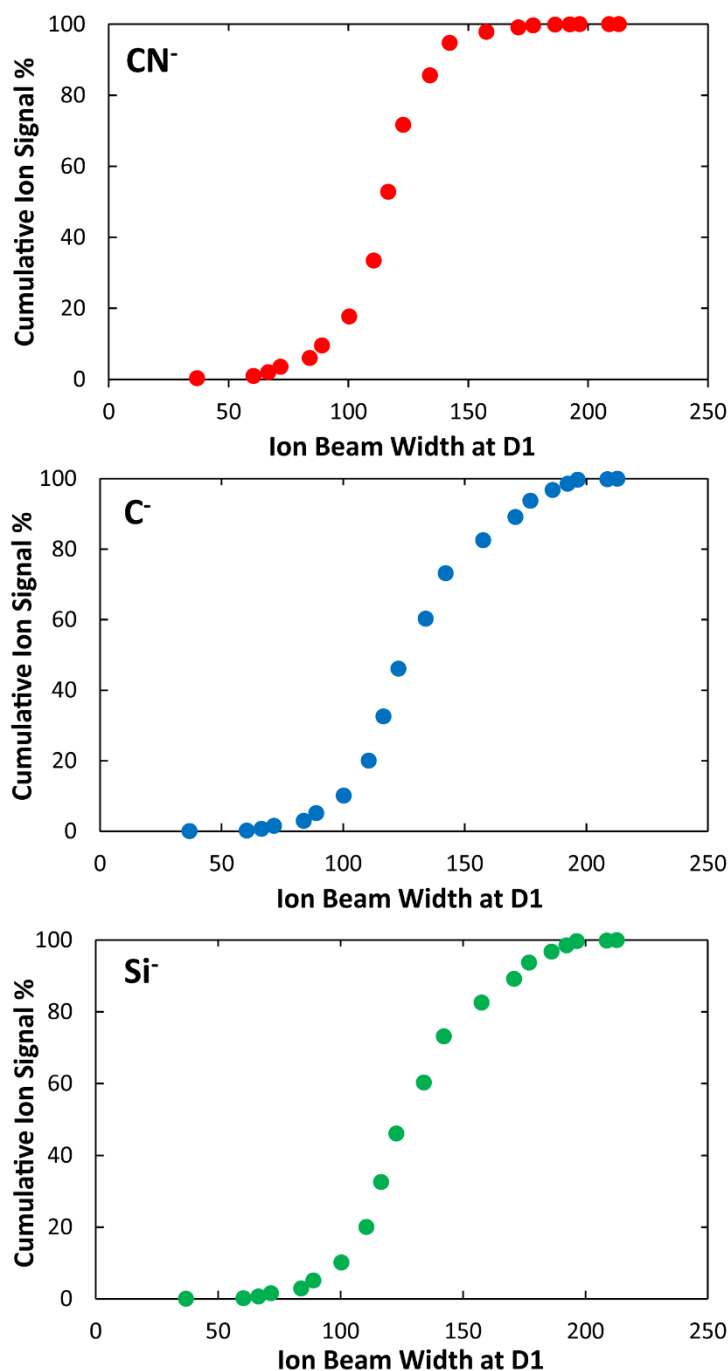


Figure 4.12: Cumulative currents of C^- , CN^- and Si^- secondary ions as a function of slit width.

The dispersal of molecular secondary ions can lead to differential transmission of ions at the apertures and slits through the mass spectrometer. In order to achieve such high spatial resolution compared to other SIMS instruments, the slits and apertures inside the NanoSIMS spectrometer are particularly narrow. The result is that high intensity regions of the molecular secondary ion beam may be cut off, resulting in element and isotope fractionation with the atomic secondary ions. The homogeneous nature of the atomic secondary ion beam means proportionally fewer ions are lost.

4.3.2 Effects of Altering Cy

The $^{14}\text{N}/^{15}\text{N}$ (measured as $^{12}\text{C}^{14}\text{N}^-/^{12}\text{C}^{15}\text{N}^-$) and $^{12}\text{C}/^{13}\text{C}$ (for both $^{12}\text{C}^-/^{13}\text{C}^-$ and $^{12}\text{C}_2^-/^{12}\text{C}^{13}\text{C}^-$ secondary ions) were determined for terrestrial SiC grains measured at Cy values between -370 and -386 bits. As Figure 4.13 shows, the Cy value has minimal effect on the $^{12}\text{C}/^{13}\text{C}$ ratios of the atomic secondary ions, with the measured ratios falling within 2σ errors of each other.

In contrast, the $^{12}\text{C}/^{13}\text{C}$ ratios of the molecular ions show significant variation as Cy is altered. As Figure 4.13 shows, the $^{12}\text{C}/^{13}\text{C}$ ratios cluster together for four of the analyses (with Cy values of -370, -374 and -378), although the measured ratios are ~3% lower than those determined for the atomic C ions. Whilst the absolute $^{12}\text{C}/^{13}\text{C}$ ratio of the terrestrial SiC grains has not been determined in this work, the 3% variation between atomic and molecular C ions will not affect the analysis of presolar SiC grains, as the measured isotope ratios are normalised to those of a terrestrial standard analysed under the same experimental conditions.

The $^{12}\text{C}/^{13}\text{C}$ ratio at a Cy value of -386 is anomalous, and is ~20% higher than those determined at higher Cy values (Figure 4.13). The variation in the $^{12}\text{C}/^{13}\text{C}$ ratios of molecular ions suggests that altering the Cy value strongly affects the fractionation of molecular secondary ions, whilst atomic secondary ions are largely unaffected.

The variation in Cy appears to also cause fractionation of the nitrogen isotopes, with measured $^{14}\text{N}/^{15}\text{N}$ ratios varying by ~45% (see Figure 4.14), although there are large errors on these measurements. As terrestrial SiC grains have extremely low abundances of N, it is difficult to know if these variations are real or affected by the low count rates.

However, as the molecular C ions are fractionated at low Cy values, it is reasonable to assume that CN⁻ ions may also be affected by altering Cy.

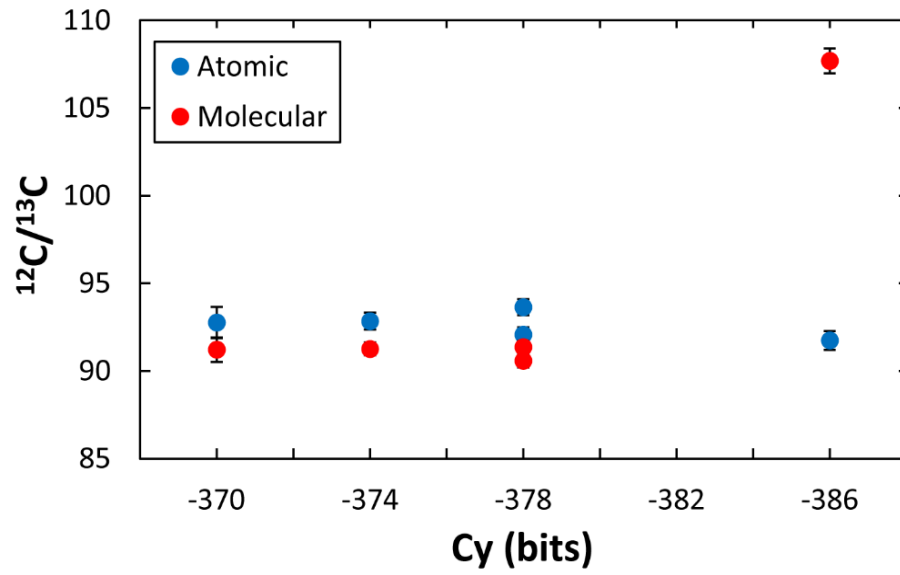


Figure 4.13: Variation in the $^{12}\text{C}/^{13}\text{C}$ ratios of atomic and molecular C secondary ions at varying Cy values. At the time of analysis, the optimum Cy value was -378 bits. Errors are 1σ .

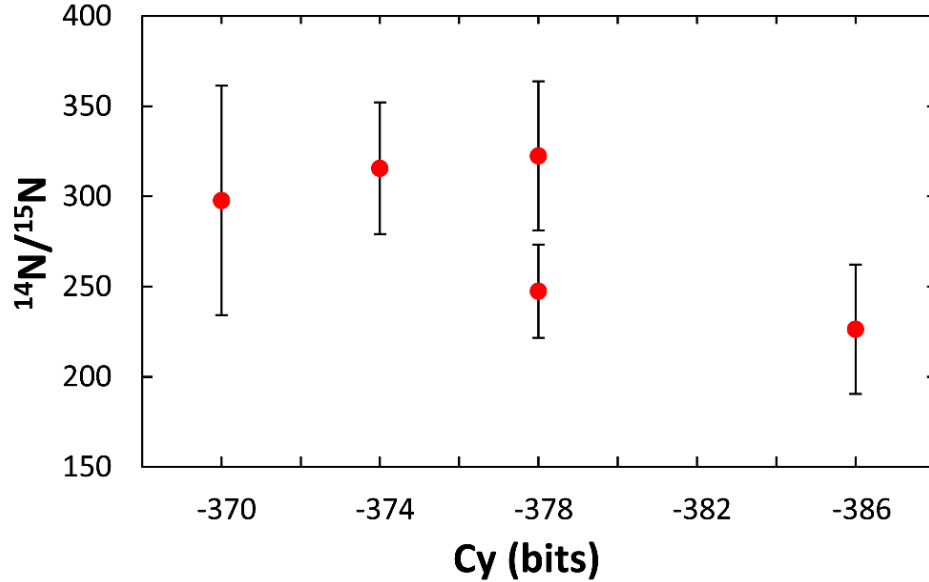


Figure 4.14: Variation in $^{14}\text{N}/^{15}\text{N}$ ratios in terrestrial SiC grains at varying Cy values. Nitrogen isotope ratios were determined from $^{12}\text{C}^{14}\text{N}/^{12}\text{C}^{15}\text{N}$ isotopes. At the time of analysis, the optimum Cy value was -378 bits. Errors are 1σ .

As was detailed in Section 4.3.1, the topography of a sample strongly influences the flight paths of secondary ions through the mass spectrometer. Atomic ions arrive at the slit as a

diffuse, homogeneous beam, whilst molecular ions are dispersed, producing an 'image' of the grain at the slit. As C_y is varied, the secondary ion beams are scanned across the entrance slit of the mass spectrometer. The result is that differential transmission of atomic and molecular ions occurs, causing elemental and isotopic mass fractionation. As this work shows, this fractionation only appears to occur at extreme C_y values, when the beam is considerably shifted relative to the entrance slit. As a result, the fractionation of atomic and molecular ions should be reasonably limited providing the instrument is properly aligned.

4.4 Conclusions

This work has determined that the topography of a sample has a significant effect on the trajectories and fractionation of molecular secondary ions compared to atomic ions.

Molecular ions, which typically have low kinetic energy, are strongly affected by the local electric field at the sample surface. Ions from different points on a grain are dispersed as they are extracted, resulting in an 'image' of the grain being projected onto the slits and apertures inside the mass spectrometer. In contrast, atomic ions typically have a higher kinetic energy, allowing them to 'punch through' the local field, regardless of their original position on the grain. Atomic ions are extracted as a diffuse beam, and produce a homogeneous image at the slits and apertures. As a result of their altered trajectories, the focus of atomic and molecular ions may differ, resulting in differential transmission which has the potential to cause elemental and isotopic fractionation.

A group of terrestrial SiC grains were analysed at various C_y values to determine the fractionation of atomic and molecular ions. Altering C_y shifts the beam focus across the entrance slit of the spectrometer. As the atomic ions arrive as a diffuse, homogeneous beam, no isotopic fractionation occurs as a result of altering C_y . The molecular ions are largely unaffected with moderate shifts in the beam focus, although significant isotopic fractionation occurs at extreme C_y values. Providing the instrument is properly aligned, no significant fractionation of atomic and molecular ions should occur.

These results are able to explain the differing ion images produced when analysing presolar SiC grains. The topography of the grains causes the carbon and silicon isotopes to have homogeneous distributions, with the individual ions losing spatial coherence with

their original position on the grain. The heterogeneous $^{12}\text{C}^{14}\text{N}^-$ images are the result of ions from across the grain becoming dispersed as they are extracted. Rather than suggesting an enrichment of nitrogen at the edge of the grain, the images instead give a clearer image of the grain topography.

Acknowledgements

We thank Roy Lewis for the provision of the KJG grains, from which the isotopic heterogeneity was first identified.

Chapter 5

This chapter contains a draft of a multi-author paper to be submitted to a journal. I am the first author. Within this I was responsible for data collection and analysis, interpretation of the results, and writing the paper as presented.

A Comparison of Acid Residue and *In-Situ* Presolar SiC Grains

A. Clarke¹, T. Henkel¹ and I. C. Lyon¹

¹School of Earth and Environmental Sciences, The University of Manchester, Williamson Building, Oxford Road, Manchester, M13 9PL

We report the carbon, nitrogen and silicon isotope ratios for 185 presolar silicon carbide grains measured with very high spatial resolution to determine whether there was any isotopic heterogeneity in the grains, and to avoid the alteration of measured isotope ratios by contamination with material from around the grains introduced either during sample preparation or during analysis. SiC grains from three acid residues and two polished sections were analysed to compare the effect of sample preparation on the grain populations from different meteorites.

The measured isotope distributions match the existing literature data, although small differences exist between the distributions for individual samples. Whilst it is possible the grains were affected by terrestrial contamination, and/or isotopic dilution in the case of the *in-situ* grains, modelling suggests these effects are minimal.

These results suggest the possibility of differing grain populations between samples, although a larger sample size, particularly for the *in-situ* grains, is necessary to confirm this.

5.1 Introduction

Presolar grains are sub-micron to micron-sized dust grains which formed as condensates in the outflows and ejecta of stars, prior to the formation of the solar system. They are characterised by their highly anomalous isotope ratios which vary by up to several orders of magnitude for many elements, relative to solar compositions (Zinner et al., 1987;

Zinner et al., 1989; Alexander, 1993; Hoppe et al., 1994; Nittler, 2006). These isotopic anomalies cannot be reproduced by any known natural processes within the solar system, and are only explained by stellar nucleosynthesis.

Following their formation, presolar grains travelled through the interstellar medium (ISM) into the early solar nebula, where they were incorporated into solar system bodies such as asteroids, interplanetary dust particles (IDPs) and comets (Huss and Lewis, 1995; Messenger et al., 2003; Messenger et al., 2005; Zinner, 2014). Their long and complicated history means that presolar grains have likely been affected by many processes in the ISM, solar nebula, and meteorite parent bodies. These processes include, but are not limited to, interaction with galactic cosmic rays (GCRs), UV radiation, and supernovae shockwaves; ion or atom implantation; collisions with other grains or gases; surface ice formation; vapourisation and recondensation; and aqueous or thermal alteration within parent asteroids (Huss and Lewis, 1995; Jones et al., 1997; Alexander and Nittler, 1999; Ehrenfreund and Charnley, 2000; Verchovsky et al., 2001; Bernatowicz et al., 2003; Lyon et al., 2007).

Since their discovery in 1987 (Lewis et al., 1987), many types of presolar grain have been identified, including nanodiamonds, graphite, silicon carbide, silicon nitride, oxides, silicates, and refractory carbides (Bernatowicz et al., 1987; Lewis et al., 1987; Amari et al., 1990; Hutcheon et al., 1994; Nittler et al., 1994; Choi et al., 1998; Alexander and Nittler, 1999; Zinner et al., 2003; Nittler et al., 2005b; Floss et al., 2008; Nittler et al., 2008). Presolar silicon carbide grains are the best studied, largely due to their relatively high abundance, up to 150 ppm in primitive meteorites (Zhao et al., 2011; Leitner et al., 2012; Zhao et al., 2013), their relatively large size compared to other presolar grains, and their high abundance of trace elements.

Over 17,000 presolar SiC grains have been analysed to date (Hynes and Gyngard, 2009), with the majority of these grains being identified in meteoritic acid residues. Acid residues are typically produced following the 'Chicago Procedure' (Amari et al., 1994), which uses a series of harsh chemical treatments to produce nearly pure SiC fractions. However, it has been shown that these treatments can damage the surface of SiC grains (Stephan et al., 1997; Henkel et al., 2007a), resulting in important information about a grain's history being lost or altered. In order to avoid this damage, many studies have

sought to use alternative sample preparation techniques, choosing to separate grains without using harsh chemicals (Bernatowicz et al., 2003; Tizard et al., 2005), or measuring grains *in-situ* from polished meteorite sections (Besmehn and Hoppe, 2003; Nguyen et al., 2003; Nittler and Alexander, 2003; Nagashima et al., 2004; Nguyen and Zinner, 2004; Nittler, 2006; Yada et al., 2008; Hoppe et al., 2010; Zinner et al., 2010; Leitner et al., 2012; Leitner et al., 2016).

Additionally, the majority of the 17,000 grains were analysed using older ion probes, such as the Cameca IMS 3f/6f, which have relatively low spatial resolution (minimum $\sim 4\ \mu\text{m}$). Recent studies have measured grains with significantly higher spatial resolution, using instruments such as the Cameca NanoSIMS (Gyngard et al., 2006; Marhas et al., 2008; Heck et al., 2009; Croat et al., 2010; Bose et al., 2012; Hoppe et al., 2012; Leitner et al., 2012; Leitner et al., 2016; Hoppe et al., 2018).

The motivation for this study is the observation that presolar SiC grains, particularly mainstream and AB grains, measured with the NanoSIMS are found to have higher $^{14}\text{N}/^{15}\text{N}$ ratios on average compared to the Presolar Grain Database (Hynes and Gyngard, 2009) as a whole. Figure 5.1 shows data from the Presolar Grain Database with measurements obtained by NanoSIMS highlighted. Figure 5.2 shows the distribution of $^{14}\text{N}/^{15}\text{N}$ ratios which peaks at ~ 1000 for grains measured at high resolution, whereas the database for all measurements displays a distribution with a peak at ~ 500 .

Measurements of the $^{14}\text{N}/^{15}\text{N}$ ratios of presolar SiC grains are particularly important for models of stellar nucleosynthesis and so any potential effects which may distort the measured isotope ratios may be significant for comparison of models with measurement data. Many astrophysical models are not able to replicate the range of $^{14}\text{N}/^{15}\text{N}$ ratios seen in SiC grains (Huss et al., 1997; Amari et al., 2001c; Hedrosa et al., 2013; Zinner, 2014; Pignatari et al., 2015), meaning the sources of certain sub-groups, particularly AB grains, are difficult to resolve. It is possible that analyses using low resolution techniques, which often have a beam spot size much larger than the analysed grains, may be affected by contamination. As mainstream and AB SiC grains are highly depleted in ^{15}N , a very small amount of terrestrial contamination can result in much lower $^{14}\text{N}/^{15}\text{N}$ ratios. Grains are typically pre-sputtered before an analysis, which can remove the majority of potential

contaminants, but it is possible for the grain to trap material below it; as the grain is sputtered during an analysis, this contamination may be revealed.

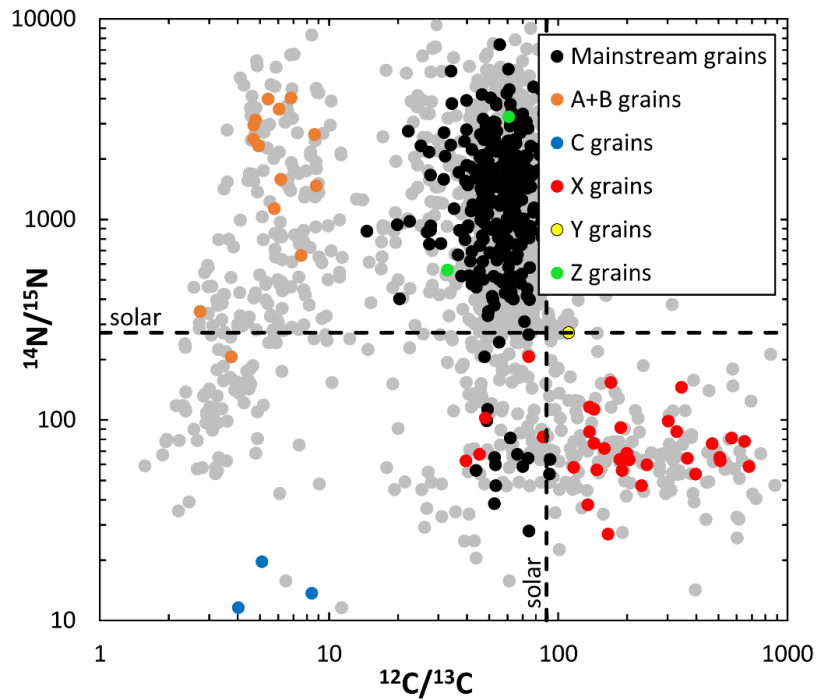


Figure 5.1: Carbon and nitrogen isotope ratios of presolar SiC grains. Coloured points are grains measured with high spatial resolution, whilst grey points are grains analysed with lower spatial resolution techniques. Data are from the Presolar Grain Database (Hynes and Gyngard, 2009).

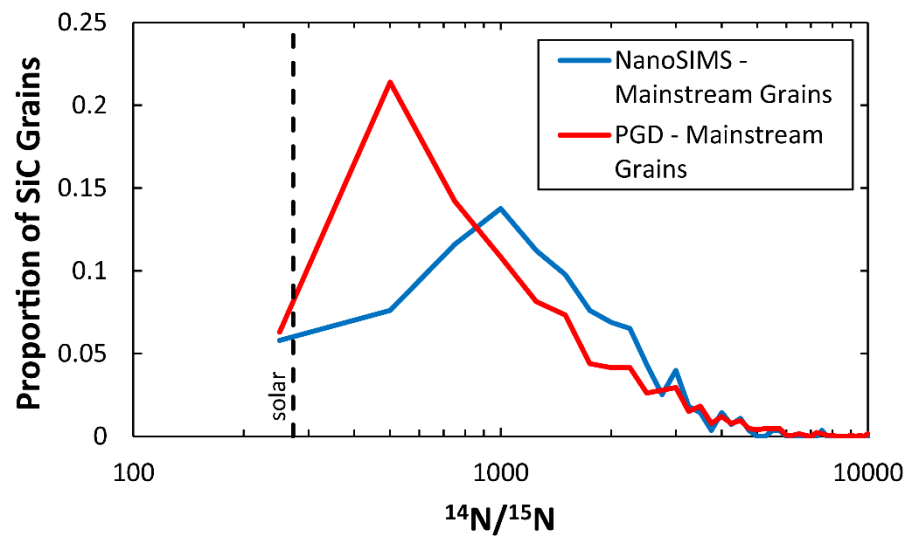


Figure 5.2: Histogram comparing the $^{14}\text{N}/^{15}\text{N}$ distribution of mainstream presolar SiC grains measured with different techniques. The red line indicates the overall distribution of mainstream SiC grains in the Presolar Grain Database (Hynes and Gyngard, 2009), whilst the blue line is a sub-set of this data, showing the distribution of $^{14}\text{N}/^{15}\text{N}$ ratios in mainstream grains analysed using the NanoSIMS.

In this work, 185 presolar SiC grains were analysed with high spatial resolution imaging of the grain, in order to determine whether any grains were isotopically heterogeneous, and to study and eliminate possible sources of contamination, the effects of different preparation methods, as well as isotopic fractionation effects that may bias the measured ratios from their true values. The aim was to discover whether the measured grains had the same $^{12}\text{C}/^{13}\text{C}$ and $^{14}\text{N}/^{15}\text{N}$ distribution as the 17000 grains in the Presolar Grain Database.

5.2 Experimental Methods

5.2.1 Sample Preparation

To compare the effects of different sample preparation methods, presolar silicon carbide grains were analysed *in-situ* from two polished meteorite sections, as well as from three acid residues.

Polished sections were prepared for two meteorites- Acfer 094 (ungrouped carbonaceous chondrite, petrologic type 2) and GRA 95229 (CR2 chondrite). Each section was prepared from ~200 mg chips of each meteorite, and was coated with a 10 nm platinum coat.

Three acid residues (KJG, JA-MM and JA-MM2) were acquired for this work, with each residue produced from pieces of Murchison meteorite (CM2 chondrite). Each residue was prepared following a similar method, although their compositions differ due to variations in the final steps of the methodology.

The KJG residue was produced using the 'Chicago Procedure' (Amari et al., 1994), which involves a series of harsh chemical and physical separation steps to produce a residue with a high abundance of silicon carbide grains. HF-HCl is used to dissolve the silicates which make up the bulk of the meteorite, whilst Cr_2O_7 , KOH and H_2O_2 are used to remove sulfur and kerogen. Density separation removes carbonaceous material such as graphite and nanodiamonds, before the SiC residue is separated into several size fractions. The KJG residue consists of grains in the 1.5-3 μm size range, and predominantly consists of SiC (73%), corundum (13%) and hibonite (5%) (Amari et al., 1994). The residue was provided as grains distributed over a 4x4 cm piece of gold foil; from this, a smaller sample (RL-1) was prepared for the purpose of this study. A 7x7 mm piece of high-purity gold foil was imprinted with a finder grid (copper H315, Agar Scientific), which allows grains to be

identified when analysing on multiple instruments. The foil was subsequently pressed into the KJG foil to transfer grains onto the new sample. To ensure the grains did not fall from the mount and were flat against the foil (in preparation for NanoSIMS analysis), the foil was pressed with a titanium carbide block.

Both JA-MM and JA-MM2 were produced following Amari et al. (1994)'s procedure (Russell et al., 1996). Whilst JA-MM2 has been through the same preparation procedures as the KJG residue, JA-MM was produced at an earlier stage in the method, meaning the residue contains minerals (such as spinel and graphite) which are not found in either KJG or JA-MM. Both JA-MM and JA-MM2 were provided as powders; a small aliquot of each was added to separate 1:1 mixtures of isopropanol and deionised water, and ultrasonicated for 5 minutes to disperse the grains through the liquid. Approximately 1 μ L of each mixture was distributed over 7x7 mm pieces of high purity gold foil, each of which had been imprinted with a finder grid (copper H315, Agar Scientific). Both JA-MM and JA-MM2 grains were pressed into the gold foil using a titanium carbide block to ensure the surface was flat, and to prevent grains from falling off the samples.

During this work, five presolar SiC grains were identified from the RL-1 sample using a FEI XL30 ESEM (Environmental SEM) at The University of Manchester. Large areas of RL-1 were searched, with EDX spectra collected for each grain in the area. SiC grains were selected based on the simultaneous detection of Si and C K α x-rays, and the absence of other peaks (particularly O K α). Following analysis with the NanoSIMS, the largest three of these grains were re-imaged using the ESEM in order to quantify the amount of material remaining for further analysis. Two of these grains, AC-KJG-2 and AC-KJG-3 were subsequently analysed using the TOF-SIMS (see Chapter 6, this thesis).

However, this method of presolar grain identification proved too time-consuming for this work. As a result, subsequent SiC grains were identified using other methods.

5.2.2 NanoSIMS Analysis

The remaining presolar SiC grains analysed in this work were identified with the use of a Cameca NanoSIMS 50L at The University of Manchester. Areas of high grain density were targeted on the acid residue samples (RL-1, JA-MM and JA-MM2), whilst searches for *in-situ* grains focused on the matrix material of the two polished sections (Acfer 094 and

GRA 95229). Prior to analysis, multiple 50x50 μm fields on each sample were pre-sputtered for ~5 minutes using a ~1.5 nA beam (D1-0 aperture, L1= 1600 V) to ensure a sputtering equilibrium was achieved. Automated image acquisition for a sequence of areas was acquired using the ‘chained analysis’ function on the NanoSIMS software.

Each 50x50 μm field was rastered using a ~1.6 pA Cs^+ beam (D1-2 aperture, ~250 nm spatial resolution) to produce secondary ion, each 512x512 pixels and comprised of ~5 frames added together) (see Figure 5.3). Ion images of $^{12}\text{C}^-$, $^{13}\text{C}^-$, $^{12}\text{C}^{14}\text{N}^-$, $^{12}\text{C}^{15}\text{N}^-$, $^{28}\text{Si}^-$, $^{29}\text{Si}^-$ and $^{30}\text{Si}^-$ were collected for the grains from KJG, JA-MM, Acfer 094, GRA 95229 and several of those from JA-MM2, whilst images of $^{12}\text{C}_2^-$, $^{12}\text{C}^{13}\text{C}^-$, $^{12}\text{C}^{14}\text{N}^-$, $^{12}\text{C}^{15}\text{N}^-$, $^{28}\text{Si}^-$, $^{29}\text{Si}^-$ and $^{30}\text{Si}^-$ were collected for the majority of the JA-MM2 grains. The detector configuration was altered during the course of this work to analyse molecular C isotopes rather than atomic ones, due to the increased yield of $^{12}\text{C}^{13}\text{C}^-$ ions (L. Nittler, 2016, pers. comm.). Presolar SiC grains from each field were identified based upon their anomalous isotope ratios of $\delta^{13}\text{C}$ and $\delta^{15}\text{N}$ which vary by several orders of magnitude, and $\delta^{29,30}\text{Si}$, which can vary by ~100‰ relative to solar compositions.

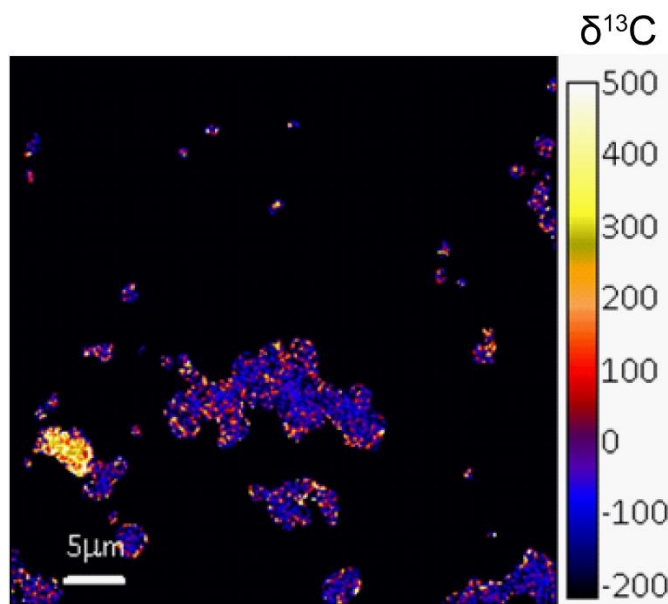


Figure 5.3: NanoSIMS image from a 50x50 μm search area. A presolar silicon carbide grain, in the bottom left corner, is identified by its $\delta^{13}\text{C}$ anomaly.

Each grain was analysed individually, typically with a field-of-view between 1-4 μm (depending on the grain size), and with high spatial resolution (typically 100-130 nm) using NanoSIMS apertures D1-5 (100 μm diameter) or D1-4 (150 μm diameter). Ion

images of $^{12}\text{C}^-$ (or $^{12}\text{C}_2^-$), $^{13}\text{C}^-$ (or $^{12}\text{C}^{13}\text{C}^-$), $^{12}\text{C}^{14}\text{N}^-$, $^{12}\text{C}^{15}\text{N}^-$, $^{28}\text{Si}^-$, $^{29}\text{Si}^-$ and $^{30}\text{Si}^-$, each 128x128 pixels and 10 frames, were collected for each grain (see Figure 5.4).

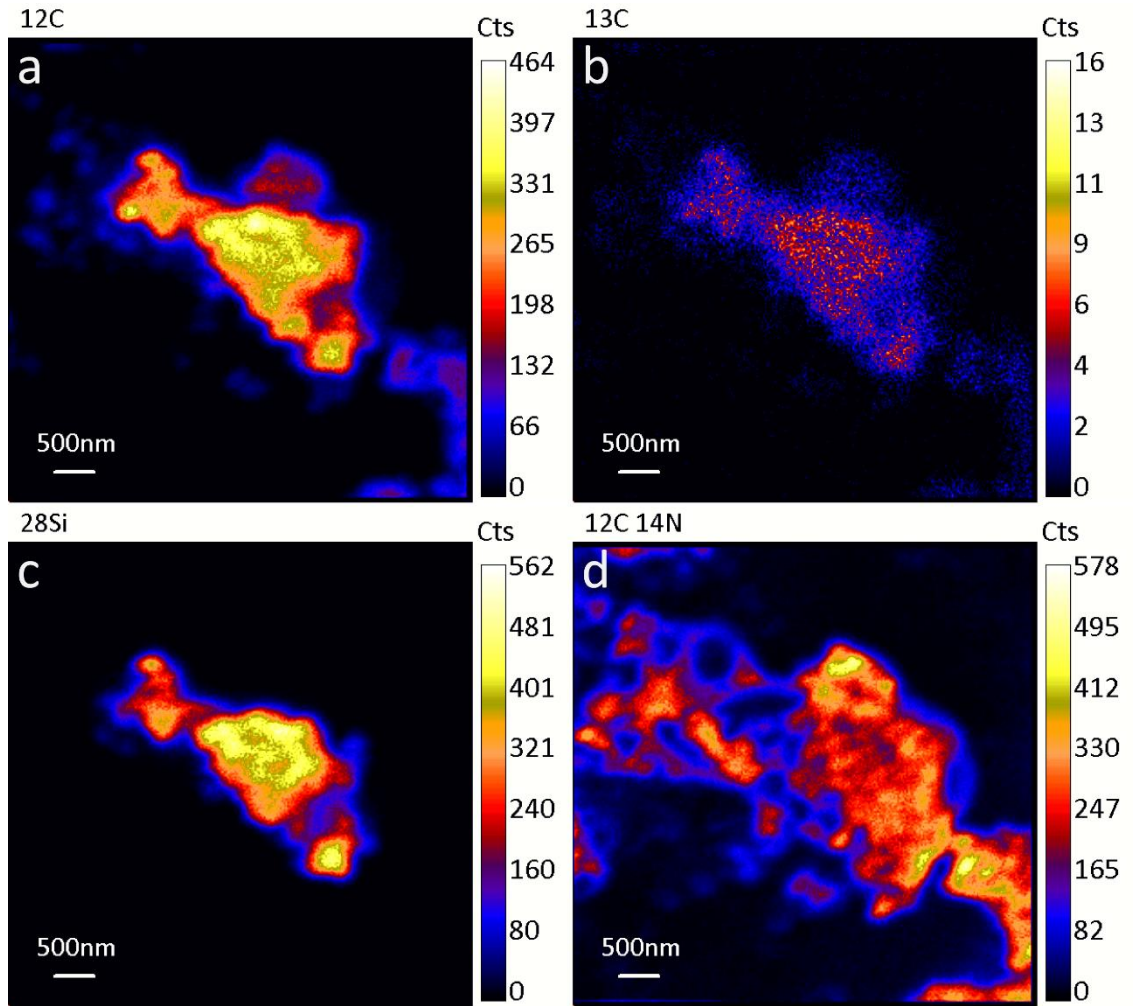


Figure 5.4: NanoSIMS ion images of a) ^{12}C , b) ^{13}C , c) ^{28}Si , and d) $^{12}\text{C}^{14}\text{N}$ from AC-MM-43, a mainstream presolar SiC grain from the JA-MM sample.

5.2.3 Data Reduction

Extraction of data from the NanoSIMS analyses was performed using the L'Image software (Larry Nittler, Carnegie Institution of Washington). Once loaded into the software, the individual frames of the ion images were aligned, which corrects for any drifting of the beam or stage which may occur during a measurement. The aligned images were combined to produce isotope ratio images (see Figure 5.5), from which Region(s) of Interest were drawn, so as to just extract data from the grain. ROIs were drawn at ~15% of total Si intensity, to minimise the inclusion of counts from the surrounding gold foil or minerals.

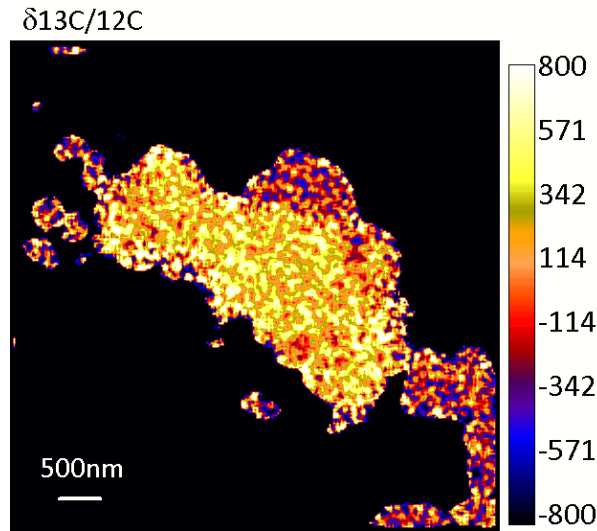


Figure 5.5: Isotope ratio image showing the $\delta^{13}\text{C}$ ratio of presolar SiC grain AC-MM-43.
 $\delta^{13}\text{C}$ values are quoted in per mil (‰).

During the analytical period, terrestrial silicon carbide grains were periodically analysed to determine the effects of instrumental mass fractionation on the measured isotope ratios, with the corrections applied to the measured isotope ratios of each grain. Whilst the absolute values of $\delta^{29,30}\text{Si}$, $\delta^{13}\text{C}$, and $\delta^{15}\text{N}$ are not known for these grains, they are assumed to be 0 ‰. This assumption should not affect the measured isotope ratios of the presolar grains, as any terrestrial variation in $\delta^{29,30}\text{Si}$, $\delta^{13}\text{C}$ and $\delta^{15}\text{N}$ is significantly smaller than the variation seen in presolar grains.

5.3 Results

In total, 185 presolar SiC grains were identified from the 5 samples: 20 from KJG, 45 from JA-MM, 88 from JA-MM2, 32 *in-situ* grains from Acfer 094, and 2 *in-situ* grains from GRA 95229. The C, N and Si isotope ratios of each of grain is presented in the Appendix of this thesis. As expected, the majority of the analysed grains were mainstream SiC grains, whilst 13 AB and 4 X grains were also identified. The analyses are presented graphically in Figure 5.6.

A total of 83900 μm^2 of GRA 95229 and 157900 μm^2 of Acfer 094 were searched for presolar SiC grains. GRA 95229 has a reported SiC abundance nearly twice that of Acfer 094 (Newton et al., 1995; Davidson et al., 2009), meaning it would have been expected to identify significantly more SiC grains than the two that are presented in this work.

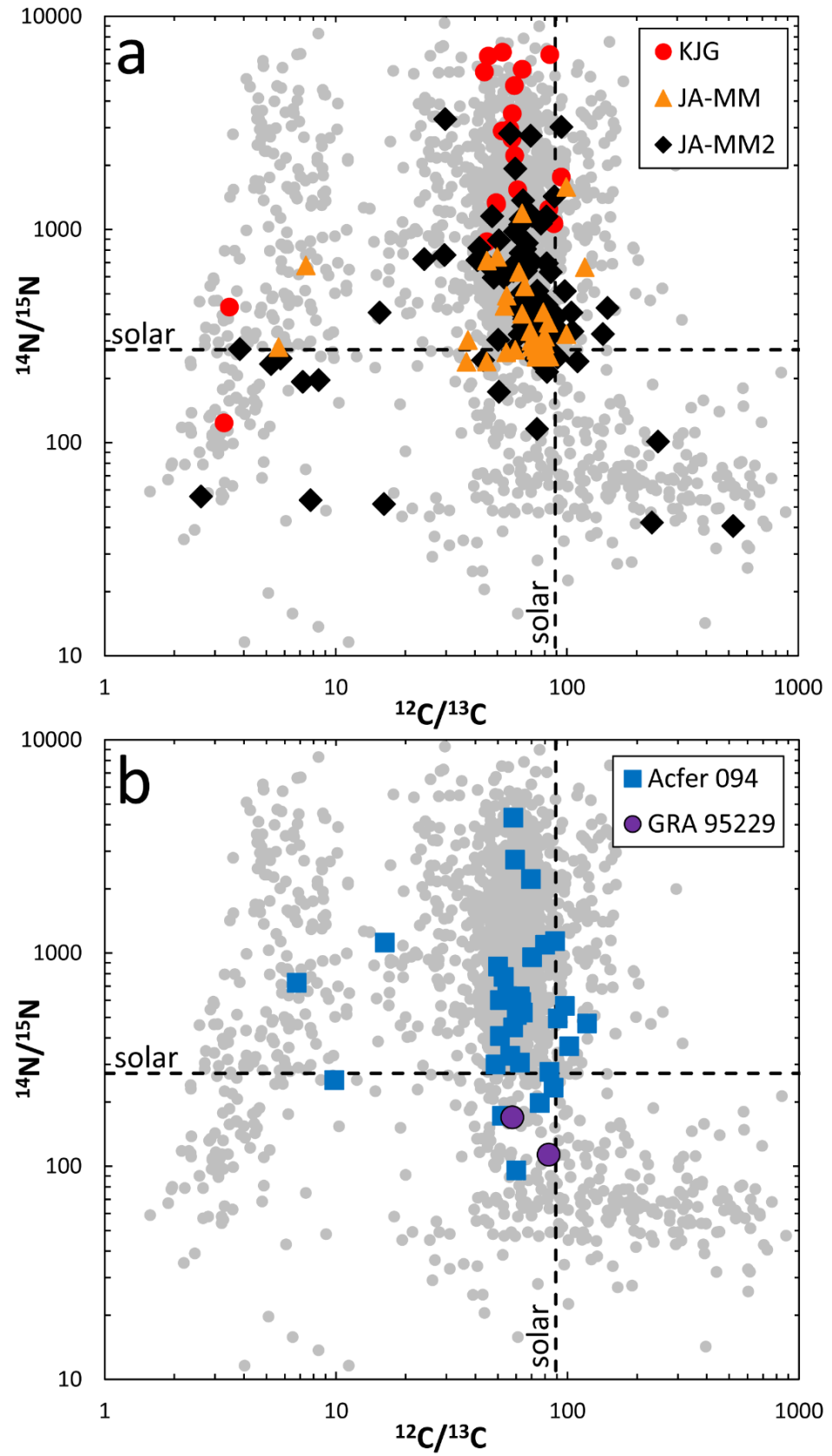


Figure 5.6: Plots showing the carbon and nitrogen isotope ratios of a) acid residue, and b) in-situ presolar SiC grains. Grey points are literature data from the Presolar Grain Database (Hynes and Gyngard, 2009).

5.4 Discussion

5.3.1 Carbon and Nitrogen Isotopes

5.3.1.1 Acid Residue Grains

As can be seen in Figure 5.6, the acid residue and *in-situ* grains have similar distributions in their carbon and nitrogen isotope ratios, and the distributions are comparable with literature data from the Presolar Grain Database (Hynes and Gyngard, 2009). There are however, significant differences in the carbon and nitrogen ratios of grains from each sample, particularly for the grains from the three acid residues- KJG, JA-MM and JA-MM2.

As Figure 5.6 shows, the mainstream grains from the KJG residue have, on average, $^{14}\text{N}/^{15}\text{N}$ ratios which are almost an order of magnitude higher than the majority of those measured in the JA-MM and JA-MM2 grains. Additionally, the AB grains from KJG have slightly lower $^{12}\text{C}/^{13}\text{C}$ ratios than all except one of the AB grains from JA-MM and JA-MM2, although it is difficult to determine if this is a true variation between the samples, as a total of 11 AB grains from the three residues is not a statistically significant sample size.

As all three residues were produced from pieces of the Murchison meteorite, it is unlikely that the differing $^{14}\text{N}/^{15}\text{N}$ (and perhaps $^{12}\text{C}/^{13}\text{C}$) ratios are the result of sample selection. Assuming the high $^{14}\text{N}/^{15}\text{N}$ ratios measured in the KJG grains represent the 'real' isotopic compositions expected for high spatial resolution analyses (as with Figures 5.1 and 5.2), it is possible that grains from the JA-MM and JA-MM2 residues may have been contaminated with terrestrial material, bringing their isotope ratios closer to solar values.

As mainstream SiC grains are typically highly depleted in ^{15}N , a small proportion of terrestrial contamination can significantly reduce the measured $^{14}\text{N}/^{15}\text{N}$ ratio. As the KJG grains have $^{12}\text{C}/^{13}\text{C}$ and $^{14}\text{N}/^{15}\text{N}$ ratios which fall at the extreme end of those seen in the Presolar Grain Database, it can be assumed that the measured ratios of those grains are real. As a result, the KJG grains can be used to determine the amount of terrestrial contamination which would be required to produce the low $^{14}\text{N}/^{15}\text{N}$ ratios seen in the majority of JA-MM and JA-MM2 grains.

On average, the KJG grains have a $^{14}\text{N}/^{15}\text{N}$ ratio of ~ 5000 , whilst the terrestrial nitrogen ratio is ~ 272 . Based upon these compositions, approximately 0.05% of the ^{15}N must be derived from terrestrial contamination to produce a measured $^{14}\text{N}/^{15}\text{N}$ ratio of <1000 (see

Figure 5.7), which represents the upper range of both the JA-MM and JA-MM2 grains. The amount of contamination required drops to ~0.035% if a starting $^{14}\text{N}/^{15}\text{N}$ ratio of 2000 (the lower range of the KJG grains) is used.

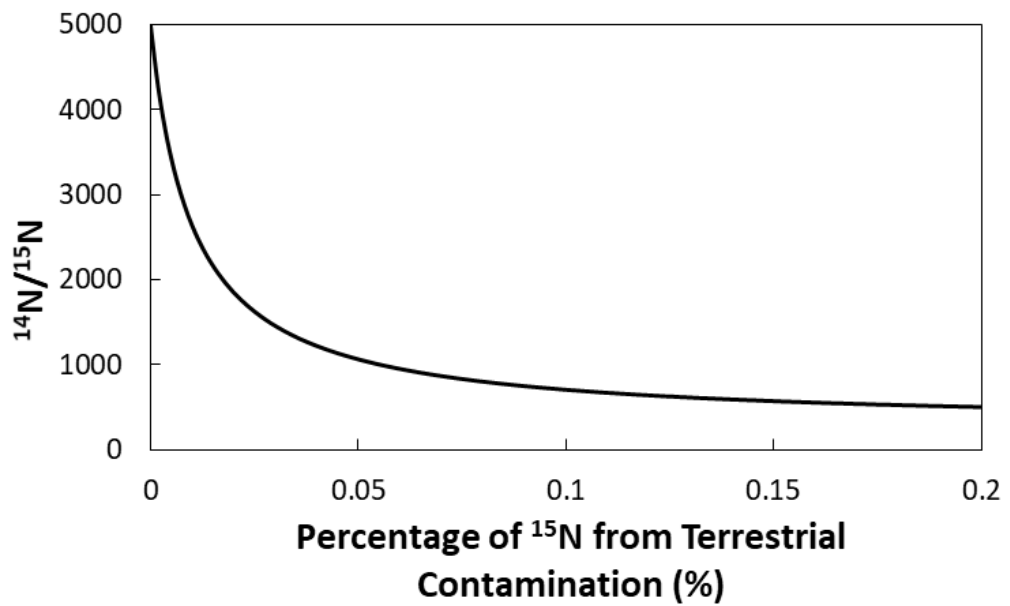


Figure 5.7: The effect of terrestrial contamination on the $^{14}\text{N}/^{15}\text{N}$ ratio of a mainstream presolar SiC grain. It is assumed the SiC grain has an initial $^{14}\text{N}/^{15}\text{N}$ ratio of 5000. When 0.2% of ^{15}N is derived from terrestrial contamination, the contaminants make up ~50% of the total atoms in the grain.

Every effort was made to eliminate potential contamination during the sample preparation and analysis phases of this work. Each grain was pre-sputtered prior to analysis, which would be expected to remove any material sitting on the surface of the grain. It is also possible that contaminants could have been trapped under the grains; whilst the pre-sputtering would not remove this material, it would be expected that the contamination would be revealed as the grains were sputtered during the analysis. High spatial resolution measurements, with careful inspection of the images for any evidence of differing nitrogen abundance or isotope composition towards the edge of the grain, and acquisition of isotope analyses from the central area of the image, were used to attempt to eliminate this possible source of contamination. It would also be expected that, as all three samples, KJG, JA-MM and JA-MM2, were prepared and analysed in the same way, then the KJG grains would also be affected if this possible source of contamination of grains was significant.

A more likely origin for any contamination is the extraction procedure which produced the two residues. As with the KJG grains, both JA-MM and JA-MM2 were produced following the 'Chicago Procedure' (Amari et al., 1994; Russell et al., 1996). As both JA-MM and JA-MM2 were affected, it is likely that any contaminants would have been introduced early in the methodology, perhaps during one of the chemical treatments (HF-HCl, Cr₂O₇, KOH, H₂O₂ etc.). Contamination could be introduced in two different ways during this procedure: insufficient cleaning of the residues, or etching of grain surfaces, although no nitrogen-bearing reagents were reported as being used in the procedure.

Following chemical treatments, each residue was cleaned to remove any remaining material from the grain surfaces (Russell et al., 1996). Although thorough, it is possible for a chemical residue to be left behind on the grains, leaving a thin coating with a terrestrial isotopic composition. Previous studies have noted that the Chicago Procedure can etch the grains, depositing solar-composition meteorite matrix material into the grain surface (Stephan et al., 1997; Henkel et al., 2007a). During an analysis, the presence of either a chemical residue or matrix material would lower the bulk ¹⁴N/¹⁵N ratio of a grain. However, any coating or surface etching would be rapidly sputtered during NanoSIMS analyses, revealing the true isotopic composition underneath.

5.3.1.2 In-Situ Grains

As with the acid residue grains, there are some noticeable differences in the carbon and nitrogen isotope ratios of the *in-situ* grains from Acfer 094 and GRA 95229 (see Figure 5.6). Only two presolar SiC grains, both mainstream, were identified from GRA 95229, but both have considerably lower ¹⁴N/¹⁵N ratios than the grains from Acfer 094. Although data from two grains is not sufficient to draw statistically significant conclusions, it does suggest that there could be differences between grains from the two samples.

Whilst the mainstream grains from Acfer 094 fit well with the literature data from the Presolar Grain Database (Hynes and Gyngard, 2009), the majority of grains cluster at lower ¹⁴N/¹⁵N ratios (see Figure 5.6). Assuming this is a real distribution, and not a statistical effect of only 30 mainstream grains having been analysed from this sample, there are two possible explanations: contamination with material of a terrestrial ¹⁴N/¹⁵N composition, or isotopic dilution from surrounding grains.

The polished sections of both Acfer 094 and GRA 95229 were prepared in a clean laboratory environment, with every effort taken to minimise contamination; all equipment was thoroughly cleaned with acetone prior to potting and polishing the sample, and care was taken to select a polishing medium which would not interfere with the isotope ratios of interest. Whilst terrestrial contamination cannot be completely ruled out, its effect is likely to be minimal. As each of these samples was prepared as a polished section, any contamination would be likely to present as a thin surface layer, which would be rapidly sputtered away during NanoSIMS analysis, revealing the true isotopic composition beneath.

As with the acid residue grains, the proportion of contamination necessary to reproduce these compositions can be estimated using a simple model. Three mainstream grains from Acfer 094 are found at higher $^{14}\text{N}/^{15}\text{N}$ ratios between 2000-5000. Using these compositions as an estimate for non-contaminated grain compositions, it can be determined that 0.04-0.05% of the ^{13}C would need to be derived from solar or terrestrial composition material to lower the $^{14}\text{N}/^{15}\text{N}$ ratio to <1000 (see Figure 5.7). This proportion increases to 0.1% when attempting to produce a nitrogen ratio of ~700- the approximate average of the mainstream grains from Acfer 094.

Alternatively, the low nitrogen ratios could be an isotopic dilution effect due to insufficient spatial resolution during the analyses. Although the NanoSIMS measurements were carried out with very high spatial resolution (typically ~100 nm), many of the grains are 100-500 nm in size. Even with such high spatial resolution, it is possible that secondary ions from the surrounding minerals, which are solar in composition, could have been detected, resulting in lower $^{14}\text{N}/^{15}\text{N}$ ratios than expected.

If the measurements were affected by isotopic dilution from surrounding minerals, it would be expected to find a correlation between the grain size and the measured $^{14}\text{N}/^{15}\text{N}$ ratio. Smaller grains would be expected to be most influenced by insufficient spatial resolution, with lower $^{14}\text{N}/^{15}\text{N}$ ratios measured as a result. As Figure 5.8 shows, there is no apparent correlation between these two variables. This suggests that despite the small size of many of the *in-situ* grains measured in this study, the spatial resolution was sufficient to minimise any contribution from the surrounding mineralogy.

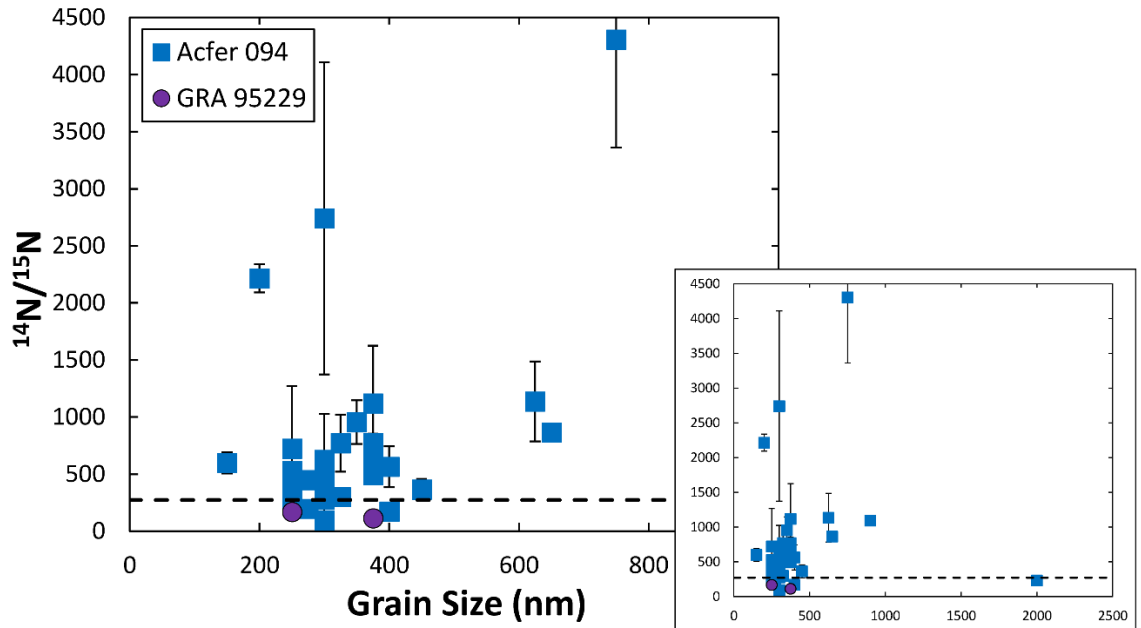


Figure 5.8: Plot showing the relationship between the $^{14}\text{N}/^{15}\text{N}$ composition and grain size of the presolar SiC grains measured in-situ from both Acfer 094 and GRA 95229.

The AB grains examined in this study also exhibit slight differences in their $^{12}\text{C}/^{13}\text{C}$ distributions (see Figure 5.9). Whilst the AB grains from the three acid residues span the range of carbon compositions seen in the literature, the two AB grains from Acfer 094 are found at slightly higher $^{12}\text{C}/^{13}\text{C}$ ratios. However, as only 2 of the 13 AB grains identified in this work were found in Acfer 094, it is difficult to determine whether this represents a real trend, or is simply an effect of an insufficient sample size. Assuming that the higher $^{12}\text{C}/^{13}\text{C}$ ratios are representative of AB grains from the sample, it is possible that the grains may have been affected by either contamination or isotopic dilution.

As with the nitrogen isotope ratios, it is possible to estimate the proportion of terrestrial or solar composition material which would be required to reproduce the marginally higher $^{12}\text{C}/^{13}\text{C}$ ratios of the AB grains from Acfer 094. Presolar SiC AB grains are highly enriched in ^{13}C , meaning a large amount of contamination is required to significantly increase the $^{12}\text{C}/^{13}\text{C}$ ratio.

The KJG grains have a $^{12}\text{C}/^{13}\text{C}$ ratio of ~ 3 , whilst the terrestrial carbon ratio is ~ 89 . As the model in Figure 5.10 shows, over 0.12% of the ^{13}C must be derived from terrestrial contaminants to reproduce the composition of the grains from Acfer 094, meaning over half the atoms in the grain would originate from the contaminant. Such a high proportion of contamination or isotope dilution seems unlikely, even when grains of 100-200 nm in

size are analysed. It is therefore more likely that the higher $^{12}\text{C}/^{13}\text{C}$ ratios of the Acfer 094 grains are better explained by an insufficient sample size of AB grains.

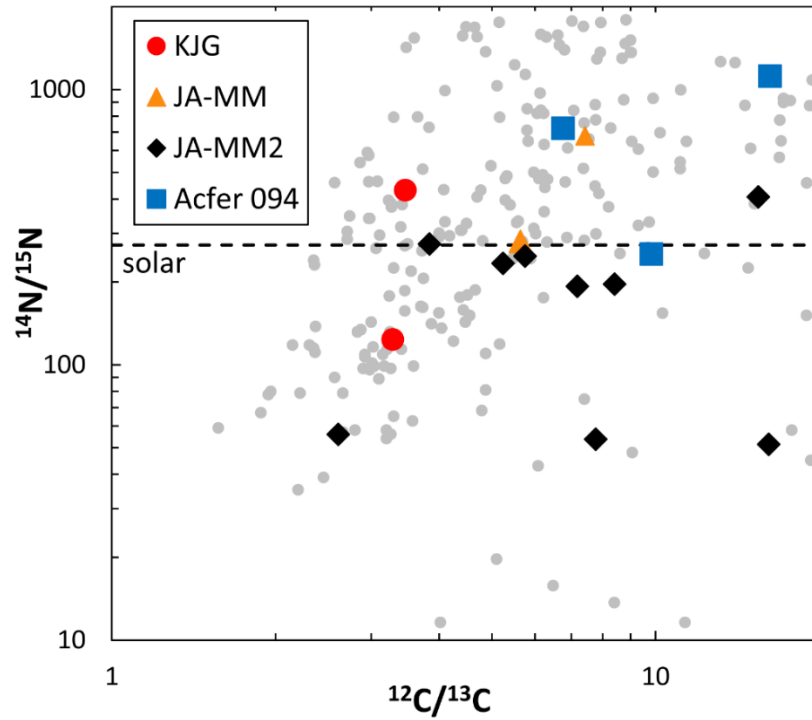


Figure 5.9: Carbon and nitrogen isotope ratios of type AB presolar SiC grains measured in this study. AB grains are typically defined as having $^{12}\text{C}/^{13}\text{C} < 10$. Grey points are literature data from the Presolar Grain Database (Hynes and Gyngard, 2009).

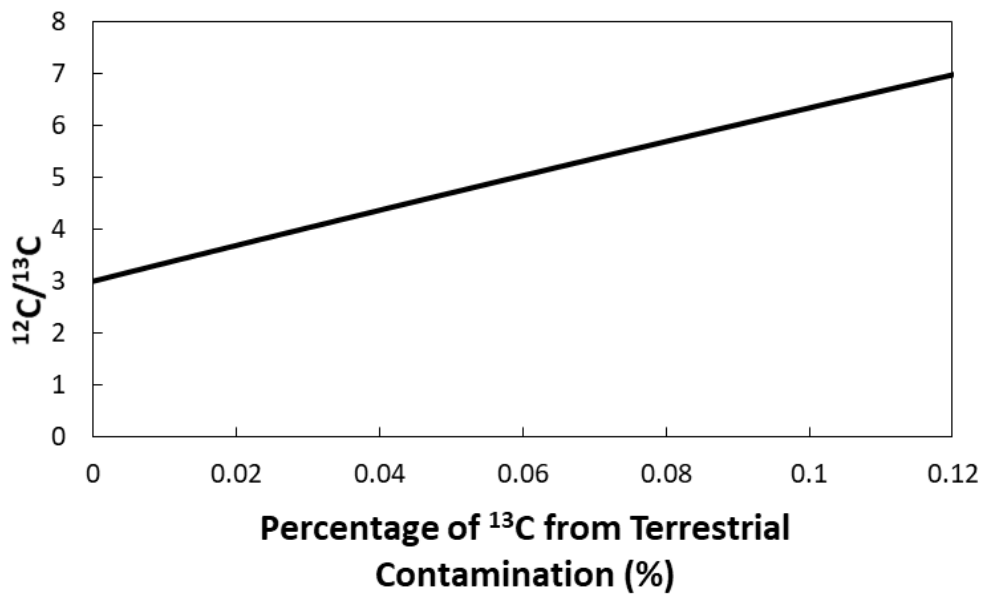


Figure 5.10: The effect of terrestrial/solar contamination on the $^{12}\text{C}/^{13}\text{C}$ ratio of a type AB presolar SiC grain. It is assumed that the SiC grain has an initial $^{12}\text{C}/^{13}\text{C}$ ratio of 3. When $\sim 0.11\%$ of ^{13}C is derived from terrestrial contamination, the contaminants make up $\sim 50\%$ of the total atoms in the grain.

5.3.2 Silicon Isotopes

Both the acid residue and *in-situ* presolar SiC grains measured in this study have very similar Si isotope distributions (see Figure 5.11), which fit well with literature data from the Presolar Grain Database (Hynes and Gyngard, 2009). In contrast to the carbon and nitrogen isotope ratios, there are no significant variations in the Si isotopes of SiC grains from different samples.

Previous studies have determined that mainstream presolar SiC grains lie on a slope of ~ 1.3 on a silicon three-isotope plot, as a result of Galactic Chemical Evolution (GCE) (Alexander and Nittler, 1999). Overall, the mainstream grains measured in this work fall on a slope of ~ 1 , although there are notable differences between grains from individual samples.

As only two grains were identified from GRA 95229, no trendline was calculated for this sample. Mainstream grains from both the KJG residue and Acfer 094 agree well with the literature data, lying along slopes with gradients of 1.32 and 1.26 respectively, although Acfer 094 displays more scatter around this trend. The trend of grains from both JA-MM and JA-MM2 are significantly shallower than those defined by the literature, with gradients of 0.59 and 1.07 respectively. It should however be noted that these samples display the most scatter and therefore low correlation, with R^2 values < 0.5 .

All three acid residues, KJG, JA-MM and JA-MM2, were produced from pieces of the Murchison meteorite. Additionally, the majority of SiC grains in the literature also originate from this meteorite. For this reason, any fractionation of Si isotopes in the JA-MM and JA-MM2 grains must have been caused by processes in the laboratory, perhaps by contamination during the sample preparation phase.

Whilst C and N are common contaminants on the gold foil on which the grains are placed, silicon is rare. The SiC grains measured *in-situ* are more likely to have been affected, either by contamination on the surface of the polished section, or by isotopic dilution from the surrounding silicate minerals which form the matrix of most meteorites. The silicon isotopes would be expected to be correlated, meaning any dilution from surrounding minerals would move the $\delta^{29}\text{Si}$ and $\delta^{30}\text{Si}$ ratios along a slope.

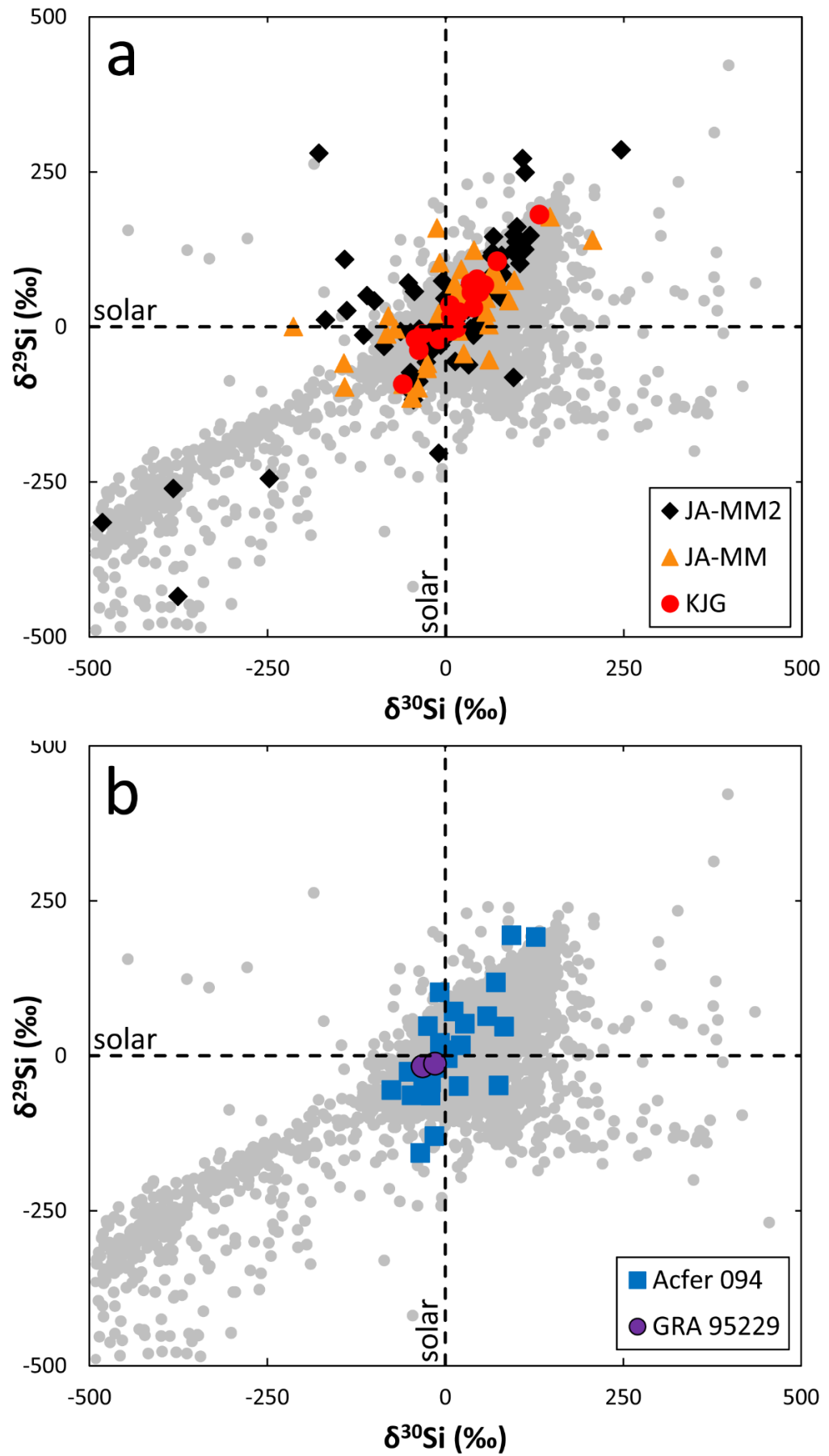


Figure 5.11: Silicon three-isotope plots of the a) acid residue, and b) in-situ presolar SiC grains analysed in this work. Grey points are literature data from the Presolar Grain Database (Hynes and Gyngard, 2009).

Assuming an arbitrary grain composition of $\delta^{30}\text{Si} = \sim 100\text{‰}$ and $\delta^{29}\text{Si} = \sim 130\text{‰}$ (based on a slope of ~ 1.3), contamination or dilution from terrestrial or solar composition material ($\delta^{29,30}\text{Si} = 0\text{‰}$) would reduce the measured $\delta^{29}\text{Si}$ and $\delta^{30}\text{Si}$ ratios along a slope with a gradient of ~ 1.3 (see Figure 5.12). As this gradient is the same as that predicted by GCE, it cannot explain the shallower trends of the grains from both JA-MM and JA-MM2. It is possible that analysis of additional grains may reduce the scatter and further improve the definition of these trends, perhaps improving their correlation with the literature data.

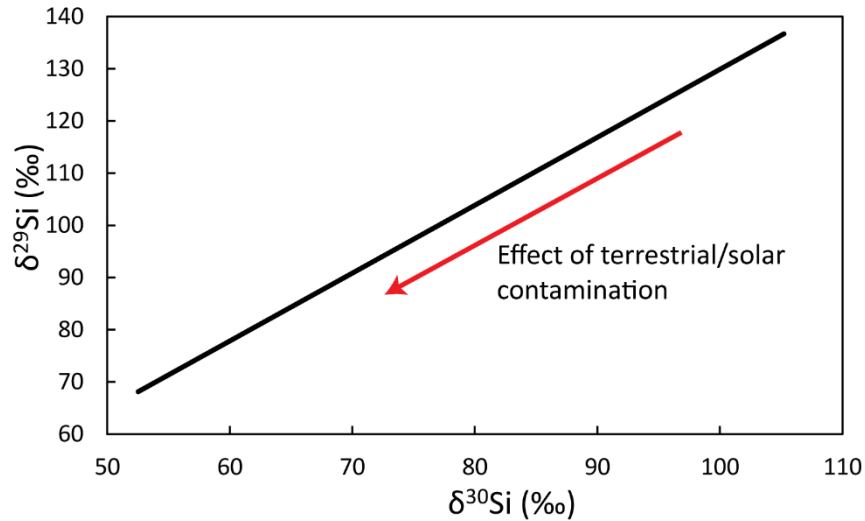


Figure 5.12: The effect of solar composition ($\delta^{29,30}\text{Si} = 0\text{‰}$) contamination on the $\delta^{29}\text{Si}$ and $\delta^{30}\text{Si}$ ratios of a mainstream presolar SiC grain. It is assumed that the SiC grain has a composition of $\delta^{29}\text{Si} \sim +100\text{‰}$ and $\delta^{30}\text{Si} \sim +130\text{‰}$.

As this gradient also represents the effect of isotopic dilution on *in-situ* grains, this method cannot be used to determine whether the grains from Acfer 094 and GRA-95229 were affected by dilution. As with the nitrogen ratios, it would be expected to find a correlation between the measured $\delta^{29,30}\text{Si}$ ratios and the grain size. Insufficient spatial resolution would be expected to have a greater influence on smaller grains, resulting in lower silicon isotope ratios. As Figure 5.13 shows, there is no correlation between the grain size and either $\delta^{29}\text{Si}$ or $\delta^{30}\text{Si}$, suggesting that the spatial resolution was high enough to minimise the contribution of secondary ions from the surrounding silicate minerals.

As neither terrestrial contamination can adequately explain the variation between samples, it is possible that the samples contain different populations of SiC grains. However, each of the three acid residues were produced from the same meteorite,

suggesting they should contain similar populations, unless altered by later processes in the laboratory.

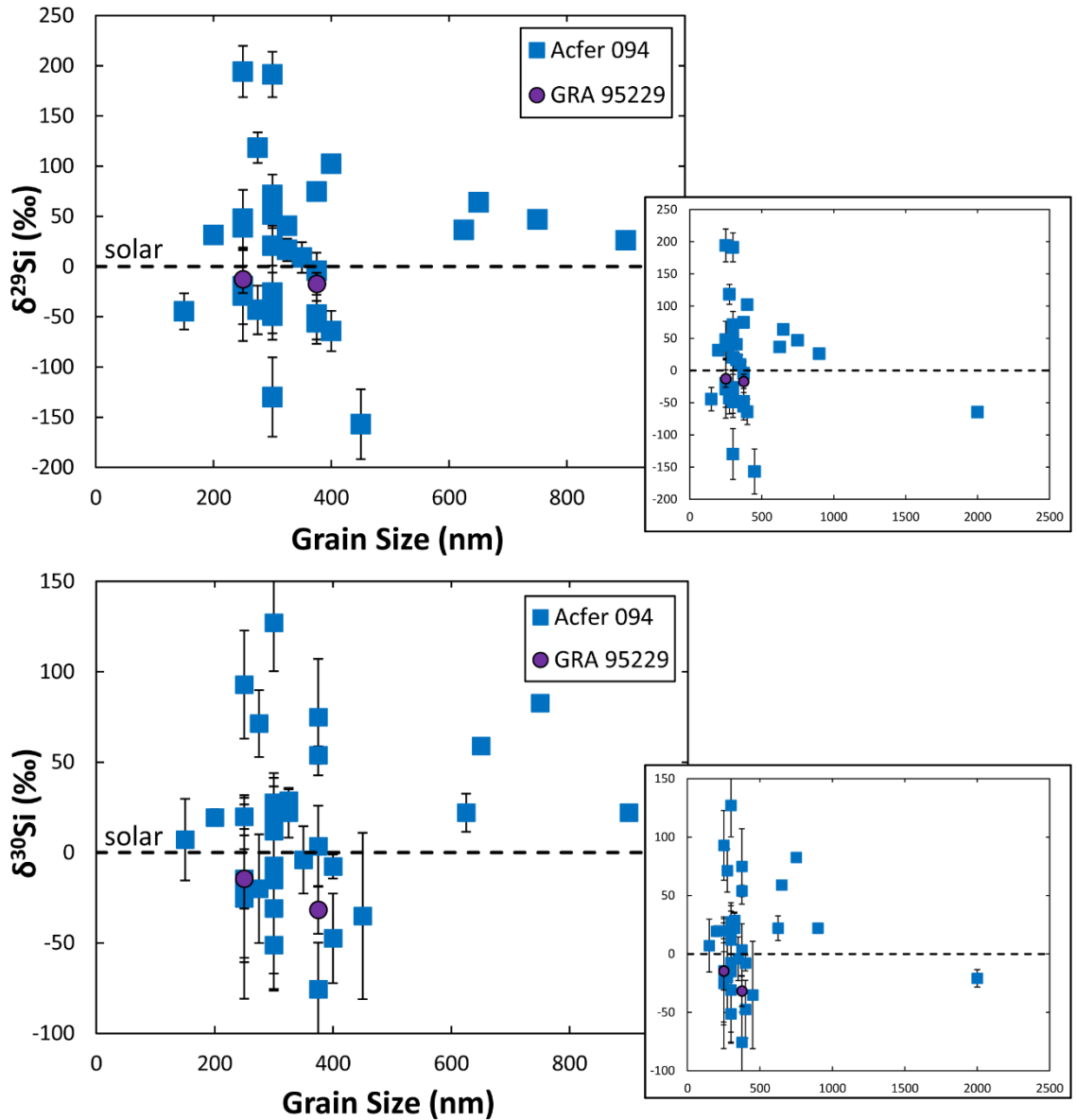


Figure 5.13: Plot showing the relationship between $\delta^{29,30}\text{Si}$ and the grain size of the presolar SiC grains measured in-situ from both Acfer 094 and GRA 95229.

5.4 Conclusions

Overall, the measured carbon, silicon and nitrogen isotope ratios of both acid residue and *in-situ* grains fit reasonably well with the literature data, although there are some notable differences between the grains from individual samples.

The mainstream grains from the KJG residue are typically found to have higher $^{14}\text{N}/^{15}\text{N}$ ratios than the grains from the other samples, with compositions towards the upper

range of that defined by the literature data. These ratios are consistent with those measured in other grains using high spatial resolution techniques. In contrast, the mainstream grains from JA-MM, Acfer 094 and GRA 95229 have $^{14}\text{N}/^{15}\text{N}$ ratios an order of magnitude lower on average. Models suggest that a relatively high proportion of terrestrial contamination would be required to reproduce these compositions. Additionally, the *in-situ* grains do not seem to have been affected by isotopic dilution from surrounding material.

Whilst the Si isotope distributions are similar for each sample, the mainstream grains from both JA-MM and JA-MM2 lie on slopes with significantly shallower gradients than those defined by the literature, as well as the other samples in this work. The apparent fractionation of the Si isotopes cannot be explained by either contamination or isotopic dilution, and is instead more likely an artefact caused by the scatter that each of these samples displays.

Whilst the differences between the grain populations from each sample are small, the variation cannot be sufficiently explained by either contamination or isotopic dilution. Further study of these samples, particularly *in-situ* grains would assist in determining whether the variation is due to insufficient sample size, or represents a true difference in the grain populations from different samples.

Acknowledgements

We thank Roy Lewis, John Arden and Addi Bischoff for the provision of the KJG, JA-MM/MM2 and Acfer 094 samples used in this work. US Antarctic meteorite samples are recovered by the Antarctic Search for Meteorites (ANSMET) program which has been funded by NSF and NASA, and characterised and curated by the Department of Mineral Sciences of the Smithsonian Institution and Astromaterials Curation Office at NASA Johnson Space Center.

Chapter 6

A Comprehensive Analysis of Ten Presolar Silicon Carbide Grains

Ten presolar silicon carbide grains were analysed for their major and trace element compositions using both Time-of-Flight Secondary Ion Mass Spectrometry (TOF-SIMS) and NanoSIMS. Carbon, nitrogen and silicon isotope ratios suggest that seven of these grains are mainstream, whilst one AB and two X grains were also identified. Four of the grains were depth-profiled. This work is a development of an analytical technique, however although the TOF-SIMS measurements were carried out with the maximum possible spatial resolution, many of the grains had significant contributions to their trace element inventories from nearby grains. As a result, the background abundances for many elements cannot be reliably determined.

6.1 Introduction

Presolar grains are stellar condensates which formed in the outflows or ejecta of dying stars, prior to the formation of the solar system. Following their formation, they resided in the interstellar medium (ISM) for over 500 Myr (Jones et al., 1997) before being incorporated into bodies such as asteroids, interplanetary dust particles (IDPs) and comets (Huss and Lewis, 1995; Messenger et al., 2003; Messenger et al., 2005; McKeegan et al., 2006; Zinner, 2014) during solar system formation. Their long history in the interstellar medium mean that many processes, such as interaction with galactic cosmic rays, UV radiation, supernovae shockwaves, vaporisation and recondensation, the formation of surface ices, collisions with other grains or gas molecules, and implantation of ions or atoms into the grain surface layers may have modified their original isotopic and elemental compositions (Huss and Lewis, 1995; Jones et al., 1997; Alexander and Nittler, 1999; Ehrenfreund and Charnley, 2000; Verchovsky et al., 2001; Bernatowicz et al., 2003; Lyon et al., 2007).

Most analyses of trace elements in SiC grains (Virag et al., 1992; Hoppe et al., 1994; Amari et al., 1995; Hoppe et al., 1996b; Gyngard et al., 2006; Huss and Smith, 2007; Marhas et

al., 2007; Marhas et al., 2008) have been carried out using ion probes, such as the NanoSIMS. Whilst these instruments are capable of determining high resolution isotope ratios for many trace elements, they are highly destructive and can only analyse 5-7 ionic species in each measurement. As a result, it is difficult to determine the composition of more than a few trace elements in each SiC grain. More recently, RIMS (Resonance Ionization Mass Spectrometry), particularly CHILI (Chicago Instrument for Laser Ionization) (Stephan et al., 2016b), has been used to analyse the composition of several elements in SiC grains (Davis et al., 2015; Stephan et al., 2015a; Stephan et al., 2015b; Stephan et al., 2016a; Trappitsch et al., 2016a; Trappitsch et al., 2016b; Stephan et al., 2017). Although CHILI is currently only capable of determining the isotopic compositions of Sr, Ba, Fe and Ni, it is significantly less destructive than conventional ion probes, meaning enough material is usually left for analysis with other techniques.

An alternative technique for trace element analysis is Time-of-Flight Secondary Ion Mass Spectrometry (TOF-SIMS). TOF-SIMS is capable of analysing the entire mass spectrum in a single measurement, allowing isotopic and elemental abundances of both major and trace elements to be determined (Stephan and Jessberger, 1996; Stephan et al., 1997). The instrument uses a pulsed primary ion beam, which results in high mass resolution and minimal sample consumption. It is possible to perform repeated measurements, in order to build up elemental and isotopic depth profiles of an individual grain (Lyon et al., 2007; King et al., 2012).

Although TOF-SIMS is useful for determining abundances of many trace elements present in presolar SiC grains, it is unable to determine high precision isotope ratios of C, N and Si, which are necessary for determining a grain's stellar origin. Without knowing a grain's source, trace element compositions cannot be applied to stellar models, meaning a grain's history cannot be fully explored.

This work comprehensively analyses the trace element composition of eight presolar silicon carbide grains, in order to provide an insight into their complicated processing history. Trace element depth profiles for several elements were produced for two of the grains by repeated measurements using TOF-SIMS, in order to identify any heterogeneity through each grain. Additionally, high precision isotope ratios of C, Si and N were

determined using the NanoSIMS, in order to ascertain the sub-group to which each grain belongs, and therefore the stellar source from which they originated.

6.2 Experimental Methods

6.2.1 Sample Preparation

Presolar silicon carbide grains were identified from the KJG and JA-MM2 acid residues (Amari et al., 1994; Russell et al., 1996). Each of these residues were produced from the Murchison meteorite (CM2) following the 'Chicago Procedure', which uses a series of chemical and physical separation treatments to produce a residue with a high yield of SiC grains (Anders and Zinner, 1993; Amari et al., 1994). The sample preparation procedures are described in Chapter 3 of this thesis.

Presolar SiC grains from the KJG residue were identified using a FEI XL30 ESEM (Environmental Scanning Electron Microscope) at The University of Manchester, which is equipped with Secondary Electron (SE), Backscattered Electron (BSE), and Energy Dispersive X-ray (EDX) detectors. SiC grains were identified by peaks in Si (and sometimes C), and an absence of O, in their EDX spectra. SE and BSE images were collected at a range of magnifications so each grain could be relocated on both the NanoSIMS and TOF-SIMS. Several grains from the KJG residue were identified in this way but only two, AC-KJG-2 and AC-KJG-3 (Figure 6.1), were large enough for TOF-SIMS analysis, which typically requires grains to be at least 1 μm in size.

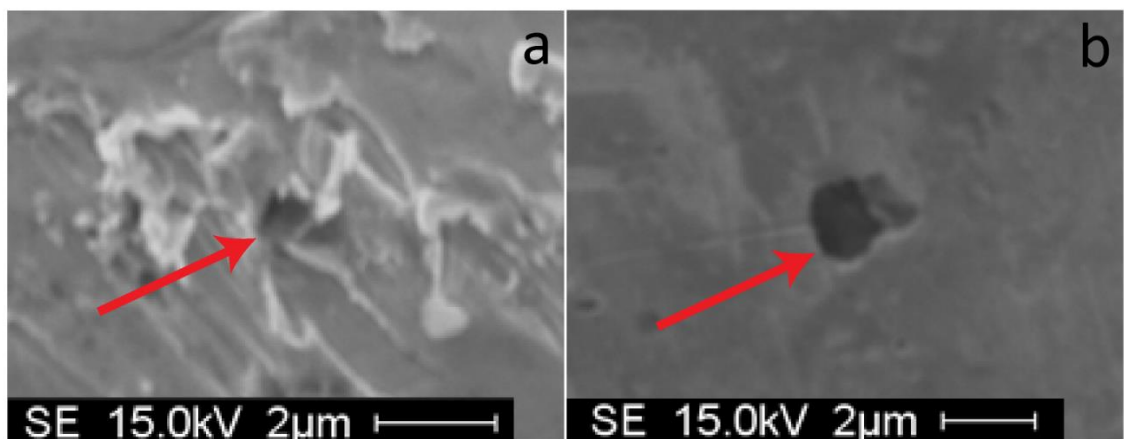


Figure 6.1: Secondary Electron (SE) image of a) AC-KJG-2, and b) AC-KJG-3. SE images were collected prior to any destructive analyses using a FEI XL30 ESEM.

As this method of identifying presolar SiC grains proved to be too time-consuming, SiC grains from the JA-MM2 residue were identified using the Cameca NanoSIMS 50L at The University of Manchester. High grain density regions of the sample were analysed with large ($\sim 30\ \mu\text{m}$) fields-of-view in order to identify isotopically anomalous grains. This process has been described in Chapter 5 of this thesis.

6.2.2 NanoSIMS

Five grains from the JA-MM2 residue (AC-MM2-1, AC-MM2-41, AC-MM2-82, AC-MM2-86 and AC-MM2-87), as well as the two KJG grains (AC-KJG-2 and AC-KJG-3) were analysed with a small field-of-view (between $1\text{--}5\ \mu\text{m}$, depending on grain size) and high spatial resolution ($\sim 100\ \text{nm}$, D1-5 aperture). A $10\ \mu\text{m}$ field over each grain was pre-sputtered for ~ 3 minutes using a $\sim 10\ \text{pA}$ Cs^+ beam (D1-1 aperture), so as to ensure a sputtering equilibrium was achieved. Ion images of $^{12}\text{C}^-$, $^{13}\text{C}^-$, $^{12}\text{C}^{14}\text{N}^-$, $^{12}\text{C}^{15}\text{N}^-$, $^{28}\text{Si}^-$, $^{29}\text{Si}^-$ and $^{30}\text{Si}^-$ were collected for the two KJG grains, whilst images of $^{12}\text{C}_2^-$, $^{12}\text{C}^{13}\text{C}^-$, $^{12}\text{C}^{14}\text{N}^-$, $^{12}\text{C}^{15}\text{N}^-$, $^{28}\text{Si}^-$, $^{29}\text{Si}^-$ and $^{30}\text{Si}^-$ were collected for the JA-MM2 grains (see Figure 6.2). Over the course of this work, the detector setup was altered to analyse molecular C isotopes instead of atomic C isotopes due to the increased yield of $^{12}\text{C}^{13}\text{C}^-$ ions compared to $^{13}\text{C}^-$ ions (L. Nittler, 2016, pers. comm.), resulting in higher counting statistics. Each ion image was 128×128 pixels, and comprised of 10 frames.

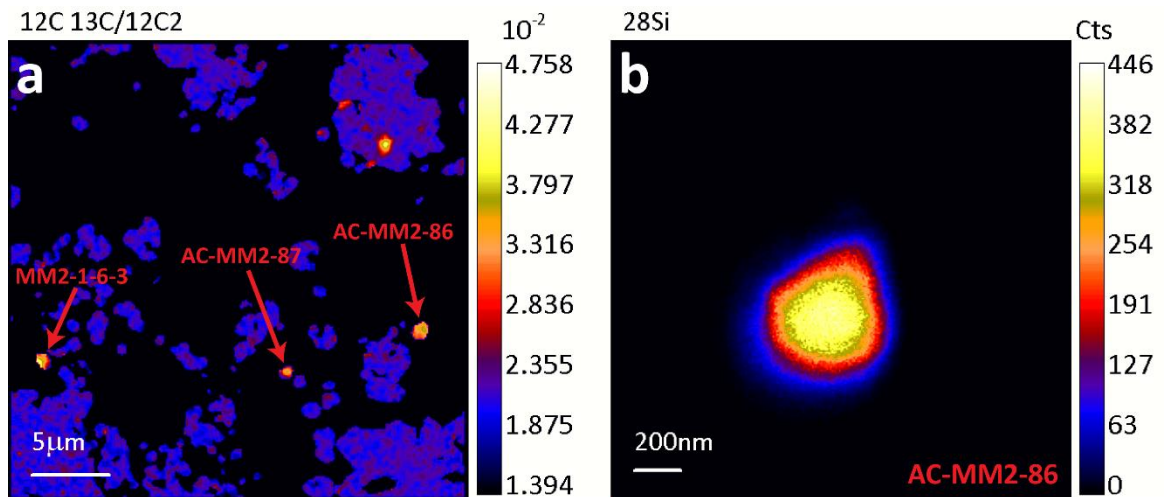


Figure 6.2: a) $^{12}\text{C}^{13}\text{C}^-/^{12}\text{C}_2^-$ isotope ratio image of a $30 \times 30\ \mu\text{m}$ field from which 3 presolar SiC grains (labelled) were identified. b) $^{28}\text{Si}^-$ secondary ion image of SiC grain AC-MM2-86, analysed with high spatial resolution with a $2\ \mu\text{m}$ field-of-view.

6.2.3 TOF-SIMS

Presolar SiC grains which were potentially isolated from nearby grains of different composition, and identifiable in the TOF-SIMS were selected for TOF-SIMS analysis. Analytical areas were between 3 and 20 μm , and each measurement collected between 700 and 1000 scans, each 64x64 pixels, with 64 primary ion shots per pixel. Each scan is saved individually, with a full mass spectrum recorded for each pixel.

Secondary ions were sputtered from the sample, with positive ions extracted by a +2000 V electric potential. In order to maximise the mass resolution at the lower end of the mass spectrum, the analyses were run in a 'delayed extraction' setup (see Section 3.3.2.2, this thesis), whereby the electric potential was applied after the primary ion beam had hit the sample. Delayed extraction helps to compensate for the time distribution of secondary ions, allowing for longer pulse lengths to be used ($\sim 30\text{-}40$ ns), which increases the counting statistics. Following extraction the secondary ions were analysed by the time-of-flight mass spectrometer, which utilises a two-stage reflectron to compensate for the energy spread of secondary ions of the same species. Higher energy ions penetrate further into the electric field, increasing the length of their flight path, allowing them to arrive at the detector at the same time as lower energy ions.

In order to determine depth profiles in a reasonable time frame, each grain was sputtered between measurements to remove material. Prior to beginning each measurement, a ~ 1 nA DC Au^+ beam was rastered over a 50×50 μm field over each grain for 5 minutes, in order to sputter ~ 50 nm of material.

A series of standards was analysed under the same measurement conditions in order to determine the effects of mass fractionation, and differences in the ionisation efficiency of different elements. As the chemical composition of a sample affects the ionisation efficiency of an element (and therefore, the measured elemental abundances), the standards must be similar in composition to the SiC grains. Only one SiC standard, NIST SRM 112b, could be procured for this work, so eight silicate standards were also analysed: NIST SRM 610/611 (both of the same composition- 610 is crushed into micron-sized grains, whilst 611 is a polished section), GOR128-G, GOR132-G, T1-G, KL2-G, ML3-B, ATHO-G, and StHs6/80-G (Jochum et al., 2000; Jochum et al., 2006; Jochum et al., 2011).

Delayed extraction also causes mass fractionation to occur during an analysis. As lighter ions (and elements) have higher velocities, they travel further from the sample compared to heavier ions. When the accelerating potential is turned on, some of these ions may have moved away from the extraction cone, leading to proportionally fewer of them being detected compared to heavier ions. As each of the silicate and SiC standards is terrestrial, they have known isotope ratios, meaning any mass fractionation can be calibrated.

6.2.4 Data Analysis

Data from the NanoSIMS analyses were analysed using the L'Image software (Larry Nittler, Carnegie Institution of Washington). Drift corrections were applied to the individual frames of each measurement, in order to correct for any beam or stage movement. By combining ion images (for example, those of ^{12}C and ^{13}C), isotope ratio images (such as $^{12}\text{C}/^{13}\text{C}$) were produced. Regions of Interest (ROIs) were drawn over each grain, so as to exclude any background counts from the gold foil.

Terrestrial silicon carbide grains were also analysed, in order for instrumental mass fractionation effects to be determined. The measured isotope ratios of each grain were corrected for these effects.

TOF-SIMS data were saved in the form of complete mass spectra at each pixel of the analysed region (xyt format). Regions of Interest (ROIs) were selected for each grain and its surrounding background. The mass spectra from each ROI were analysed using TSTSpec (Thomas Stephan, University of Chicago) (Stephan, 2001). A mass calibration was applied to each spectra by identifying three or more known peaks, and a statistical dead time correction was applied (Stephan et al., 1994), which accounts for simultaneous arrivals of secondary ions at the detector. Peaks (and the surrounding background) were selected across each mass spectrum, allowing element and isotope ratios to be determined.

The elemental abundances were corrected for both the background, and variations in ionisation efficiency of each element. Background abundances were determined from the ROIs selected around each grain, whilst the RSFs (determined from the silicate and SiC standards) were applied to correct for the ionisation efficiencies. The background

correction assumes that levels are constant across the analysed area. The measured isotope ratios were corrected for instrumental mass fractionation by applying the corrections determined from the silicate and SiC standards.

6.3 Results

6.3.1 Carbon, Silicon and Nitrogen Isotopes

The measured carbon, silicon and nitrogen isotope ratios for each grain are presented in Table 6.1. Seven of the grains are mainstream grains (see Figures 6.3 and 6.4), whilst one AB grain (AC-MM2-82) and two X grains, AC-MM2-41 (see Figure 6.5) and MM2-1-6-3, were also identified.

Grain	Type	$^{12}\text{C}/^{13}\text{C}$	$^{14}\text{N}/^{15}\text{N}$	$\delta^{29}\text{Si}$	$\delta^{30}\text{Si}$
AC-MM2-1	M	60.3 ± 0.1	428 ± 5	149 ± 1	95.8 ± 1.2
AC-MM2-41	X	523 ± 2	40.7 ± 0.3	-261 ± 1	-383 ± 1
AC-MM2-82	AB	8.41 ± 0.02	196 ± 259	51.9 ± 5.1	46.6 ± 6.3
AC-MM2-86	M	53.4 ± 0.5	597 ± 255	102 ± 7	104 ± 8
AC-MM2-87	M	49.0 ± 0.7	1592 ± 262	48.0 ± 11.8	76.4 ± 14.7
MM2-1-6-3	X	60.1 ± 1.6	233 ± 246	-425 ± 28	-286 ± 38
MM2-1-7	M	56.1 ± 1.7	225 ± 234	-194 ± 107	-112 ± 137
MM2-3-19	M	78.0 ± 3.8	297 ± 225	15.9 ± 66.8	37.1 ± 82.4
AC-KJG-2	M	45.6 ± 0.2	6499 ± 365	-37.8 ± 1.9	-37.6 ± 2.3
AC-KJG-3	M	57.9 ± 0.2	3488 ± 142	23.5 ± 1.2	18.9 ± 1.4

Table 6.1: Carbon, nitrogen and silicon isotope ratios of 10 presolar silicon carbide grains, as determined by NanoSIMS analysis. Errors are 1σ .

We were unable to determine the $^{12}\text{C}/^{13}\text{C}$, $^{14}\text{N}/^{15}\text{N}$ and $\delta^{29,30}\text{Si}$ isotope ratios from the TOF-SIMS analyses due to both low counting statistics (as a result of the pulsed primary ion beam), and insufficient mass resolution, particularly for the C and N isotopes.

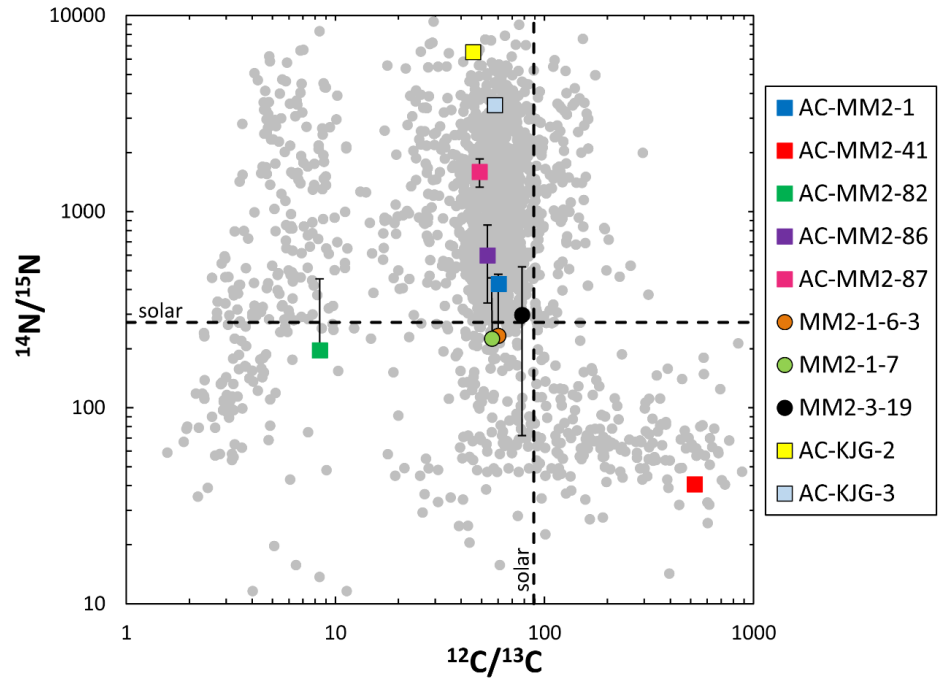


Figure 6.3: Carbon and nitrogen isotope ratios, as determined by NanoSIMS analysis, of the ten presolar SiC grains which were later analysed using the TOF-SIMS. Square symbols indicate the ratio was determined at high spatial resolution with a small field-of-view. Errors are 1σ . Grey points are literature data from the Presolar Grain Database (Hynes and Gyngard, 2009).

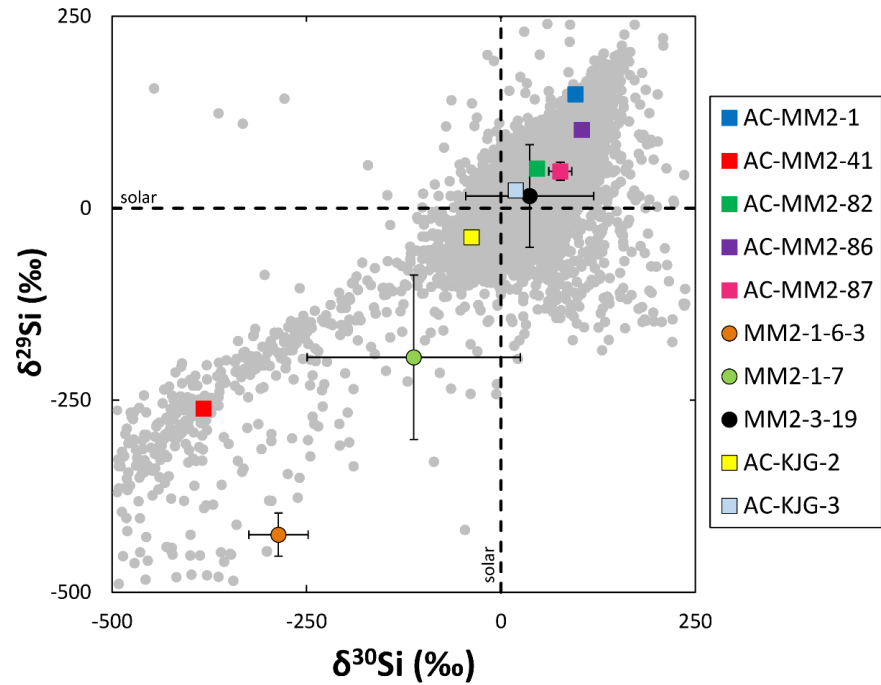


Figure 6.4: Silicon isotope ratios, as determined by NanoSIMS analysis, of the ten presolar SiC grains which were later analysed using the TOF-SIMS. Square symbols indicate the ratios were determined at high spatial resolution with a small field-of-view. Errors are 1σ . Grey points are literature data from the Presolar Grain Database (Hynes and Gyngard, 2009).

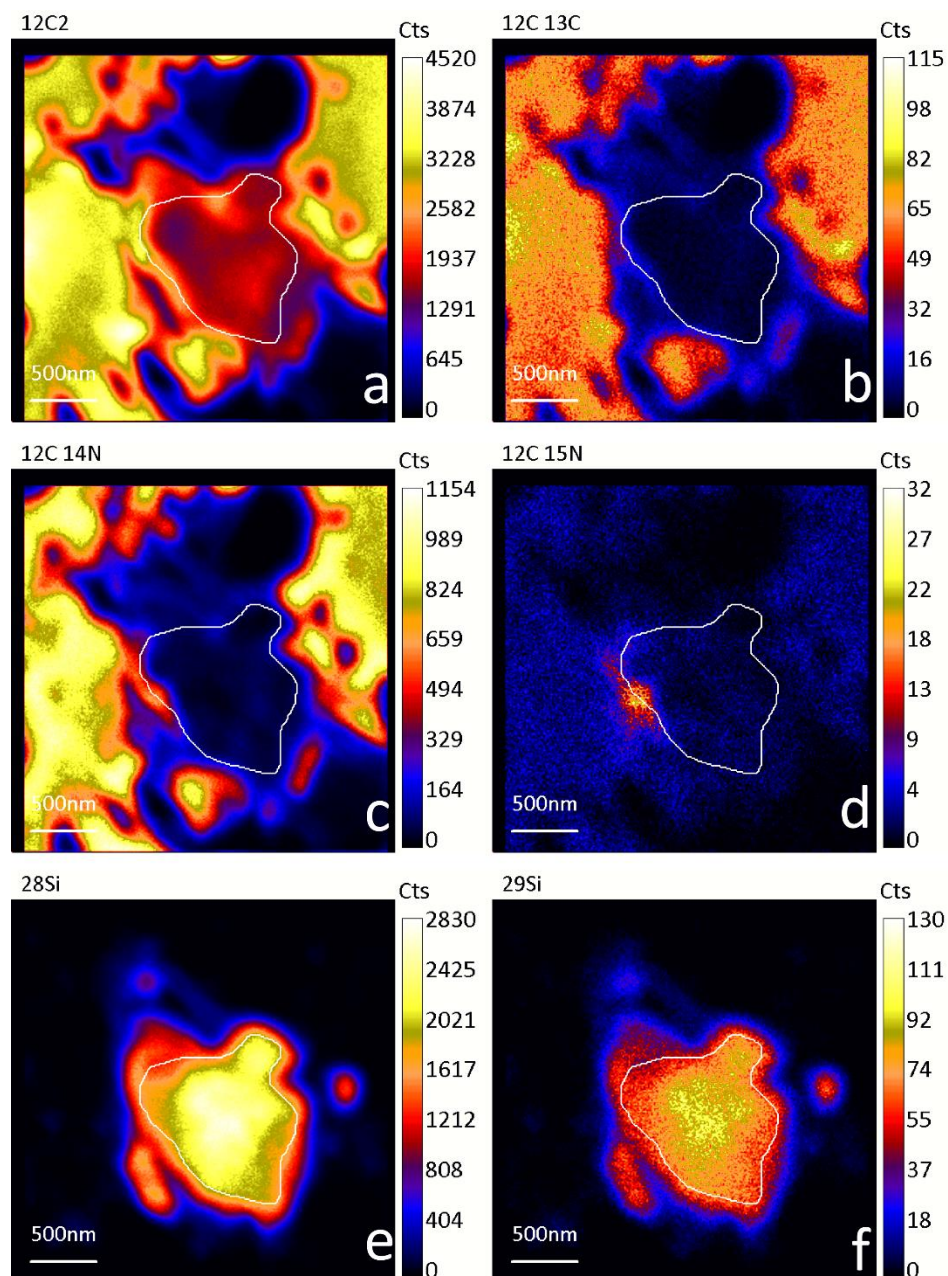


Figure 6.5: Secondary ion images of a) $^{12}\text{C}_2^-$, b) $^{12}\text{C}^{13}\text{C}^-$, c) $^{12}\text{C}^{14}\text{N}^-$, d) $^{12}\text{C}^{15}\text{N}^-$, e) $^{28}\text{Si}^-$, and f) $^{29}\text{Si}^-$ of grain AC-KJG-41, produced during NanoSIMS analysis. The white line indicates the outline of the grain.

6.3.2 Element Depth Profiles

6.3.2.1 JA-MM2 grains

Each of the eight presolar SiC grains from the JA-MM2 residue were measured for their trace element compositions, with repeated measurements acquired for AC-MM1 and AC-MM-41 to enable depth-profiles to be determined. Several secondary ion species were identified in each grain, with ion images produced for each. Examples of these from MM2-3-19 (Figure 6.6) and AC-MM2-1 (Figure 6.7) are shown presented here, whilst further images can be found in the Appendix of this thesis.

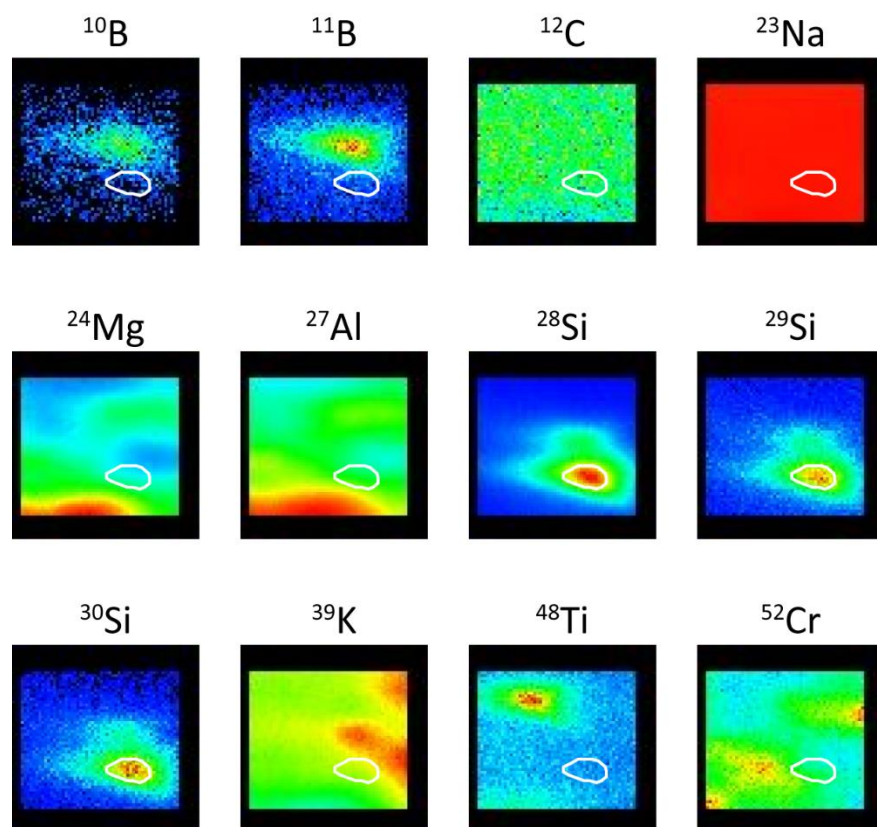


Figure 6.6: Ion images of selected secondary ion species from grain MM2-3-19 (outlined in white), as determined by TOF-SIMS analysis and corrected for instrumental drift using TOFCmd. Images are 6.5x6.5 μm .

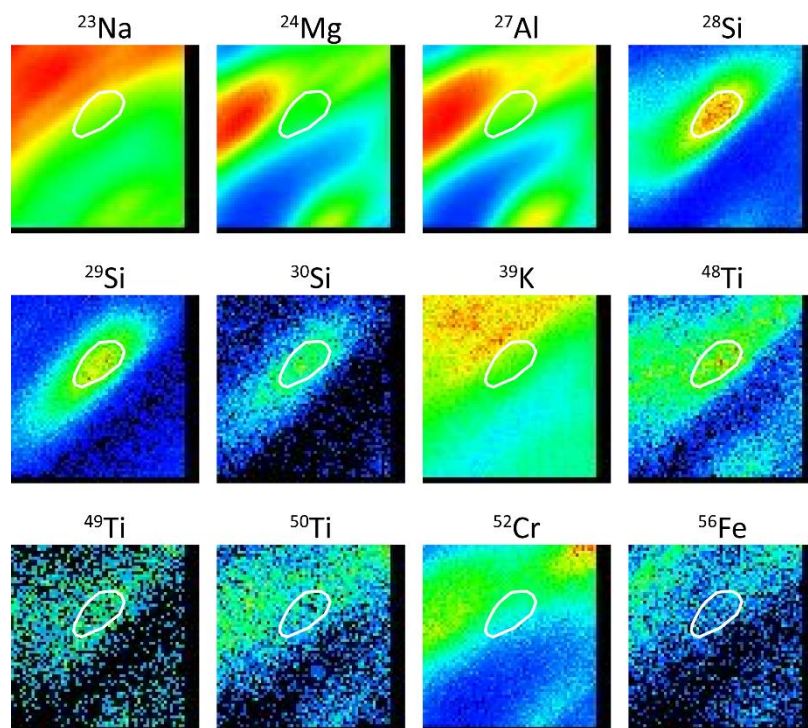


Figure 6.7: Ion images of selected secondary ion species from grain AC-MM2-1 (outlined in white), as determined by TOF-SIMS analysis and corrected for instrumental drift with TOFCmd. Images are 15x15 μm .

Although the peaks of many elements could be identified from the mass spectra of each grain, many of these were found to have elemental abundances which were almost indistinguishable from the surrounding background. Additionally, many of the SiC grains were surrounded by several other grains (see Figures 6.6 and 6.7), which prevented accurate background levels to be determined.

Six of the grains from JA-MM2, AC-MM-82, AC-MM2-86, AC-MM2-87, MM2-1-6-3, MM2-1-7 and MM2-3-19, had particularly high levels of background counts for many elements. As a result, the only elements which could reliably be determined to present in the grains were Na and K.

The analyses of AC-MM2-1 and AC-MM2-41 were also affected by high background counts due to the proximity of nearby grains. Several measurements of AC-MM2-1 suggested the presence of Ti, V, Cr, Fe, Sr and Ba (see Figure 6.7), with possible B, K and Ca, although the presence of these elements varied between measurements. Meanwhile, grain AC-MM2-41 appears to contain above-background levels of Na and Ti, with possible Al, K, Cr, Fe and Ba, although again, the presence of these elements varied between measurements.

6.3.2.2 KJG grains

Depth profiles for several elements were produced for the two presolar SiC grains from the JA-MM2 residue. During the NanoSIMS analyses, a significant volume of material was sputtered from each of these grains (see Figure 6.8).

Thirteen TOF-SIMS analyses were acquired for AC-KJG-2 before the grain was completely sputtered away. As ~50 nm of material was sputtered between each measurement, a total of ~650 nm of the grain was depth-profiled. Assuming that grain AC-KJG-2 was approximately spherical, with a pre-analysis diameter of ~1.25 μm , it can be estimated that the depth profile begins at a depth of ~600 nm.

A total of 14 TOF-SIMS analyses were carried out for AC-KJG-3, equating to a depth profile of ~700 nm. Assuming the grain was approximately spherical, with a pre-analysis diameter of ~1.5 μm , the trace element depth profiles begin from a depth of ~800 nm.

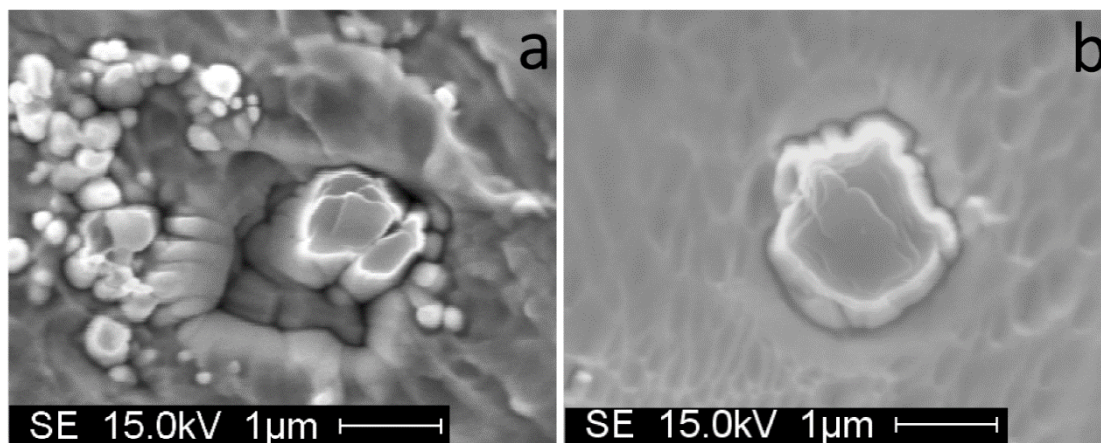


Figure 6.8: Secondary Electron (SE) images of a) AC-KJG-2, and b) AC-KJG-3, after analysis with the NanoSIMS. Images were collected using a FEI XL30 ESEM.

Elemental abundances of Na, Mg, K, Ti, Cr, Mn, Fe and Sr were determined for grain AC-KJG-2, and are displayed in Table 6.2. The depth profiles for many of these elements are reasonably flat (see Figure 6.9), with approximately uniform elemental abundances throughout the grain. Some variation is evident in the abundance of Sr through the grain, although the mass resolution at high masses is often unable to completely resolve isotopes from their isobaric interferences.

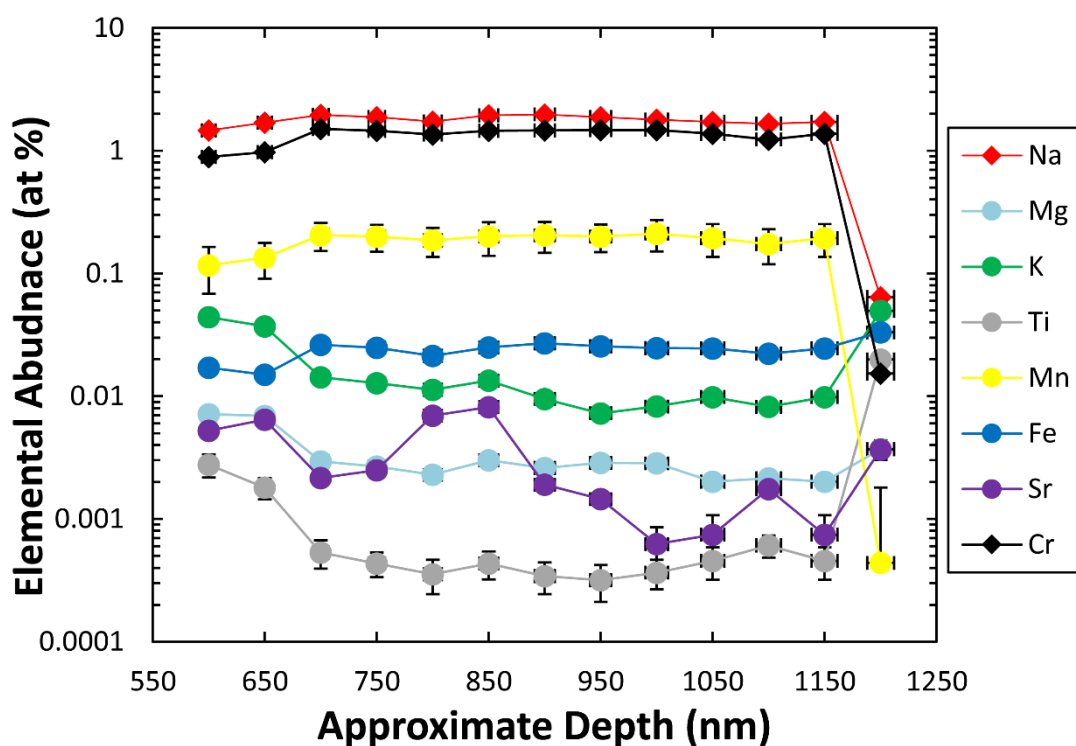


Figure 6.9: Trace element depth profiles of Na, Mg, K, Ti, Cr, Mn, Fe and Sr for grain AC-KJG-2, as determined by TOF-SIMS analysis. Elemental abundances are relative to Si.

Errors are 1σ .

Approximate Depth (nm)	Na/Si	Mg/Si ($\times 10^{-3}$)	K/Si ($\times 10^{-2}$)	Ti/Si ($\times 10^{-4}$)	Cr/Si	Mn/Si ($\times 10^{-1}$)	Fe/Si ($\times 10^{-2}$)	Sr/Si ($\times 10^{-3}$)
600	1.46 \pm 0.04	7.17 \pm 0.67	4.41 \pm 0.22	27.8 \pm 6.0	0.889 \pm 0.048	1.16 \pm 0.08	1.71 \pm 0.21	5.24 \pm 0.44
650	1.69 \pm 0.04	6.90 \pm 0.32	3.70 \pm 0.15	18.0 \pm 3.6	0.972 \pm 0.044	1.34 \pm 0.07	1.50 \pm 0.10	6.44 \pm 0.41
700	1.96 \pm 0.07	2.94 \pm 0.21	1.43 \pm 0.06	5.33 \pm 1.38	1.50 \pm 0.05	2.05 \pm 0.08	2.63 \pm 0.13	2.15 \pm 0.13
750	1.88 \pm 0.06	2.68 \pm 0.17	1.28 \pm 0.05	4.33 \pm 0.99	1.45 \pm 0.05	1.99 \pm 0.07	2.48 \pm 0.13	2.49 \pm 0.14
800	1.73 \pm 0.06	2.29 \pm 0.21	1.13 \pm 0.04	3.55 \pm 1.10	1.35 \pm 0.05	1.86 \pm 0.07	2.13 \pm 0.13	6.96 \pm 0.26
850	1.94 \pm 0.08	3.01 \pm 0.21	1.34 \pm 0.06	4.34 \pm 1.13	1.45 \pm 0.06	2.00 \pm 0.09	2.50 \pm 0.13	8.15 \pm 0.27
900	1.98 \pm 0.07	2.60 \pm 0.16	0.951 \pm 0.031	3.42 \pm 0.99	1.46 \pm 0.06	2.04 \pm 0.08	2.69 \pm 0.14	1.90 \pm 0.09
950	1.88 \pm 0.06	2.86 \pm 0.20	0.726 \pm 0.024	3.17 \pm 1.06	1.47 \pm 0.05	2.00 \pm 0.07	2.55 \pm 0.14	1.45 \pm 0.09
1000	1.79 \pm 0.07	2.84 \pm 0.26	0.824 \pm 0.038	3.66 \pm 0.99	1.48 \pm 0.06	2.11 \pm 0.09	2.46 \pm 0.16	0.624 \pm 0.227
1050	1.72 \pm 0.06	2.01 \pm 0.22	0.985 \pm 0.044	4.54 \pm 1.34	1.37 \pm 0.06	1.94 \pm 0.09	2.45 \pm 0.15	0.745 \pm 0.325
1100	1.66 \pm 0.05	2.15 \pm 0.17	0.819 \pm 0.032	6.09 \pm 1.26	1.23 \pm 0.05	1.73 \pm 0.08	2.22 \pm 0.15	1.75 \pm 0.11
1150	1.72 \pm 0.06	2.01 \pm 0.22	0.985 \pm 0.044	4.54 \pm 1.34	1.37 \pm 0.06	1.94 \pm 0.09	2.45 \pm 0.15	0.745 \pm 0.325
1200	0.064 \pm 0.002	3.71 \pm 0.67	4.96 \pm 0.22	199 \pm 15	0.0153 \pm 0.0014	0.00439 \pm 0.00299	3.31 \pm 0.30	3.69 \pm 0.33
Geometric Mean	1.38 \pm 0.05	3.03 \pm 0.25	1.43 \pm 0.06	7.33 \pm 1.74	0.935 \pm 0.040	1.15 \pm 0.06	2.35 \pm 0.15	2.34 \pm 0.21

Table 6.2: Elemental abundances of Na, Mg, K, Ti, Cr, Mn, Fe and Sr for grain AC-KJG-2, as determined by TOF-SIMS. Abundances (relative to Si) are quoted for the entire depth profile, as well as a geometric mean for the whole grain. Errors are 1σ .

Elemental abundances of Li, O, Na, Mg, Al and Ca were determined for grain AC-KJG-3, and are presented in Table 6.3. As with grain AC-KJG-2, the depth profiles are flat, with approximately homogeneous abundances throughout the grain (see Figure 6.10).

Approximate Depth (nm)	Li/Si ($\times 10^{-6}$)	O/Si	Na/Si ($\times 10^{-1}$)	Mg/Si ($\times 10^{-2}$)	Al/Si ($\times 10^{-3}$)	Ca/Si ($\times 10^{-2}$)
800	3.10 ± 1.14	0.284 ± 0.079	0.607 ± 0.215	1.13 ± 0.14	3.14 ± 0.49	1.77 ± 0.56
850	4.41 ± 1.58	0.297 ± 0.082	0.906 ± 0.321	1.21 ± 0.15	3.18 ± 0.50	2.27 ± 0.71
900	4.81 ± 1.82	0.287 ± 0.081	1.19 ± 0.42	1.49 ± 0.18	3.82 ± 0.60	2.71 ± 0.85
950	5.06 ± 1.92	0.260 ± 0.074	0.991 ± 0.351	1.18 ± 0.15	3.08 ± 0.49	2.36 ± 0.74
1000	5.77 ± 2.15	0.298 ± 0.085	1.25 ± 0.44	1.46 ± 0.18	3.41 ± 0.54	2.64 ± 0.83
1050	6.64 ± 2.35	0.267 ± 0.074	1.14 ± 0.40	1.23 ± 0.15	3.37 ± 0.53	2.51 ± 0.79
1100	6.99 ± 2.53	0.280 ± 0.079	1.34 ± 0.48	1.50 ± 0.18	3.76 ± 0.59	2.78 ± 0.87
1150	8.90 ± 3.19	0.307 ± 0.086	1.27 ± 0.45	1.46 ± 0.18	3.75 ± 0.59	2.76 ± 0.86
1200	8.45 ± 3.01	0.270 ± 0.076	1.25 ± 0.44	1.45 ± 0.18	3.73 ± 0.58	2.65 ± 0.83
1250	8.29 ± 2.95	0.295 ± 0.083	1.28 ± 0.45	1.42 ± 0.17	3.60 ± 0.56	2.61 ± 0.82
1300	6.68 ± 2.41	0.274 ± 0.077	1.11 ± 0.39	1.17 ± 0.15	3.07 ± 0.49	2.35 ± 0.74
1350	8.44 ± 2.99	0.289 ± 0.081	1.28 ± 0.45	1.49 ± 0.18	3.19 ± 0.50	2.70 ± 0.85
1400	7.34 ± 2.64	0.268 ± 0.075	1.11 ± 0.39	1.17 ± 0.14	3.12 ± 0.49	2.32 ± 0.73
1450	6.09 ± 2.25	0.237 ± 0.068	1.05 ± 0.37	1.12 ± 0.14	3.07 ± 0.48	2.16 ± 0.68
Geometric Mean	6.25 ± 2.27	0.279 ± 0.078	1.11 ± 0.39	1.31 ± 0.16	3.37 ± 0.53	2.45 ± 0.77

Table 6.3: Elemental abundances of Li, O, Na, Mg, Al and Ca in grain AC-KJG-3, as determined by TOF-SIMS. Abundances (relative to Si) are quoted for the entire depth profile, along with a geometric mean of the entire grain. Errors are 1σ .

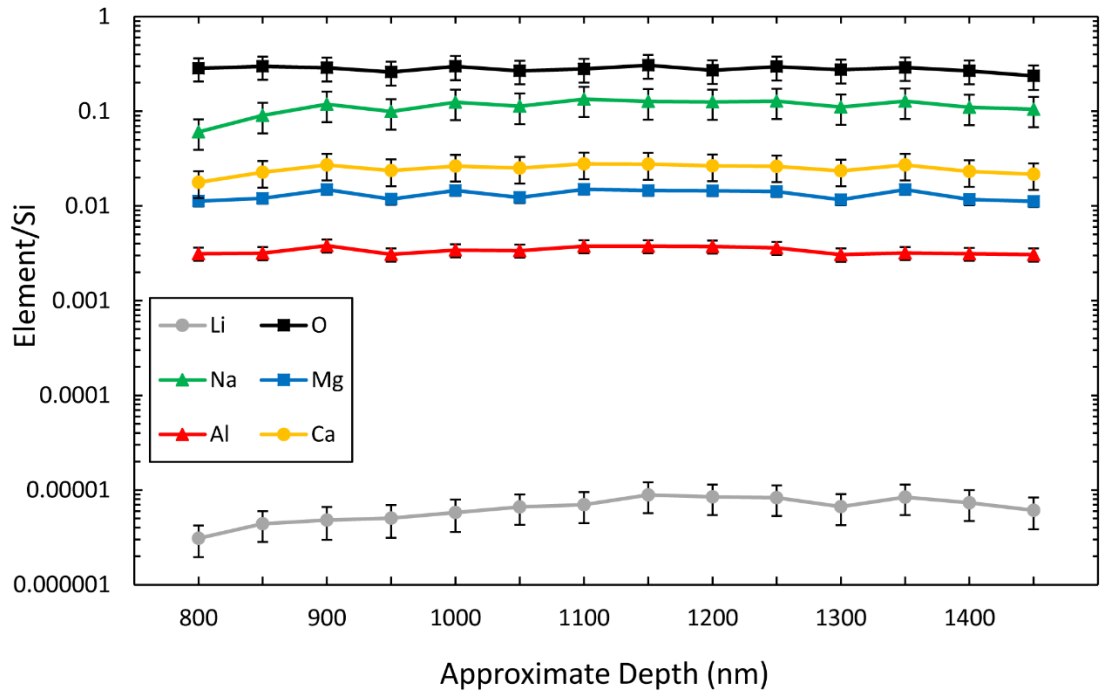


Figure 6.10: Trace element depth profiles of Li, O, Na, Mg, Al and Ca in grain AC-KJG-3, as determined by TOF-SIMS. Elemental abundances are relative to Si, and all errors are 1σ .

6.4 Discussion

6.4.1 Carbon, Silicon and Nitrogen Isotopes

The measured C, N and Si isotope ratios using the NanoSIMS suggest that seven of the grains- AC-KJG-2, AC-KJG-3, AC-MM2-1, AC-MM2-86, AC-MM2-87, MM2-1-7 and MM2-3-19- are mainstream presolar SiC grains. Mainstream grains make up ~90% of all presolar SiC, and are suggested to have formed around 1-3 M_{\odot} AGB (asymptotic giant branch) stars of solar metallicity (Iben and Renzini, 1983; Zinner et al., 1989; Hoppe et al., 1994; Hoppe and Ott, 1997; Nicolussi et al., 1997; Nicolussi et al., 1998; Lugaro et al., 2003).

One grain, AC-MM2-82, was identified as an AB grain. The astrophysical environment in which these grains form is less well understood, although it has been suggested that they may form around post-AGB stars, J-type stars, or in core-collapse supernovae (Lambert et al., 1986; Amari et al., 1995; Asplund et al., 1998; Pellin et al., 2000; Herwig, 2001; Savina et al., 2003; Herwig et al., 2011; Pignatari et al., 2015; Nguyen et al., 2018). Two grains, AC-MM2-41 and MM2-1-6-3 were identified as X grains, on the basis of their extremely low $\delta^{29}\text{Si}$ and $\delta^{30}\text{Si}$ compositions, and low $^{14}\text{N}/^{15}\text{N}$ for AC-MM2-1. X grains are believed to form in the ejecta of Type II supernovae (Meyer and Clayton, 2000; Rauscher et al., 2002; Pignatari et al., 2013a).

The isotope ratios of C, N and Si could not be determined by TOF-SIMS analysis. The use of a pulsed primary ion beam, necessary for the time-of-flight technique, results in low counting statistics. Additionally, the mass resolution was not high enough to fully resolve the peaks of many neighbouring peaks (such as $^{29}\text{Si}^+$ and $^{28}\text{SiH}^+$), meaning any calculated isotope ratios are highly unreliable.

6.4.2.2 KJG Grains

Both AC-KJG-2 and AC-KJG-3 display flat depth profiles for each measured element, with approximately uniform abundances throughout each grain. The abundances of many of the elements are in agreement with those measured in previous studies (Amari et al., 1995; Henkel et al., 2007a; King et al., 2012).

The measured abundances of oxygen for AC-KJG-3 is higher than would be expected for SiC grains, with reported abundances of 0.28 relative to Si. Rather than being a true

abundance, it is likely that the enrichment of oxygen is due to a poorly defined RSF value, which is used to correct for variations in ionisation efficiency between different elements.

The RSF values were determined by analysing a series of silicate and SiC standards. Oxygen does not readily produce a positive secondary ion, instead being predominantly sputtered as negative secondary ions. The result is that even in O-rich samples, such as the silicate standards, low count rates of O are detected, leading to the RSF being poorly defined. Additionally, oxygen's ionisation behaviour in SiC is unknown, as it was not detectable in the TOF-SIMS analyses of the SiC standard.

The measured abundances of Cr in AC-KJG-2 are around 2 orders of magnitude higher than those determined by King et al. (2012). The lack of variation in the depth profile suggests that the elevated abundances are not attributable to a Cr-rich sub-grain. The enrichment in Cr may reflect that of the stellar envelope at the time of condensation, or subsequent alteration. As uniform abundances are seen throughout the grain, it is unlikely that terrestrial contamination caused the elevated abundances, as this would only be expected to affect the outer regions of the grain. The Chicago Procedure, used to produce the KJG residue, does utilise a Cr_2O_7 chemical treatment, although it would be unlikely for this to penetrate through the entire grain.

Previous work by Lyon et al. (2007) found elevated abundances of Li and B near the surface of SiC grains, likely caused by implantation of ions or atoms by shockwaves in the ISM. The measured abundances of Li in this work are several orders of magnitude lower for grain AC-KJG-3, showing homogeneous abundances throughout the grain, with no evidence for implantation of material. However, both grains were extracted using the 'Chicago Procedure' (Amari et al., 1994), which has been demonstrated to alter the surface of SiC grains (Stephan et al., 1997; Henkel et al., 2007a). Therefore it is possible that evidence for ion or atom implantation may have been destroyed or altered.

The homogeneous distributions of trace elements may reflect either the composition of the stellar envelope in which the grains condensed, or could suggest the grain was homogenised by alteration processes. Assuming the distribution reflects primary processes, it suggests that the composition of the stellar envelope was relatively constant as the grains were condensing, with little variation. Alternatively, it is possible that the

grains were homogenised by secondary alteration processes. Grains may be affected by thermal or aqueous alteration in their parent asteroids, or become vaporised by shockwaves in the ISM, before re-condensing with homogeneous compositions.

6.5 Conclusions

Ten presolar silicon carbide grains were analysed for their major and trace element compositions, using a combination of NanoSIMS and TOF-SIMS analyses. Seven of these grains were determined to be mainstream grains, whilst one AB and two X grains were also identified.

The six SiC grains from the JA-MM2 residue were analysed with the highest spatial resolution that is currently achievable on the IDLE-3 TOF-SIMS, but this proved to be insufficient for resolving the grains from other grains in the vicinity. Despite this, each of the grains was found to have slightly elevated abundances of Na and K compared to the background levels, in agreement with previous analyses of SiC grains.

The two SiC grains from the KJG residue were depth-profiled, with repeated TOF-SIMS measurements collected to sample over 500 nm of each grain. Each of these grains was found to be homogeneous, with uniform trace element abundances throughout the grain. Around 40% of the SiC grains analysed by King et al. (2012) had homogeneous element distributions. The uniform abundances may reflect the composition of the stellar envelope in which the grains formed, although it cannot be ruled out that the grains were homogenised by secondary alteration processes. Neither grain showed evidence of Li implantation in the grain surface as has previously been identified by Lyon et al. (2007). However, it is possible that evidence of ion or atom implantation may have been altered or removed during the extraction process (Stephan et al., 1997; Henkel et al., 2007a).

Chapter 7

Summary and Future Work

This chapter summarises the research covered in this thesis, examines the analytical problems encountered, and suggests future research opportunities.

7.1 Issues with ‘Gentle Separation’

The original aim of this work was to compare the effects of sample preparation on presolar SiC, by analysing presolar SiC grains separated from their host meteorites by physical means (size and density separation) (Tizard et al., 2005), with SiC grains measured *in-situ* in meteorite matrix and from acid residues. The objective of this work was to assess to what degree the widely used acid residue technique induced chemical and isotopic alteration in the grains.

Unfortunately, due to issues with the density separation procedure, no gently separated grains were identified during this work. During the density separation step, the grains repeatedly clumped to form small aggregates. As the aggregates trapped air between them, they floated on the surface of the Organic Heavy Liquids, and prevented the grains from being separated according to their density. It was initially assumed that the grains had ‘dried out’ and stuck together, although the same issues were encountered when the process was repeated with ‘wet’ grains.

The gentle separation method was repeated twice, with chips of Murchison and GRA 95229. As the grains continued to clump together, a decision was taken to abandon the density separation, and search for grains in the size separated fractions. As the abundance of presolar SiC grains was lower in these fractions, the searches were time-consuming. After several weeks of analytical time without success, the search for gently separated SiC grains was abandoned due to time constraints with the project, and the focus was moved onto the acid residue and *in-situ* grains.

7.2 Comparison of Acid Residue and *In-Situ* Grains

During this work, 185 presolar SiC grains were identified and analysed from three acid residues and two polished meteorite sections. The C, Si and N isotope ratios of each grain were determined, so as to identify each grain's SiC sub-group, and therefore its stellar origin.

Of the 185 grains analysed in this work, 168 were mainstream grains, which are suggested to have formed around 1-3 M_{\odot} AGB star of close to solar metallicity. Four X grains were identified, all from JA-MM2, and are thought to have condensed in the ejecta of a Type II supernova. Thirteen AB grains were also identified- two *in-situ* in Acfer 094, two each in the KJG and JA-MM residues, and seven from the JA-MM2 residue. The origin of these grains is not well understood, but has been argued that they may have formed around a post-AGB or J-type star.

SiC grains from the KJG residue were found to be highly depleted in ^{15}N , in agreement with data from other high spatial resolution analyses. However, grains from the other samples (Acfer 094, GRA 95229, JA-MM and JA-MM2) had on average, lower $^{14}\text{N}/^{15}\text{N}$ ratios, more in agreement with those found in the Presolar Grain Database. As the three acid residues were all produced from Murchison, it is unlikely that the KJG residue would contain a different population of SiC grains compared to JA-MM and JA-MM2, suggesting there may be some influence of terrestrial contamination, which would result in lower $^{14}\text{N}/^{15}\text{N}$ compositions. Modelling suggests 20-50% of terrestrial contamination for a typical KJG grain composition would be required to produce the typical $^{14}\text{N}/^{15}\text{N}$ composition of the JA-MM and JA-MM2 grains. Any contamination on the surface of the grains would be rapidly sputtered during a NanoSIMS analysis, revealing the 'true' isotopic composition as the acquisition progresses, suggesting that if any alteration in these grains must penetrate through the entire grain.

The majority of the *in-situ* grains from Acfer 094 and GRA 95229 were also found to have relatively low $^{14}\text{N}/^{15}\text{N}$ ratios compared to grains from the KJG residue. Although the measurements were carried out with high spatial resolution (typically 100-130 nm), the small size (typically 100-500 nm) of many of the *in-situ* grains means the measured ratios may have been affected by isotopic dilution from surrounding minerals, which have solar compositions. If isotopic dilution had affected the measured ratios, it would be expected

to find a correlation between the grain size and measured $^{14}\text{N}/^{15}\text{N}$ ratios of the grains. No correlation between $^{14}\text{N}/^{15}\text{N}$ and grain size was identified in this work, suggesting that the influence of isotopic dilution to the measured ratios was minimal. Whilst it is possible that both Acfer 094 and GRA 95229 could have been affected by contamination, models suggest that a relatively high proportion (40-50%) would be required to produce a $^{14}\text{N}/^{15}\text{N}$ ratio of ~ 700 , the average of the Acfer 094 grains. Additionally, as both of these samples were prepared as polished sections, any contamination would likely be found on the sample surface; during a NanoSIMS analysis, surface contamination would be rapidly sputtered away, revealing the true $^{14}\text{N}/^{15}\text{N}$ isotope ratio of the grain.

The majority of SiC grains analysed in this work were found to have silicon isotope ratios which lie on a slope similar to that defined by the literature on a Si 3-isotope plot. However, the grains from the JA-MM and JA-MM2 residues appear to lie on shallower slopes, although there is significant scatter for each of the samples, which appears to have affected the gradient of the calculated trendlines. Models suggest that the fractionation of the Si isotopes in these grains is not caused by contamination with terrestrial material. Additionally, no correlation was identified between the measured $\delta^{29,30}\text{Si}$ compositions and the grain sizes of the *in-situ* grains, suggesting that isotopic dilution has not affected the measured $\delta^{29,30}\text{Si}$ ratios.

The differences in the $^{12}\text{C}/^{13}\text{C}$, $^{14}\text{N}/^{15}\text{N}$ and $\delta^{29,30}\text{Si}$ compositions of the SiC grains from different samples does not appear to be adequately explained by either contamination with terrestrial material, or by isotopic dilution. In the absence of other suitable explanations, it is possible that these differences represent real variations in the SiC grain populations of different meteorites.

7.3 Effect of Sample Topography on Secondary Ion Extraction in the NanoSIMS

In this work, apparent heterogeneity in the distribution of N within the grain was discovered in many SiC grains from the acid residue samples, whilst the C and Si distributions were homogeneous. As heterogeneity can be used to inform on the processing history of presolar grains, it was important to determine whether the N distribution was real. As the heterogeneity was only seen in acid residue grains, it was

suggested that the topography of the grain may influence the extraction of secondary ions, potentially causing fractionation of atomic and molecular species.

Modelling the secondary ion flight paths in the NanoSIMS revealed that atomic ions are largely unaffected by the topography of a sample; their higher relative kinetic energy means that their trajectories through the NanoSIMS ion optics are relatively undisturbed by variations in the local electric field at the grain surface, arriving at the slits and apertures as a diffuse, homogeneous ion beam. As the beam is homogenised, each secondary ion loses its spatial coherence with its original location on the grain, forming homogeneous ion images at the slits and apertures inside the mass spectrometer.

In contrast, the trajectories of molecular secondary ions, which have lower kinetic energy on average than the atomic secondary ions, are strongly influenced by the sample topography. Their low kinetic energy means that they are greatly affected by the local field; secondary ions from different parts of the sample arrive at the slit as distinct, dispersed beams, effectively projecting an 'image' of the grain onto the slits and apertures. The enrichments of N at the edges of many of the acid residue presolar SiC grains are likely an artefact caused by the grain topography, rather than a true heterogeneous distribution.

The altered flight paths of atomic and molecular ions create the potential for fractionation to occur at the slits and apertures inside the NanoSIMS and that topography, even on a ~micron scale sample, can induce significant transmission and isotopic fractionation effects. Induced isotopic fractionation is shown to be small (<10%) provided the ion beams are aligned optimally within the instrument but have the potential to be greater (>100%) if the alignment is sub-optimal.

7.4 Trace Element Depth Profiles

Ten presolar SiC grains, 7 mainstream, 1 AB and 2 X grains, from the KJG and JA-MM2 acid residues were comprehensively analysed for their trace element compositions using TOF-SIMS, with repeated measurements collected for 4 of the grains to determine trace element depth-profiles.

The analyses of the 8 grains from the JA-MM2 residue were strongly affected by the presence of other nearby grains, which resulted in high background counts meaning few elements could reliably be determined to be present in the SiC grains. Each of these grains appear to contain Na and K, whilst two of the grains (AC-MM2-1 and AC-MM2-41) are suggested to contain Na and Ti, with possible V, Cr, Fe, Sr, Ba, Al and K.

The two grains from the KJG residue, AC-KJG-2 and AC-KJG-3, appear to contain significant abundances of O, Na, Cr, Mn, Fe and Sr, with possible Mg, Al, K, Ti and V. Due to analytical issues, the spatial resolution during the analyses of these two grains was poorer than would be ideal. However, the absence of any nearby grains meant that the background counts for many elements were low enough to allow several peaks to be identified from the mass spectra.

7.5 Future Work

7.5.1 Gently Separated SiC Grains

Although the separation procedure was unsuccessful in this project, the analysis of pristine gently separated grains is a key continuation of this work. High spatial resolution analyses of C, N and Si isotope ratios would allow direct comparison with the acid residue and *in-situ* grains from this work, as well as with other analyses from the Presolar Grain Database. Comparing grains from different sample preparation and analytical techniques is vital to understanding the spread of isotope ratios in the literature data, particularly for $^{14}\text{N}/^{15}\text{N}$. Determining any influence of contamination will allow improved constraints to be placed on astrophysical models which seek to understand stellar nucleosynthesis.

7.5.2 Acid Residue and *In-Situ* Grains

Although a significant number of presolar SiC grains were analysed in this work, we are currently unable to determine if the differences between grain populations from different samples represent real variation between different meteorites.

It would be beneficial to this work to analyse additional SiC grains, particularly from Acfer 094 and GRA 95229. Analysis of grains from additional meteorites, from a range of meteorite groups and petrologic types, would enable greater comparison between the SiC populations from different meteorites. This project could also be extended to include other presolar grain types, such as graphites and oxides.

7.5.3 Trace Element Depth Profiling

Trace element analysis of presolar SiC grains was relatively unsuccessful during this project, due to the influence of nearby grains on the measured elemental abundances. Further work should focus on preparing samples with lower grain densities, to maximise the separation of grains. Additionally, candidate grains should be extensively imaged using the SEM prior to analysis, in order to select grains with the clearest surroundings.

References

- Abia, C., De Laverny, P. and Wahlin, R. (2008). Chemical analysis of carbon stars in the Local Group-II. The Carina dwarf spheroidal galaxy. *Astronomy & Astrophysics* **481**:161-168.
- Alexander, C. M. O'D. (1993). Presolar SiC in chondrites: How variable and how many sources? *Geochimica et Cosmochimica Acta* **57**:2869-2888.
- Alexander, C. M. O'D. (1997) Dust production in the galaxy: the meteorite perspective, in: Bernatowicz, T., Zinner, E. (Eds.), AIP Conference Proceedings. AIP, pp. 567-593.
- Alexander, C. M. O'D. and Nittler, L. R. (1999). The galactic evolution of Si, Ti, and O isotopic ratios. *The Astrophysical Journal* **519**:222-235.
- Alpher, R. A., Bethe, H. and Gamow, G. (1948). The origin of chemical elements. *Physical Review* **73**:803-804.
- Amari, S., Anders, E., Virag, A. and Zinner, E. (1990). Interstellar graphite in meteorites. *Nature* **345**:238-240.
- Amari, S., Gao, X., Nittler, L. R., Zinner, E., Jose, J., Hernanz, M. and Lewis, R. S. (2001a). Presolar grains from novae. *The Astrophysical Journal* **551**:1065-1072.
- Amari, S., Hoppe, P., Zinner, E. and Lewis, R. S. (1992). Interstellar SiC with unusual isotopic compositions: Grains from a supernova? *The Astrophysical Journal* **394**:L43-L46.
- Amari, S., Hoppe, P., Zinner, E. and Lewis, R. S. (1995). Trace-element concentrations in single circumstellar silicon carbide grains from the Murchison meteorite. *Meteoritics* **30**:679-693.
- Amari, S., Lewis, R. S. and Anders, E. (1994). Interstellar grains in meteorites: I. Isolation of SiC, graphite and diamond; size distributions of SiC and graphite. *Geochimica et Cosmochimica Acta* **58**:459-470.
- Amari, S., Nittler, L. R., Zinner, E., Gallino, R., Lugaro, M. and Lewis, R. S. (2001b). Presolar SiC grains of type Y: Origin from low-metallicity asymptotic giant branch stars. *The Astrophysical Journal* **546**:248-266.
- Amari, S., Nittler, L. R., Zinner, E., Lodders, K. and Lewis, R. S. (2001c). Presolar SiC grains of type A and B: Their isotopic compositions and stellar origins. *The Astrophysical Journal* **559**:463-483.
- Amari, S., Zinner, E., Gallino, R., Lugaro, M., Straniero, O. and Dominguez, I. (2005) Probing the galactic chemical evolution of Si and Ti with presolar SiC grains, in: Terasawa, M., Kubono, S., Kishida, T., Kajino, T., Motobayashi, T., Nomoto, K. (Eds.), Origin of Matter & Evolution of Galaxies 2003. World Scientific, pp. 59-70.

- Anders, E. and Zinner, E. (1993). Interstellar grains in primitive meteorites: Diamond, silicon carbide, and graphite. *Meteoritics & Planetary Science* **28**:490-514.
- Arnould, M. (1976). Possibility of synthesis of proton-rich nuclei in highly evolved stars. II. *Astronomy & Astrophysics* **46**:117-125.
- Arnould, M. and Goriely, S. (2003). The p-process of stellar nucleosynthesis: astrophysics and nuclear physics status. *Physics Reports* **384**:1-84.
- Asplund, M., Lambert, D. L., Kipper, T., Pollacco, D. and Shetrone, M. (1998). The rapid evolution of the born-again giant Sakurai's object. *arXiv preprint astro-ph/9811208*.
- Audouze, J. (1970). Some nucleosynthetic effects of energetic proton fluxes on stellar surfaces and on the solar system. *Astronomy & Astrophysics* **8**:436-457.
- Bernatowicz, T., Fraundorf, G., Tang, M., Anders, E., Wopenka, B., Zinner, E. and Fraundorf, P. (1987). Evidence for interstellar SiC in the Murray carbonaceous meteorite. *Nature* **330**:728-730.
- Bernatowicz, T. J., Amari, S. and Lewis, R. S. (1992) TEM studies of a circumstellar rock, 23rd Lunar and Planetary Science Conference, p. Abstract #1045.
- Bernatowicz, T. J., Amari, S., Zinner, E. K. and Lewis, R. S. (1991). Interstellar grains within interstellar grains. *The Astrophysical Journal* **373**:L73-L76.
- Bernatowicz, T. J., Cowsik, R., Gibbons, P. C., Lodders, K., Fegley, B., Amari, S. and Lewis, R. S. (1996). Constraints on stellar grain formation from presolar graphite in the Murchison meteorite. *The Astrophysical Journal* **472**:760-782.
- Bernatowicz, T. J., Messenger, S., Pravdivtseva, O., Swan, P. and Walker, R. M. (2003). Pristine presolar silicon carbide. *Geochimica et Cosmochimica Acta* **67**:4679-4691.
- Bernheim, M., Wu, T. D., Guerquin-Kern, J. L. and Croisy, A. (2008). Focussing of a transient low energy Cs⁺ probe for improved NanoSIMS characterizations. *European Physical Journal-Applied Physics* **42**:311-319.
- Bertelli, G., Nasi, E., Girardi, L. and Marigo, P. (2009). Scaled solar tracks and isochrones in a large region of the Z–Y plane-II. From 2.5 to 20 M_⊙ stars. *Astronomy & Astrophysics* **508**:355-369.
- Besmehn, A. and Hoppe, P. (2003). A NanoSIMS study of Si-and Ca-Ti-isotopic compositions of presolar silicon carbide grains from supernovae. *Geochimica et Cosmochimica Acta* **67**:4693-4703.
- Black, D. C. and Pepin, R. O. (1969). Trapped neon in meteorites- II. *Earth and Planetary Science Letters* **6**:395-405.
- Boato, G. (1954). The isotopic composition of hydrogen and carbon in the carbonaceous chondrites. *Geochimica et Cosmochimica Acta* **6**:209-220.

- Bocchio, M., Jones, A. P. and Slavin, J. D. (2014). A re-evaluation of dust processing in supernova shock waves. *Astronomy & Astrophysics* **570**:A32.
- Boothroyd, A. I. and Sackmann, I.-J. (1999). The CNO isotopes: deep circulation in red giants and first and second dredge-up. *The Astrophysical Journal* **510**:232-250.
- Bose, M., Floss, C., Stadermann, F. J., Stroud, R. M. and Speck, A. K. (2012). Circumstellar and interstellar material in the CO3 chondrite ALHA77307: An isotopic and elemental investigation. *Geochimica et Cosmochimica Acta* **93**:77-101.
- Boss, A. P. (1995). Collapse and fragmentation of molecular cloud cores. 2: Collapse induced by stellar shock waves. *The Astrophysical Journal* **439**:224-236.
- Boss, A. P., Keiser, S. A., Ipatov, S. I., Myhill, E. A. and Vanhala, H. A. (2009). Triggering collapse of the presolar dense cloud core and injecting short-lived radioisotopes with a shock wave. I. Varied shock speeds. *The Astrophysical Journal* **708**:1268-1280.
- Burbidge, E. M., Burbidge, G. R., Fowler, W. A. and Hoyle, F. (1957). Synthesis of the elements in stars. *Reviews of modern physics* **29**:547-650.
- Busso, M., Gallino, R. and Wasserburg, G. J. (1999). Nucleosynthesis in asymptotic giant branch stars: Relevance for galactic enrichment and solar system formation. *Annual Review of Astronomy and Astrophysics* **37**:239-309.
- Cameron, A. G. W. (1957). Nuclear reactions in stars and nucleogenesis. *Publications of the Astronomical Society of the Pacific* **69**:201-222.
- Cameron, A. G. W. (1962). The formation of the sun and planets. *Icarus* **1**:13-69.
- Cameron, A. G. W. (1982) Elemental and nuclidic abundances in the solar system, Essays in Nuclear Astrophysics, pp. 23-44.
- Cameron, A. G. W. and Truran, J. W. (1977). The supernova trigger for formation of the solar system. *Icarus* **30**:447-461.
- Cassen, P. and Chick, K. M. (1997) The survival of presolar grains during the formation of the solar system, in: Bernatowicz, T., Zinner, E. (Eds.), AIP Conference Proceedings. AIP, pp. 697-719.
- Cerezo, A., Clifton, P. H., Galtrey, M. J., Humphreys, C. J., Kelly, T. F., Larson, D. J., Lozano-Perez, S., Marquis, E. A., Oliver, R. A. and Sha, G. (2007). Atom probe tomography today. *Materials Today* **10**:36-42.
- Choi, B.-G., Huss, G. R., Wasserburg, G. and Gallino, R. (1998). Presolar corundum and spinel in ordinary chondrites: Origins from AGB stars and a supernova. *Science* **282**:1284-1289.
- Clayton, D. D. (1988). Isotopic anomalies: Chemical memory of galactic evolution. *The Astrophysical Journal* **334**:191-195.

- Clayton, D. D. and Timmes, F. X. (1997). Placing the Sun in galactic chemical evolution: Mainstream SiC particles. *The Astrophysical Journal* **483**:220-227.
- Clayton, R. N., Grossman, L. and Mayeda, T. K. (1973). A component of primitive nuclear composition in carbonaceous meteorites. *Science* **182**:485-488.
- Cook, C. W., Fowler, W. A., Lauritsen, C. C. and Lauritsen, T. (1957). B 12, C 12, and the red giants. *Physical Review* **107**:508.
- Croat, T., Berg, T., Bernatowicz, T., Groopman, E. and Jadhav, M. (2013). Refractory metal nuggets within presolar graphite: First condensates from a circumstellar environment. *Meteoritics & Planetary Science* **48**:686-699.
- Croat, T., Jadhav, M., Lebsack, E. and Bernatowicz, T. (2011a). TiC and rutile within a supernova graphite. *Geochimica et Cosmochimica Acta* **69**:177-188.
- Croat, T., Jadhav, M., Lebsack, E. and Bernatowicz, T. (2011b) A unique supernova graphite: Contemporaneous condensation of all things carbonaceous, 42nd Lunar and Planetary Science Conference, p. Abstract #1533.
- Croat, T., Stadermann, F. and Bernatowicz, T. (2010). Unusual 29, 30Si-rich SiCs of massive star origin found within graphites from the Murchison meteorite. *The Astronomical Journal* **139**:2159.
- Croat, T. K., Bernatowicz, T., Amari, S., Messenger, S. and Stadermann, F. J. (2003). Structural, chemical, and isotopic microanalytical investigations of graphite from supernovae. *Geochimica et Cosmochimica Acta* **67**:4705-4725.
- Croat, T. K., Stadermann, F. J. and Bernatowicz, T. J. (2008). Correlated isotopic and microstructural studies of turbostratic presolar graphites from the Murchison meteorite. *Meteoritics & Planetary Science* **43**:1497-1516.
- Daulton, T. L., Bernatowicz, T. J., Lewis, R. S., Messenger, S., Stadermann, F. J. and Amari, S. (2002). Polytype distribution in circumstellar silicon carbide. *Science* **296**:1852-1855.
- Daulton, T. L., Bernatowicz, T. J., Lewis, R. S., Messenger, S., Stadermann, F. J. and Amari, S. (2003). Polytype distribution of circumstellar silicon carbide: Microstructural characterization by transmission electron microscopy. *Geochimica et Cosmochimica Acta* **67**:4743-4767.
- Daulton, T. L., Stadermann, F. J., Bernatowicz, T. J., Amari, S. and Lewis, R. S. (2009) Coordinated TEM/NanoSIMS Microanalysis of Structurally or Isotopically Rare Presolar Silicon Carbides, 72nd Annual Meeting of the Meteoritical Society. Lunar and Planetary Institute, Houston, p. Abstract #5381.
- Davidson, J., Busemann, H., Alexander, C., Nittler, L., Schrader, D., Orthous-Daunay, F.-R., Quirico, E., Franchi, I. and Grady, M. (2009) Presolar SiC abundances in primitive meteorites by NanoSIMS raster ion imaging of insoluble organic matter, 40th Lunar and Planetary Science Conference, p. Abstract #1853.

- Davis, A., Stephan, T., Trappitsch, R., Pellin, M., Savina, M. and Dauphas, N. (2015). CHILI, a Nanobeam Secondary Neutral Mass Spectrometer with Extraordinary Spatial Resolution, Sensitivity, and Selectivity: First Results. *Microscopy and Microanalysis* **21**:1143-1144.
- Ebisuzaki, T. and Shibasaki, N. (1988). The effects of mixing of the ejecta on the hard x-ray emissions from SN-1987A. *The Astrophysical Journal* **327**:L5-L8.
- Ehrenfreund, P. and Charnley, S. B. (2000). Organic molecules in the interstellar medium, comets, and meteorites: A voyage from dark clouds to the early earth. *Annual Review of Astronomy and Astrophysics* **38**:427-483.
- Floss, C. and Stadermann, F. J. (2009). High abundances of circumstellar and interstellar C-anomalous phases in the primitive CR3 chondrites QUE 99177 and MET 00426. *The Astrophysical Journal* **697**:1242-1255.
- Floss, C., Stadermann, F. J. and Bose, M. (2008). Circumstellar Fe oxide from the Acfer 094 carbonaceous chondrite. *The Astrophysical Journal* **672**:1266.
- Fowler, W. A. and Greenstein, J. L. (1956). Element-building reactions in stars. *Proceedings of the National Academy of Sciences* **42**:173-180.
- Gallino, R., Busso, M. and Lugaro, M. (1997) Neutron capture nucleosynthesis in AGB stars, in: Bernatowicz, T., Zinner, E. (Eds.), AIP Conference Proceedings. AIP, pp. 115-153.
- Gallino, R., Raiteri, C. M., Busso, M. and Matteucci, F. (1994). The puzzle of silicon, titanium, and magnesium anomalies in meteoritic silicon carbide grains. *The Astrophysical Journal* **430**:858-869.
- Groopman, E., Zinner, E., Amari, S., Gyngard, F., Hoppe, P., Jadhav, M., Lin, Y., Xu, Y., Marhas, K. and Nittler, L. R. (2015). Inferred Initial $^{26}\text{Al}/^{27}\text{Al}$ Ratios in Presolar Stardust Grains from Supernovae are Higher than Previously Estimated. *The Astrophysical Journal* **809**:31.
- Groopman, E. E. and Nittler, L. R. (2018). Correlated XANES, TEM, and NanoSIMS of presolar graphite grains. *Geochimica et Cosmochimica Acta* **221**:219-236.
- Gyngard, F., Amari, S., Jadhav, M., Marhas, K., Zinner, E. and Lewis, R. S. (2006). Titanium isotopic ratios in KJG presolar SiC grains from Murchison. *Meteoritics & Planetary Science* **41**:A71-A71.
- Haenecour, P., Floss, C., José, J., Amari, S., Lodders, K., Jadhav, M., Wang, A. and Gyngard, F. (2016). Coordinated Analysis of Two Graphite Grains from the CO3. 0 LAP 031117 Meteorite: First Identification of a CO Nova Graphite and a Presolar Iron Sulfide Subgrain. *The Astrophysical Journal* **825**:88.
- Hainebach, K., Schramm, D. and Blake, J. (1976). Cosmic-ray spallative origin of the rare odd-odd nuclei, consistent with light-element production. *The Astrophysical Journal* **205**:920-930.

- Harrison, T. (1978). The low-temperature photonuclear nucleosynthesis of the bypassed (p-) nuclei in degenerate hydrogen burning zones and its relationship to nova outbursts. *The Astrophysical Journal Supplement Series* **36**:199-216.
- Heck, P., Pellin, M., Davis, A., Isheim, D., Seidman, D., Hiller, J., Mane, A., Elam, J., Savina, M. and Auciello, O. (2011a) Atom-probe tomographic analyses of Allende and synthetic nanodiamonds, Workshop on Formation of the First Solids in the Solar System, p. 9096.
- Heck, P., Pellin, M., Davis, A., Isheim, D., Seidman, D., Hiller, J., Mane, A., Elam, J., Savina, M. and Auciello, O. (2012) Atom-Probe Tomographic Analysis: Towards Carbon Isotope Ratios in Individual Nanodiamonds, 43rd Lunar and Planetary Science Conference, p. Abstract #1790.
- Heck, P., Pellin, M., Davis, A., Isheim, D., Seidman, D., Hiller, J., Mane, A., Elam, J., Savina, M. and Stephan, T. (2011b) Atom-probe tomographic analyses of meteoritic nanodiamond residue from Allende, 42nd Lunar and Planetary Science Conference, p. Abstract #2070.
- Heck, P., Pellin, M., Davis, A., Martin, I., Renaud, L., Benbalagh, R., Isheim, D., Seidman, D., Hiller, J. and Stephan, T. (2010) Atom-Probe Tomographic Analyses of Presolar Silicon Carbide Grains and Meteoritic Nanodiamonds---First Results on Silicon Carbide, 41st Lunar and Planetary Science Conference, p. Abstract #2112.
- Heck, P. R., Gyngard, F., Ott, U., Meier, M. M. M., Avila, J. N., Amari, S., Zinner, E. K., Lewis, R. S., Baur, H. and Wieler, R. (2009). Interstellar residence times of presolar SiC dust grains from the Murchison carbonaceous meteorite. *The Astrophysical Journal* **698**:1155-1164.
- Heck, P. R., Pellin, M. J., Davis, A. M., Isheim, D., Seidman, D. N., Hiller, J., Mane, A., Elam, J., Savina, M. R., Stephan, T., Stadermann, F. J., Zhao, X., Daulton, T. L. and Floss, C. (2011c). Atom-probe tomography of meteoritic and synthetic nanodiamonds. *Meteoritics & Planetary Science* **46**:A90-A90.
- Heck, P. R., Stadermann, F. J., Isheim, D., Auciello, O., Daulton, T. L., Davis, A. M., Elam, J. W., Floss, C., Hiller, J. and Larson, D. J. (2014). Atom-probe analyses of nanodiamonds from Allende. *Meteoritics & Planetary Science* **49**:453-467.
- Hedrosa, R., Abia, C., Busso, M., Cristallo, S., Domínguez, I., Palmerini, S., Plez, B. and Straniero, O. (2013). Nitrogen isotopes in asymptotic giant branch carbon stars and presolar SiC grains: A challenge for stellar nucleosynthesis. *The Astrophysical Journal Letters* **768**:L11.
- Henkel, T., Stephan, T., Jessberger, E. K., Hoppe, P., Strebel, R., Amari, S. and Lewis, R. S. (2007a). 3-D elemental and isotopic composition of presolar silicon carbides. *Meteoritics & Planetary Science* **42**:1121-1134.
- Henkel, T., Tizard, J., Blagburn, D. and Lyon, I. (2006). Interstellar dust laser explorer (IDLE): A new instrument for submicron analyses of stardust-quantification of laser SNMS. *Applied surface science* **252**:7117-7119.

- Henkel, T., Tizard, J., Blagburn, D. J. and Lyon, I. C. (2007b). IDLE- Interstellar dust laser explorer: A new instrument for elemental and isotopic analysis and imaging of interstellar and interplanetary dust. *Review of Scientific Instruments* **78**:055107.
- Herbst, E. and Van Dishoeck, E. F. (2009). Complex organic interstellar molecules. *Annual Review of Astronomy and Astrophysics* **47**:427-480.
- Herwig, F. (2001). The Evolutionary Timescale of Sakurai's Object: A Test of Convection Theory? *The Astrophysical Journal Letters* **554**:L71.
- Herwig, F., Pignatari, M., Woodward, P. R., Porter, D. H., Rockefeller, G., Fryer, C. L., Bennett, M. and Hirschi, R. (2011). Convective-reactive Proton-12C Combustion in Sakurai's Object (V4334 Sagittarii) and Implications for the Evolution and Yields from the First Generations of Stars. *The Astrophysical Journal* **727**:89.
- Hirashita, H., Nozawa, T., Asano, R. S. and Lee, T. (2016). Revisiting the lifetime estimate of large presolar grains in the interstellar medium. *Planetary and Space Science* **133**:17-22.
- Hoppe, P., Amari, S., Zinner, E., Ireland, T. and Lewis, R. S. (1994). Carbon, nitrogen, magnesium, silicon, and titanium isotopic compositions of single interstellar silicon carbide grains from the Murchison carbonaceous chondrite. *The Astrophysical Journal* **430**:870-890.
- Hoppe, P., Amari, S., Zinner, E. and Lewis, R. S. (1995). Isotopic compositions of C, N, O, Mg, and Si, trace element abundances, and morphologies of single circumstellar graphite grains in four density fractions from the Murchison meteorite. *Geochimica et Cosmochimica Acta* **59**:4029-4056.
- Hoppe, P., Annen, P., Strebel, R., Eberhardt, P., Gallino, R., Lugaro, M., Amari, S. and Lewis, R. S. (1997). Meteoritic silicon carbide grains with unusual Si-isotopic compositions: Evidence for an origin in low-mass, low-metallicity asymptotic giant branch stars. *The Astrophysical Journal* **487**:L101-L104.
- Hoppe, P. and Besmehn, A. (2002). Evidence for extinct vanadium-49 in presolar silicon carbide grains from supernovae. *The Astrophysical Journal* **576**:L69-L72.
- Hoppe, P., Fujiya, W. and Zinner, E. (2012). Sulfur molecule chemistry in supernova ejecta recorded by silicon carbide stardust. *The Astrophysical Journal Letters* **745**:L26.
- Hoppe, P., Leitner, J., Groner, E., Marhas, K. K., Meyer, B. S. and Amari, S. (2010). NanoSIMS studies of small presolar SiC grains: New insights into supernova nucleosynthesis, chemistry and dust formation. *The Astrophysical Journal* **719**:1370-1384.
- Hoppe, P., Lodders, K. and Fujiya, W. (2015). Sulfur in presolar silicon carbide grains from asymptotic giant branch stars. *Meteoritics & Planetary Science* **50**:1122-1138.
- Hoppe, P. and Ott, U. (1997) Mainstream silicon carbide grains from meteorites, in: Bernatowicz, T., Zinner, E. (Eds.), AIP Conference Proceedings. AIP, pp. 27-58.

- Hoppe, P., Pignatari, M., Kodolányi, J., Gröner, E. and Amari, S. (2018). NanoSIMS isotope studies of rare types of presolar silicon carbide grains from the Murchison meteorite: Implications for supernova models and the role of ^{14}C . *Geochimica et Cosmochimica Acta* **221**:182-199.
- Hoppe, P., Strebel, R., Eberhardt, P., Amari, S. and Lewis, R. S. (1996a). Small SiC grains and a nitride grain of circumstellar origin from the Murchison meteorite: Implications for stellar evolution and nucleosynthesis. *Geochimica et Cosmochimica Acta* **60**:883-907.
- Hoppe, P., Strebel, R., Eberhardt, P., Amari, S. and Lewis, R. S. (1996b). Type II supernova matter in a silicon carbide grain from the Murchison meteorite. *Science* **272**:1314-1316.
- Hoppe, P., Strebel, R., Eberhardt, P., Amari, S. and Lewis, R. S. (2000). Isotopic properties of silicon carbide X grains from the Murchison meteorite in the size range 0.5-1.5 μm . *Meteoritics & Planetary Science* **35**:1157-1176.
- Hoyle, F. (1954). On Nuclear Reactions Occuring in Very Hot Stars. I. the Synthesis of Elements from Carbon to Nickel. *The Astrophysical Journal Supplement Series* **1**:121.
- Hoyle, F., Dunbar, D. N. F., Wenzel, W. A. and Whaling, W. (1953). A state in C-12 predicted from astrophysical evidence. *Physical Review* **92**:1095-1095.
- Hughes, J. P., Rakowski, C. E., Burrows, D. N. and Slane, P. O. (1999). Nucleosynthesis and mixing in Cassiopeia A. *The Astrophysical Journal Letters* **528**:L109.
- Huss, G. R. (1997) The survival of presolar grains in solar system bodies, in: Bernatowicz, T., Zinner, E. (Eds.), AIP Conference Proceedings. AIP, pp. 721-748.
- Huss, G. R., Hutcheon, I. D. and Wasserburg, G. (1997). Isotopic systematics of presolar silicon carbide from the Orgueil (CI) chondrite: Implications for solar system formation and stellar nucleosynthesis. *Geochimica et Cosmochimica Acta* **61**:5117-5148.
- Huss, G. R. and Lewis, R. S. (1995). Presolar diamond, SiC, and graphite in primitive chondrites: Abundances as a function of meteorite class and petrologic type. *Geochimica et Cosmochimica Acta* **59**:115-160.
- Huss, G. R. and Smith, J. B. (2007). Titanium isotopic compositions of well-characterized silicon carbide grains from Orgueil (CI): Implications for s-process nucleosynthesis. *Meteoritics & Planetary Science* **42**:1055-1075.
- Hutcheon, I., Huss, G., Fahey, A. and Wasserburg, G. (1994). Extreme Mg-26 and O-17 enrichments in an Orgueil corundum: Identification of a presolar oxide grain. *The Astrophysical Journal* **425**:L97-L100.
- Hynes, K. and Gyngard, F. (2009) The Presolar Grain Database: <http://presolar.wustl.edu/~pgd>, 40th Lunar and Planetary Science Conference, p. Abstract #1198.

- Hynes, K. M., Amari, S., Bernatowicz, T. J., Lebsack, E., Gyngard, F. and Nittler, L. R. (2011) Combined TEM and NanoSIMS Analysis of Subgrains in a SiC AB Grain, 42nd Lunar and Planetary Science Conference. Lunar and Planetary Institute, The Woodlands, Texas, p. Abstract #2332.
- Hynes, K. M., Croat, T. K., Amari, S., Mertz, A. F. and Bernatowicz, T. J. (2010). Structural and isotopic microanalysis of presolar SiC from supernovae. *Meteoritics & Planetary Science* **45**:596-614.
- Iben, I. and Renzini, A. (1983). Asymptotic giant branch evolution and beyond. *Annual Review of Astronomy and Astrophysics* **21**:271-342.
- Jochum, K. P., Dingwell, D. B., Rocholl, A., Stoll, B., Hofmann, A. W., Becker, S., Besmehn, A., Bessette, D., Dietze, H. J. and Dulski, P. (2000). The Preparation and Preliminary Characterisation of Eight Geological MPI-DING Reference Glasses for In-Situ Microanalysis. *Geostandards and Geoanalytical Research* **24**:87-133.
- Jochum, K. P., Stoll, B., Herwig, K., Willbold, M., Hofmann, A. W., Amini, M., Aarburg, S., Abouchami, W., Hellebrand, E. and Mocek, B. (2006). MPI-DING reference glasses for in situ microanalysis: New reference values for element concentrations and isotope ratios. *Geochemistry, Geophysics, Geosystems* **7**.
- Jochum, K. P., Weis, U., Stoll, B., Kuzmin, D., Yang, Q., Raczek, I., Jacob, D. E., Stracke, A., Birbaum, K. and Frick, D. A. (2011). Determination of reference values for NIST SRM 610–617 glasses following ISO guidelines. *Geostandards and Geoanalytical Research* **35**:397-429.
- Jones, A., Tielens, A., Hollenbach, D. and McKee, C. (1994). Grain destruction in shocks in the interstellar medium. *The Astrophysical Journal* **433**:797-810.
- Jones, A. P., Tielens, A. G. G. M., Hollenbach, D. J. and McKee, C. F. (1997) The propagation and survival of interstellar grains, in: Bernatowicz, T. J., Zinner, E. (Eds.), *Astrophysical Implications of the Laboratory Study of Presolar Materials*. AIP Press, Woodbury, pp. 595-613.
- José, J., Coc, A. and Hernanz, M. (1999). Nuclear uncertainties in the NeNa-MgAl cycles and production of ²²Na and ²⁶Al during nova outbursts. *The Astrophysical Journal* **520**:347-360.
- José, J. and Hernanz, M. (2007). The origin of presolar nova grains. *Meteoritics & Planetary Science* **42**:1135-1143.
- José, J., Hernanz, M., Amari, S., Lodders, K. and Zinner, E. (2004). The imprint of nova nucleosynthesis in presolar grains. *The Astrophysical Journal* **612**:414-428.
- José, J., Hernanz, M., Amari, S. and Zinner, E. (2003). Constraining models of classical nova outbursts with the Murchison meteorite. *Publications of the Astronomical Society of Australia* **20**:351-355.

- Karakas, A. I., Campbell, S. W. and Stancliffe, R. J. (2010). Is Extra Mixing Really Needed in Asymptotic Giant Branch Stars? *The Astrophysical Journal* **713**:374.
- Kifonidis, K., Plewa, T., Janka, H.-T. and Müller, E. (2003). Non-spherical core collapse supernovae-I. Neutrino-driven convection, Rayleigh-Taylor instabilities, and the formation and propagation of metal clumps. *Astronomy & Astrophysics* **408**:621-649.
- King, A. J., Henkel, T., Rost, D. and Lyon, I. C. (2012). Trace element depth profiles in presolar silicon carbide grains. *Meteoritics & Planetary Science* **47**:1624-1643.
- Kodolányi, J., Vollmer, C., Hoppe, P. and Müller, M. (2016) NanoSIMS and TEM Investigations of Supernova SiC Grains, 47th Lunar and Planetary Science Conference. Lunar and Planetary Institute, Houston, p. Abstract #1478.
- Koehler, P. E., Spencer, R. R., Guber, K. H., Winters, R. R., Raman, S., Harvey, J. A., Hill, N. W., Blackmon, J. C., Bardayan, D. W., Larson, D. C., Lewis, T. A., Pierce, D. E. and Smith, M. S. (1998) High resolution neutron capture and transmission measurements on Ba-137 and their impact on the interpretation of meteoric barium anomalies, in: Mezzacappa, A. (Ed.), *Stellar Evolution, Stellar Explosions and Galactic Chemical Evolution*, pp. 337-343.
- Kovetz, A. and Prialnik, D. (1997). The composition of nova ejecta from multicycle evolution models. *The Astrophysical Journal* **477**:356-367.
- Lagadec, E., Zijlstra, A. A., Sloan, G. C., Matsuura, M., Wood, P. R., van Loon, J. T., Harris, G. J., Blommaert, J., Hony, S., Groenewegen, M. A. T., Feast, M. W., Whitelock, P. A., Menzies, J. W. and Cioni, M. R. (2007). Spitzer spectroscopy of carbon stars in the Small Magellanic Cloud. *Monthly Notices of the Royal Astronomical Society* **376**:1270-1284.
- Lambert, D. L., Gustafsson, B., Eriksson, K. and Hinkle, K. H. (1986). The chemical composition of carbon stars. I-Carbon, nitrogen, and oxygen in 30 cool carbon stars in the Galactic disk. *The Astrophysical Journal Supplement Series* **62**:373-425.
- Larimer, J. W. and Bartholomay, M. (1979). The role of carbon and oxygen in cosmic gases: Some applications to the chemistry and mineralogy of enstatite chondrites. *Geochimica et Cosmochimica Acta* **43**:1455-1466.
- Leitner, J., Vollmer, C., Floss, C., Zipfel, J. and Hoppe, P. (2016). Ancient stardust in fine-grained chondrule dust rims from carbonaceous chondrites. *Earth and Planetary Science Letters* **434**:117-128.
- Leitner, J., Vollmer, C., Hoppe, P. and Zipfel, J. (2012). Characterization of presolar material in the CR chondrite Northwest Africa 852. *The Astrophysical Journal* **745**:38-53.
- Lewis, J. B., Isheim, D., Floss, C., Daulton, T. and Seidman, D. (2016) Analysis of Allende Nanodiamond Residue by Correlated Transmission Electron Microscopy and Atom-Probe Tomography, 47th Lunar and Planetary Science Conference, p. Abstract #2248.

- Lewis, J. B., Isheim, D., Floss, C., Daulton, T. L. and Seidman, D. N. (2014a) New Atom-Probe Tomography Data and Improved Techniques for Meteoritic Nanodiamond Analysis, 45th Lunar and Planetary Science Conference. Lunar and Planetary Institute, The Woodlands, Texas, p. Abstract #2607.
- Lewis, J. B., Isheim, D., Floss, C., Groopman, E., Gyngard, F. and Seidman, D. N. (2014b) Isotopic Composition and Trace Element Abundances of a Presolar SiC AB Grain Reconstructed by Atom-Probe Tomography, 77th Annual Meeting of the Meteoritical Society. Lunar and Planetary Institute, Casablanca, Morocco, p. Abstract #5367.
- Lewis, J. B., Isheim, D., Floss, C. and Seidman, D. N. (2017) Normalized Distributions of Nanodiamond $^{12}\text{C}/^{13}\text{C}$ Isotopic Ratios from Allende by Atom-Probe Tomography, 48th Lunar and Planetary Science Conference. Lunar and Planetary Institute, Houston, p. Abstract #2555.
- Lewis, J. B., Isheim, D., Moutanabbir, O., Floss, C. and Seidman, D. N. (2015). Standardization and correction of artifacts in atom-probe tomographic analysis of Allende nanodiamonds. *Meteoritics & Planetary Science* **50**.
- Lewis, R. S., Amari, S. and Anders, E. (1990). Meteoritic silicon carbide: pristine material from carbon stars. *Nature* **348**:293-298.
- Lewis, R. S., Amari, S. and Anders, E. (1994). Interstellar grains in meteorites: II. SiC and its noble gases. *Geochimica et Cosmochimica Acta* **58**:471-494.
- Lewis, R. S., Ming, T., Wacker, J. F., Anders, E. and Steel, E. (1987). Interstellar diamonds in meteorites. *Nature* **326**:160-162.
- Lin, Y., Gyngard, F. and Zinner, E. (2010). Isotopic analysis of supernova SiC and Si₃N₄ grains from the Qingzhen (EH3) chondrite. *The Astrophysical Journal* **709**:1157.
- Liu, N., Nittler, L. R., Alexander, C. M. D., Wang, J., Pignatari, M., José, J. and Nguyen, A. (2016). Stellar origins of extremely ^{13}C -AND ^{15}N -enriched presolar sic grains: Novae or Supernovae? *The Astrophysical Journal* **820**:140.
- Lodders, K. and Amari, S. (2005). Presolar grains from meteorites: Remnants from the early times of the solar system. *Chemie Der Erde-Geochemistry* **65**:93-166.
- Lodders, K. and Fegley, B. (1995). The origin of circumstellar silicon carbide grains found in meteorites. *Meteoritics* **30**:661-678.
- Lodders, K. and Fegley, B. (1997) Condensation chemistry of carbon stars, AIP Conference Proceedings. AIP, pp. 391-423.
- Lodders, K. and Fegley, B. (1999) Condensation chemistry of circumstellar grains, Symposium-International Astronomical Union. Cambridge Univ Press, pp. 279-290.

- Lugaro, M., Herwig, F., Lattanzio, J. C., Gallino, R. and Straniero, O. (2003). S-process nucleosynthesis in asymptotic giant branch stars: A test for stellar evolution. *The Astrophysical Journal* **586**:1305-1319.
- Lugaro, M., Karakas, A. I., Bruno, C. G., Aliotta, M., Nittler, L. R., Bemmerer, D., Best, A., Boeltzig, A., Broggini, C., Caciolli, A., Cavanna, F., Ciani, G. F., Corvisiero, P., Davinson, T., Depalo, R., Di Leva, A., Elekes, Z., Ferraro, F., Formicola, A., Fülöp, Z., Gervino, G., Guglielmetti, A., Gustavino, C., Gyürky, G., Imbriani, G., Junker, M., Menegazzo, R., Mossa, V., Pantaleo, F. R., Piatti, D., Prati, P., Scott, D. A., Straniero, O., Strieder, F., Szücs, T., Takács, M. P. and Trezzi, D. (2017). Origin of meteoritic stardust unveiled by a revised proton-capture rate of ^{17}O . *Nature Astronomy* **1**:0027.
- Lugaro, M., Zinner, E., Gallino, R. and Amari, S. (1999). Si isotopic ratios in mainstream presolar SiC grains revisited. *The Astrophysical Journal* **527**:369-394.
- Lyon, I., Clarke, A., Henkel, T., Moore, K. and McMahon, G. (2016) Very High Spatial Resolution Isotope and Elemental Imaging of Pre-Solar SiC Grains: Topographic and Imaging Artefacts that may lead to Apparent, but Spurious, Heterogeneity Within Grains, 79th Annual Meeting of the Meteoritical Society, p. Abstract #1921.
- Lyon, I., Henkel, T. and Clarke, A. (2015) High Spatial Resolution Isotope Ratio Imaging and 3D Reconstruction of Presolar SiC Grains, 78th Annual Meeting of the Meteoritical Society, p. Abstract #5297.
- Lyon, I. C., Tizard, J. M. and Henkel, T. (2007). Evidence for lithium and boron from star-forming regions implanted in presolar SiC grains. *Meteoritics & Planetary Science* **42**:373-385.
- Marhas, K. K., Amari, S., Gyngard, F., Zinner, E. and Gallino, R. (2008). Iron and nickel isotopic ratios in presolar SiC grains. *The Astrophysical Journal* **689**:622-645.
- Marhas, K. K., Hoppe, P. and Ott, U. (2007). NanoSIMS studies of Ba isotopic compositions in single presolar silicon carbide grains from AGB stars and supernovae. *Meteoritics & Planetary Science* **42**:1077-1101.
- McKeegan, K. D., Aléon, J., Bradley, J., Brownlee, D., Busemann, H., Butterworth, A., Chaussidon, M., Fallon, S., Floss, C. and Gilmour, J. (2006). Isotopic compositions of cometary matter returned by Stardust. *Science* **314**:1724-1728.
- Mendybaev, R. A., Beckett, J. R., Grossman, L., Stolper, E., Cooper, R. F. and Bradley, J. P. (2002). Volatilization kinetics of silicon carbide in reducing gases: An experimental study with applications to the survival of presolar grains in the solar nebula. *Geochimica et Cosmochimica Acta* **66**:661-682.
- Messenger, S., Keller, L. P. and Lauretta, D. S. (2005). Supernova olivine from cometary dust. *Science* **309**:737-741.
- Messenger, S., Keller, L. P., Stadermann, F. J., Walker, R. M. and Zinner, E. (2003). Samples of stars beyond the solar system: Silicate grains in interplanetary dust. *Science* **300**:105-108.

- Messenger, S., Sandford, S. and Brownlee, D. (2006) The population of starting materials available for solar system construction, *Meteorites and the early solar system II*, pp. 187-208.
- Meyer, B. and Clayton, D. (2000). Molybdenum and zirconium isotopes from a supernova neutron burst. *The Astrophysical Journal Letters* **540**:L49.
- Nagashima, K., Krot, A. N. and Yurimoto, H. (2004). Stardust silicates from primitive meteorites. *Nature* **428**:921-924.
- Newton, J., Bischoff, A., Arden, J., Franchi, I., Geiger, T., Greshake, A. and Pillinger, C. (1995). Acfer 094, a uniquely primitive carbonaceous chondrite from the Sahara. *Meteoritics & Planetary Science* **30**:47-56.
- Nguyen, A., Zinner, E. and Lewis, R. S. (2003). Identification of small presolar spinel and corundum grains by isotopic raster imaging. *Publications of the Astronomical Society of Australia* **20**:382-388.
- Nguyen, A. N., Nakamura-Messenger, K., Messenger, S., Keller, L. P. and Klöck, W. (2014) Identification of a Compound Spinel and Silicate Presolar Grain in a Chondritic Interplanetary Dust Particle, 45th Lunar and Planetary Science Conference. Lunar and Planetary Institute, Houston, p. Abstract #2351.
- Nguyen, A. N., Nittler, L. R., Alexander, C. M. D. and Hoppe, P. (2018). Titanium isotopic compositions of rare presolar SiC grain types from the Murchison meteorite. *Geochimica et Cosmochimica Acta* **221**:162-181.
- Nguyen, A. N. and Zinner, E. (2004). Discovery of ancient silicate stardust in a meteorite. *Science* **303**:1496-1499.
- Nicolussi, G. K., Davis, A. M., Pellin, M. J., Lewis, R. S., Clayton, R. N. and Amari, S. (1997). s-process zirconium in presolar silicon carbide grains. *Science* **277**:1281-1283.
- Nicolussi, G. K., Pellin, M. J., Lewis, R. S., Davis, A. M., Clayton, R. N. and Amari, S. (1998). Strontium isotopic composition in individual circumstellar silicon carbide grains: A record of s-process nucleosynthesis. *Physical Review Letters* **81**:3583-3586.
- Nittler, L., Gallino, R., Lugaro, M., Straniero, O., Domínguez, I. and Zinner, E. (2005a). Si and C isotopes in presolar silicon carbide grains from AGB stars. *Nuclear Physics A* **758**:348-351.
- Nittler, L. R. (2006). Correlated microanalysis of presolar materials. *Meteoritics & Planetary Science* **41**:A133-A133.
- Nittler, L. R. and Alexander, C. (1999) Automatic identification of presolar Al- and Ti-rich oxide grains from ordinary chondrites, 30th Lunar and Planetary Science Conference, p. Abstract #2041.

- Nittler, L. R. and Alexander, C. M. O. (2003). Automated isotopic measurements of micron-sized dust: Application to meteoritic presolar silicon carbide. *Geochimica et Cosmochimica Acta* **67**:4961-4980.
- Nittler, L. R., Alexander, C. M. O., Gallino, R., Hoppe, P., Nguyen, A. N., Stadermann, F. J. and Zinner, E. K. (2008). Aluminum-, calcium- and titanium-rich oxide stardust in ordinary chondrite meteorites. *The Astrophysical Journal* **682**:1450-1478.
- Nittler, L. R., Alexander, C. M. O., Gao, X., Walker, R. M. and Zinner, E. (1997). Stellar sapphires: The properties and origins of presolar Al₂O₃ in meteorites. *The Astrophysical Journal* **483**:475-495.
- Nittler, L. R., Alexander, C. M. O., Gao, X., Walker, R. M. and Zinner, E. K. (1994). Interstellar oxide grains from the Tieschitz ordinary chondrite. *Nature* **370**:443-446.
- Nittler, L. R., Alexander, C. M. O., Stadermann, F. J. and Zinner, E. K. (2005b). Presolar chromite in Orgueil. *Meteoritics & Planetary Science* **40**:5208.
- Nittler, L. R., Amari, S., Zinner, E., Woosley, S. E. and Lewis, R. S. (1996). Extinct Ti-44 in presolar graphite and SiC: Proof of a supernova origin. *The Astrophysical Journal* **462**:L31-L34.
- Nittler, L. R., Hoppe, P., Alexander, C. M. O., Amari, S., Eberhardt, P., Gao, X., Lewis, R. S., Strebel, R., Walker, R. M. and Zinner, E. (1995). Silicon nitride from supernovae. *The Astrophysical Journal* **453**:L25-L28.
- Nollett, K. M., Busso, M. and Wasserburg, G. (2003). Cool bottom processes on the thermally pulsing asymptotic giant branch and the isotopic composition of circumstellar dust grains. *The Astrophysical Journal* **582**:1036.
- Nuth, J. A., Charnley, S. B. and Johnson, N. M. (2006) Chemical processes in the interstellar medium: Source of the gas and dust in the primitive solar nebula, Meteorites and the early solar system II. The University of Arizona Press, pp. 147-167.
- Pellin, M. J., Davis, A. M., Calaway, W. F., Lewis, R. S., Clayton, R. N. and Amari, S. (2000) Zr and Mo Isotopic Constraints on the Origins of Unusual Types of Presolar SiC Grains, 31st Lunar and Planetary Science Conference. Lunar and Planetary Institute, Houston, Texas, p. Abstract #1934.
- Pignatari, M., Gobel, K., Reifarth, R., Travaglio, C. and NuGrid, C. (2016). The production of proton-rich isotopes beyond iron: The gamma-process in stars. *International Journal of Modern Physics E-Nuclear Physics* **25**.
- Pignatari, M., Wiescher, M., Timmes, F., De Boer, R., Thielemann, F.-K., Fryer, C., Heger, A., Herwig, F. and Hirschi, R. (2013a). Production of carbon-rich presolar grains from massive stars. *The Astrophysical Journal Letters* **767**:L22.
- Pignatari, M., Zinner, E., Bertolli, M., Trappitsch, R., Hoppe, P., Rauscher, T., Fryer, C., Herwig, F., Hirschi, R. and Timmes, F. (2013b). Silicon carbide grains of type c

provide evidence for the production of the unstable isotope ^{32}Si in supernovae. *The Astrophysical Journal Letters* **771**:L7.

Pignatari, M., Zinner, E., Hoppe, P., Jordan, C. J., Gibson, B. K., Trappitsch, R., Herwig, F., Fryer, C., Hirschi, R. and Timmes, F. X. (2015). Carbon-rich Presolar Grains from Massive Stars: Subsolar $^{12}\text{C}/^{13}\text{C}$ and $^{14}\text{N}/^{15}\text{N}$ Ratios and the Mystery of ^{15}N . *The Astrophysical Journal Letters* **808**:L43.

Rauscher, T., Heger, A., Hoffman, R. and Woosley, S. (2002). Nucleosynthesis in massive stars with improved nuclear and stellar physics. *The Astrophysical Journal* **576**:323-378.

Rayet, M., Arnould, M., Hashimoto, M., Prantzos, N. and Nomoto, K. (1995). The p-process in Type II supernovae. *Astronomy & Astrophysics* **298**:517.

Reynolds, J. H. and Turner, G. (1964). Rare gases in the chondrite Renazzo. *Journal of Geophysical Research* **69**:3263-3281.

Russell, S. S., Arden, J. W. and Pillinger, C. (1996). A carbon and nitrogen isotope study of diamond from primitive chondrites. *Meteoritics & Planetary Science* **31**:343-355.

Sandford, S. A. and Allamandola, L. J. (1993). Condensation and vaporization studies of CH_3OH and NH_3 ices- Major implications for astrochemistry. *The Astrophysical Journal* **417**:815-825.

Savina, M. R., Tripa, C. E., Pellin, M. J., Davis, A. M., Clayton, R. N., Lewis, R. S. and Amari, S. (2003) Isotopic Composition of Molybdenum and Barium in Single Presolar Silicon Carbide Grains of Type A+B, 34th Lunar and Planetary Science Conference. Lunar and Planetary Institute, Houston, Texas, p. Abstract #2079.

Seeger, P. A., Fowler, W. A. and Clayton, D. D. (1965). Nucleosynthesis of Heavy Elements by Neutron Capture. *The Astrophysical Journal Supplement Series* **11**:121-157.

Sloan, G., Kraemer, K., McDonald, I., Groenewegen, M., Wood, P., Zijlstra, A., Lagadec, E., Boyer, M., Kemper, F. and Matsuura, M. (2016). The infrared spectral properties of magellanic carbon stars. *The Astrophysical Journal* **826**:44-63.

Stadermann, F., Zhao, X., Daulton, T., Isheim, D., Seidman, D., Heck, P., Pellin, M., Savina, M., Davis, A. and Stephan, T. (2010) Atom-probe tomographic study of the three-dimensional structure of presolar silicon carbide and nanodiamonds at atomic resolution, 41st Lunar and Planetary Science Conference, p. Abstract #2134.

Stadermann, F. J., Isheim, D., Zhao, X., Daulton, T. L., Floss, C., Seidman, D. N., Heck, P. R., Pellin, M. J., Savina, M. R., Hiller, J., Mane, A., Elam, J., Davis, A. M., Stephan, T. and Amari, S. (2011) Atom-Probe Tomographic Characterization of Meteoritic Nanodiamonds and Presolar SiC, 42nd Lunar and Planetary Science Conference. Lunar and Planetary Institute, The Woodlands, Texas, p. Abstract #1595.

Starrfield, S., Truran, J., Wiescher, M. and Sparks, W. (1998). Evolutionary sequences for Nova V1974 Cygni using new nuclear reaction rates and opacities. *Monthly Notices of the Royal Astronomical Society* **296**:502-522.

- Stephan, T. (2001). TOF-SIMS in cosmochemistry. *Planetary and Space Science* **49**:859-906.
- Stephan, T. and Jessberger, E. K. (1996) TOF-SIMS analysis of interstellar SiC grains, , 27th Lunar and Planetary Science Conference, p. Abstract #1267.
- Stephan, T., Rost, D., Jessberger, E., Budell, R., Greshake, A., Zinner, E., Amari, S., Hoppe, P. and Lewis, R. (1997) TOF-SIMS analysis of SiC grains with high lateral resolution, 28th Lunar and Planetary Science Conference, p. Abstract #1371.
- Stephan, T., Trappitsch, R., Boehnke, P., Davis, A. M., Pellin, M. J. and Pardo, O. S. (2017) Analysis of Strontium, Zirconium, Molybdenum, and Barium Isotopes in Presolar Silicon Carbide Grains with CHILI, 48th Lunar and Planetary Science Conference. Lunar and Planetary Institute, Houston, p. Abstract #2513.
- Stephan, T., Trappitsch, R., Davis, A., Pellin, M., Rost, D., Savina, M. and Dauphas, N. (2015a) Simultaneous Analysis of Strontium, Zirconium, and Barium Isotopes in Presolar Silicon Carbide Grains with CHILI, 46th Lunar and Planetary Science Conference, p. Abstract #2825.
- Stephan, T., Trappitsch, R., Davis, A. M., Gyngard, F., Hoppe, P. and Pellin, M. J. (2016a). Strontium and barium isotopes in type X presolar silicon carbide grains analyzed with CHILI- two types of supernova grains. *Meteoritics & Planetary Science* **51**:A595-A595.
- Stephan, T., Trappitsch, R., Davis, A. M., Pellin, M. J., Rost, D., Savina, M. R., Jadhav, M. and Kelly, C. H. (2015b) Isotopic composition of presolar silicon carbide grains analyzed with CHILI, 78th Annual Meeting of the Meteoritical Society, p. Abstract #1856.
- Stephan, T., Trappitsch, R., Davis, A. M., Pellin, M. J., Rost, D., Savina, M. R., Yokochi, R. and Liu, N. (2016b). CHILI – the Chicago Instrument for Laser Ionization – a new tool for isotope measurements in cosmochemistry. *International Journal of Mass Spectrometry* **407**:1-15.
- Stephan, T., Zehnpfenning, J. and Benninghoven, A. (1994). Correction of dead time effects in time-of-flight mass spectrometry. *Journal of Vacuum Science & Technology A: Vacuum, Surfaces, and Films* **12**:405-410.
- Stroud, R. M. and Bernatowicz, T. (2005) Surface and internal structure of pristine presolar silicon carbide, 36th Lunar and Planetary Science Conference, p. Abstract #2010.
- Stroud, R. M., De Gregorio, B. T., Liu, N., Alexander, C. M. O. D., Nittler, L. R., Steele, A. and Wang, J. (2017) Transmission Electron Microscopy of Rare Polytypes of Presolar SiC, 48th Lunar and Planetary Science Conference. Lunar and Planetary Institute, Houston, p. Abstract #2562.
- Suess, H. E. (1965). Chemical evidence bearing on the origin of the solar system. *Annual Review of Astronomy and Astrophysics* **3**:217-234.

- Thielemann, F.-K., Arcones, A., Käppeli, R., Liebendörfer, M., Rauscher, T., Winteler, C., Fröhlich, C., Dillmann, I., Fischer, T. and Martinez-Pinedo, G. (2011). What are the astrophysical sites for the r-process and the production of heavy elements? *Progress in Particle and Nuclear Physics* **66**:346-353.
- Timmes, F. X. and Clayton, D. D. (1996). Galactic evolution of silicon isotopes: Application to presolar SiC grains from meteorites. *The Astrophysical Journal* **472**:723-741.
- Timmes, F. X., Woosley, S. E., Hartmann, D. H. and Hoffman, R. D. (1996). The production of Ti-44 and Co-60 in supernovae. *The Astrophysical Journal* **464**:332-341.
- Tizard, J., Lyon, I. and Henkel, T. (2005). The gentle separation of presolar SiC grains from meteorites. *Meteoritics & Planetary Science* **40**:335-342.
- Trappitsch, R., Stephan, T., Davis, A., Pellin, M., Rost, D., Savina, M., Kelly, C. and Dauphas, N. (2016a) Simultaneous Analysis of Iron and Nickel Isotopes in Presolar SiC Grains with CHILI, 47th Lunar and Planetary Science Conference, p. Abstract #3025.
- Trappitsch, R., Stephan, T., Davis, A. M., Pellin, M. J., Savina, M. R., Gyngard, F., Bisterzo, S., Gallino, R. and Dauphas, N. (2016b). Iron and nickel isotopic compositions of presolar silicon carbide grains from AGB stars measured with CHILI. *Meteoritics & Planetary Science* **51**:A628-A628.
- Treffers, R. and Cohen, M. (1974). High-resolution spectra of cool stars in the 10- and 20-micron regions. *The Astrophysical Journal* **188**:545-552.
- Verchovsky, A., Wright, I. and Pillinger, C. (2003). Ion implantation into presolar grains: a theoretical model. *Publications of the Astronomical Society of Australia* **20**:329-336.
- Verchovsky, A. B., Wright, I. P., Fisenko, A. V. and Pillinger, C. T. (2001). A numerical model of ion implantation into presolar grains. *Nuclear Physics A* **688**:106-109.
- Verchovsky, A. B., Wright, I. P. and Pillinger, C. T. (2004). Astrophysical significance of asymptotic giant branch stellar wind energies recorded in meteoritic SiC grains. *The Astrophysical Journal* **607**:611-619.
- Virag, A., Wopenka, B., Amari, S., Zinner, E., Anders, E. and Lewis, R. S. (1992). Isotopic, optical, and trace element properties of large single SiC grains from the Murchison meteorite. *Geochimica et Cosmochimica Acta* **56**:1715-1733.
- Wasserburg, G., Boothroyd, A. I. and Sackmann, I.-J. (1995). Deep circulation in red giant stars: a solution to the carbon and oxygen isotope puzzles? *The Astrophysical Journal Letters* **447**:L37.
- Woosley, S. and Howard, W. (1978). The p-process in supernovae. *The Astrophysical Journal Supplement Series* **36**:285-304.

- Woosley, S. E. and Weaver, T. A. (1995). The evolution and explosion of massive stars. 2. Explosive hydrodynamics and nucleosynthesis. *The Astrophysical Journal Supplement Series* **101**:181-235.
- Wright, C. M., Do Duy, T. and Lawson, W. (2016). Absorption at 11 μm in the interstellar medium and embedded sources: evidence for crystalline silicates. *Monthly Notices of the Royal Astronomical Society* **457**:1593-1625.
- Yada, T., Floss, C., Stadermann, F. J., Zinner, E., Nakamura, T., Noguchi, T. and Lea, A. S. (2008). Stardust in Antarctic micrometeorites. *Meteoritics & Planetary Science* **43**:1287-1298.
- Zhao, X., Floss, C., Lin, Y. and Bose, M. (2013). Stardust investigation into the CR chondrite Grove Mountain 021710. *The Astrophysical Journal* **769**:49.
- Zhao, X., Floss, C., Stadermann, F., Lin, Y. and Bose, M. (2011). The stardust investigation into the CR2 chondrite GRV 021710. *Meteoritics & Planetary Science* **74**.
- Zinner, E. (2014) Presolar Grains, in: Davis, A. M. (Ed.), *Meteorites and Cosmochemical Processes - Treatise on Geochemistry* (2nd Edition), 2nd ed. Elsevier, pp. 181-213.
- Zinner, E., Amari, S., Guinness, R., Jennings, C., Mertz, A. F., Nguyen, A. N., Gallino, R., Hoppe, P., Lugaro, M. and Nittler, L. R. (2007). NanoSIMS isotopic analysis of small presolar grains: Search for Si ³ N ⁴ grains from AGB stars and Al and Ti isotopic compositions of rare presolar SiC grains. *Geochimica et Cosmochimica Acta* **71**:4786-4813.
- Zinner, E., Amari, S., Guinness, R., Nguyen, A., Stadermann, F. J., Walker, R. M. and Lewis, R. S. (2003). Presolar spinel grains from the Murray and Murchison carbonaceous chondrites. *Geochimica et Cosmochimica Acta* **67**:5083-5095.
- Zinner, E., Gyngard, F. and Nittler, L. (2010) Automated C and Si isotopic analysis of presolar SiC grains from the Indarch enstatite chondrite, 41st Lunar and Planetary Science Conference, p. Abstract #1359.
- Zinner, E., Ming, T. and Anders, E. (1987). Large isotopic anomalies of Si, C, N and noble gases in interstellar silicon carbide from the Murray meteorite. *Nature* **330**:730-732.
- Zinner, E., Ming, T. and Anders, E. (1989). Interstellar SiC in the Murchison and Murray meteorites: Isotopic composition of Ne, Xe, Si, C, and N. *Geochimica et Cosmochimica Acta* **53**:3273-3290.
- Zinner, E., Nittler, L. R., Gallino, R., Karakas, A. I., Lugaro, M., Straniero, O. and Lattanzio, J. C. (2006). Silicon and carbon isotopic ratios in AGB stars: SiC grain data, models, and the Galactic evolution of the Si isotopes. *The Astrophysical Journal* **650**:350-373.

Appendix

Grain	Type	$^{12}\text{C}/^{13}\text{C}$	$^{14}\text{N}/^{15}\text{N}$	$\delta^{29}\text{Si}$ (‰)	$\delta^{30}\text{Si}$ (‰)
AC-KJG-1	M	59.4 ± 0.8	2221 ± 145	55.4 ± 2.9	36.3 ± 3.5
AC-KJG-2	M	52.1 ± 1.1	7643 ± 231	-34.3 ± 1.9	-51.4 ± 2.3
AC-KJG-3	M	67.2 ± 0.7	3189 ± 128	28.0 ± 1.2	7.24 ± 1.43
AC-KJG-4	M	64.0 ± 0.2	5636 ± 247	60.5 ± 1.7	39.5 ± 2.1
AC-KJG-5	AB	3.46 ± 0.02	432 ± 65	-20.0 ± 14.6	-42.4 ± 17.7
AC-KJG-6	M	52.4 ± 0.9	2897 ± 189	-20.4 ± 4.4	-9.75 ± 5.49
AC-KJG-7	M	57.8 ± 0.8	2664 ± 121	67.4 ± 1.7	54.3 ± 2.1
AC-KJG-8	M	56.6 ± 0.8	2956 ± 93	69.9 ± 1.9	35.2 ± 2.3
AC-KJG-9	M	49.6 ± 0.5	1312 ± 42	106 ± 5	72.2 ± 3.8
AC-KJG-10	M	49.4 ± 0.4	1336 ± 51	-92.6 ± 9.4	-60.1 ± 11.8
AC-KJG-11	M	52.6 ± 0.5	6788 ± 312	65.8 ± 1.5	46.7 ± 1.8
AC-KJG-12	M	59.2 ± 1.1	4729 ± 213	76.7 ± 0.5	44.1 ± 0.6
AC-KJG-13	M	43.9 ± 0.9	5481 ± 276	181 ± 1	132 ± 1
AC-KJG-14	M	84.3 ± 1.3	6600 ± 294	30.7 ± 2.3	38.8 ± 2.8
AC-KJG-15	AB	3.29 ± 0.01	124 ± 57	-1.93 ± 1.70	15.3 ± 2.1
AC-KJG-16	M	94.5 ± 2.1	1760 ± 93	17.3 ± 9.7	7.08 ± 11.71
AC-KJG-17	M	87.9 ± 1.9	1065 ± 48	-7.08 ± 1.89	6.24 ± 2.33
AC-KJG-18	M	61.1 ± 1.5	1535 ± 67	34.8 ± 13.4	6.02 ± 16.20
AC-KJG-19	M	45.0 ± 0.8	875 ± 51	-11.9 ± 5.0	-32.6 ± 5.9
AC-KJG-20	M	83.4 ± 1.3	1245 ± 62	55.9 ± 0.5	47.5 ± 0.6

Table A.1: The $^{12}\text{C}/^{13}\text{C}$, $^{14}\text{N}/^{15}\text{N}$, $\delta^{29,30}\text{Si}$, and sub-groups of the presolar SiC grains analysed from the KJG residue.

Grain	Type	$^{12}\text{C}/^{13}\text{C}$	$^{14}\text{N}/^{15}\text{N}$	$\delta^{29}\text{Si}$ (‰)	$\delta^{30}\text{Si}$ (‰)
AC-MM-1	M	119 ± 3	665 ± 211	-43.2 ± 12.9	25.1 ± 16.4
AC-MM-2	AB	5.65 ± 0.01	280 ± 6	177 ± 5	146 ± 6
AC-MM-3	M	63.9 ± 0.5	402 ± 12	44.1 ± 7.3	38.6 ± 8.9
AC-MM-4	M	99.4 ± 3.6	323 ± 18	-67.3 ± 13.7	-26.3 ± 16.9
AC-MM-5	M	54.87 ± 0.14	490 ± 6	92.2 ± 1.6	66.5 ± 1.9
AC-MM-6	M	44.9 ± 0.1	240 ± 2	61.4 ± 6.3	26.3 ± 7.5
AC-MM-7	M	78.9 ± 0.3	409 ± 5	51.2 ± 4.0	36.5 ± 4.8
AC-MM-8	M	78.7 ± 0.6	306 ± 3	35.6 ± 7.1	21.1 ± 8.5
AC-MM-9	M	78.0 ± 0.4	275 ± 3	84.3 ± 6.3	71.0 ± 7.6
AC-MM-10	M	80.0 ± 0.8	291 ± 4	23.6 ± 7.0	56.5 ± 8.6
AC-MM-11	M	83.8 ± 1.2	254 ± 5	92.6 ± 18.8	21.6 ± 22.0
AC-MM-12	M	79.9 ± 1.5	252 ± 7	71.0 ± 19.7	56.5 ± 23.7
AC-MM-13	M	77.9 ± 6.7	274 ± 34	159 ± 68	-12 ± 76
AC-MM-14	M	70.1 ± 3.0	300 ± 23	-3.09 ± 36.82	-70.5 ± 43.1
AC-MM-15	M	79.9 ± 5.3	291 ± 37	-11.4 ± 79.9	-83.1 ± 93.2
AC-MM-16	M	78.2 ± 4.7	255 ± 21	0.41 ± 86.01	-214 ± 92
AC-MM-17	M	62.0 ± 5.8	631 ± 139	-96.7 ± 59.3	-142 ± 70
AC-MM-18	M	36.7 ± 4.4	239 ± 77	140 ± 134	206 ± 168
AC-MM-19	M	65.6 ± 4.4	541 ± 95	42.2 ± 56.4	88.7 ± 69.9
AC-MM-20	M	73.7 ± 2.8	252 ± 19	103 ± 36	-8.72 ± 41.47
AC-MM-21	M	54.6 ± 1.3	266 ± 10	-58.4 ± 33.6	-143 ± 39
AC-MM-22	M	81.4 ± 2.7	262 ± 19	68.6 ± 41.0	36.5 ± 49.0
AC-MM-23	M	45.0 ± 1.2	715 ± 129	11.1 ± 18.6	8.82 ± 22.56
AC-MM-24	M	49.8 ± 3.4	744 ± 55	17.1 ± 112.7	-80.6 ± 129.6
AC-MM-25	M	72.6 ± 1.3	-	69.0 ± 15.5	75.6 ± 18.8
AC-MM-26	M	49.8 ± 5.4	-	-115 ± 98	-48.8 ± 123.9
AC-MM-27	M	73.9 ± 2.1	259 ± 11	40.0 ± 39.9	41.7 ± 48.4
AC-MM-28	M	59.7 ± 2.8	272 ± 16	33.6 ± 43.9	-0.61 ± 52.33
AC-MM-29	M	78.3 ± 2.8	275 ± 12	-113 ± 51	-47.1 ± 63.9
AC-MM-30	M	80.4 ± 1.2	314 ± 10	68.8 ± 12.8	39.9 ± 15.3
AC-MM-31	M	69.4 ± 1.3	333 ± 14	-58.9 ± 11.1	-25.8 ± 13.8
AC-MM-32	M	73.8 ± 0.8	272 ± 7	52.2 ± 7.8	52.3 ± 9.4
AC-MM-33	M	70.4 ± 1.0	282 ± 8	69.2 ± 18.4	12.2 ± 21.7
AC-MM-34	M	37.3 ± 0.4	303 ± 8	67.8 ± 13.4	43.2 ± 16.0
AC-MM-35	M	83.1 ± 1.5	365 ± 14	50.0 ± 12.9	13.5 ± 15.4
AC-MM-36	M	53.6 ± 1.2	438 ± 38	-98.6 ± 19.9	-38.9 ± 24.6
AC-MM-37	M	70.5 ± 1.3	-	36.0 ± 13.9	24.6 ± 16.5
AC-MM-38	M	51.6 ± 2.3	-	75.3 ± 47.3	96.1 ± 57.2
AC-MM-39	M	77.1 ± 1.2	-	3.37 ± 14.08	60.3 ± 17.3
AC-MM-40	M	78.8 ± 1.0	-	46.0 ± 15.4	56.6 ± 18.5
AC-MM-41	M	82.1 ± 1.3	-	-6.65 ± 20.84	17.9 ± 25.3
AC-MM-42	M	73.8 ± 1.0	275 ± 9	-53.1 ± 13.5	60.9 ± 17.1
AC-MM-43	M	63.9 ± 0.4	1193 ± 63	124 ± 4	39.7 ± 4.1
AC-MM-44	M	99.1 ± 1.4	1583 ± 87	21.4 ± 2.4	-10.0 ± 2.9
AC-MM-45	AB	7.42 ± 0.04	678 ± 41	-92.6 ± 3.5	-60.1 ± 4.2

Table A.2: The $^{12}\text{C}/^{13}\text{C}$, $^{14}\text{N}/^{15}\text{N}$, $\delta^{29,30}\text{Si}$, and sub-groups of the presolar SiC grains analysed from the JA-MM residue.

Grain	Type	$^{12}\text{C}/^{13}\text{C}$	$^{14}\text{N}/^{15}\text{N}$	$\delta^{29}\text{Si}$ (‰)	$\delta^{30}\text{Si}$ (‰)
AC-MM2-1	M	60.3 ± 0.07	428 ± 4	149 ± 1	95.8 ± 1.2
AC-MM2-2	M	58.2 ± 0.0	271 ± 1	249 ± 0	111 ± 1
AC-MM2-3	M	58.5 ± 0.1	638 ± 16	161 ± 2	99.9 ± 2.3
AC-MM2-4	M	59.6 ± 0.0	977 ± 9	137 ± 1	98.4 ± 0.7
AC-MM2-5	M	59.6 ± 0.0	1930 ± 21	121 ± 1	94.3 ± 0.7
AC-MM2-6	M	62.6 ± 0.4	1053 ± 79	-118 ± 4	-45.6 ± 5.2
AC-MM2-7	M	62.4 ± 0.2	322 ± 8	115 ± 4	78.4 ± 4.4
AC-MM2-8	M	78.9 ± 1.2	377 ± 44	-101 ± 11	-52.4 ± 13.8
AC-MM2-9	M	16.2 ± 0.0	51.5 ± 0.9	271 ± 2	108 ± 2
AC-MM2-10	M	62.9 ± 0.2	775 ± 23	-87.8 ± 1.5	-37.8 ± 2.0
AC-MM2-11	M	65.3 ± 3.9	379 ± 144	70.9 ± 51.9	-52.4 ± 60.4
AC-MM2-12	M	69.6 ± 0.1	2753 ± 29	-61.2 ± 1.1	32.2 ± 1.4
AC-MM2-13	M	68.2 ± 0.5	484 ± 29	70.0 ± 6.1	48.7 ± 7.4
AC-MM2-14	M	56.7 ± 0.1	2820 ± 81	-29.6 ± 2.2	-7.03 ± 2.73
AC-MM2-15	M	70.5 ± 0.3	1158 ± 24	66.6 ± 3.2	34.1 ± 4.0
AC-MM2-16	M	61.3 ± 0.2	424 ± 9	79.1 ± 1.9	60.6 ± 2.4
AC-MM2-17	M	66.3 ± 0.0	640 ± 5	64.8 ± 0.5	38.2 ± 0.6
AC-MM2-18	X	247 ± 1	101 ± 1	-315 ± 1	-482 ± 1
AC-MM2-19	M	70.7 ± 0.0	703 ± 8	-55.8 ± 0.5	13.4 ± 0.6
AC-MM2-20	M	150 ± 1	428 ± 12	-13.3 ± 2.8	38.9 ± 3.6
AC-MM2-21	M	104 ± 0	408 ± 7	-2.84 ± 1.93	34.7 ± 2.4
AC-MM2-22	M	50.7 ± 0.1	890 ± 39	-73.8 ± 2.2	-49.6 ± 2.7
AC-MM2-23	M	63.0 ± 0.2	1117 ± 28	-12.4 ± 1.9	4.05 ± 2.38
AC-MM2-24	M	94.5 ± 0.5	3024 ± 85	-204 ± 3.59	-10.1 ± 5.0
AC-MM2-25	M	66.9 ± 0.1	864 ± 13	-3.75 ± 1.08	-37.3 ± 1.3
AC-MM2-26	M	64.5 ± 0.1	1369 ± 37	104 ± 2	72.5 ± 2.0
AC-MM2-27	M	50.4 ± 0.2	304 ± 8	114 ± 5	64.2 ± 5.8
AC-MM2-28	M	73.4 ± 0.4	247 ± 6	99.1 ± 5.0	75.4 ± 6.1
AC-MM2-29	M	81.7 ± 0.6	694 ± 39	37.2 ± 5.1	4.43 ± 6.25
AC-MM2-30	M	43.3 ± 0.2	244 ± 5	60.9 ± 15.5	11.4 ± 18.8
AC-MM2-31	M	87.6 ± 0.9	262 ± 9	-81.6 ± 7.6	95.1 ± 10.3
AC-MM2-32	M	65.7 ± 0.2	811 ± 21	-9.25 ± 2.41	-12.7 ± 3.0
AC-MM2-33	M	77.1 ± 0.3	1066 ± 15	85.9 ± 3.2	70.1 ± 3.9
AC-MM2-34	M	88.4 ± 0.3	1427 ± 51	-5.61 ± 2.04	-0.48 ± 2.54
AC-MM2-35	M	40.9 ± 0.1	719 ± 13	10.2 ± 2.2	14.3 ± 2.8
AC-MM2-36	M	71.8 ± 0.2	332 ± 5	65.8 ± 2.9	68.7 ± 3.7
AC-MM2-37	M	52.3 ± 0.2	616 ± 32	97.6 ± 3.8	76.2 ± 4.7
AC-MM2-38	M	74.3 ± 0.5	516 ± 23	147 ± 8	118 ± 9
AC-MM2-39	M	45.2 ± 0.3	684 ± 35	52.2 ± 9.0	58.1 ± 11.2
AC-MM2-40	M	64.7 ± 0.6	351 ± 17	36.9 ± 25.5	19.6 ± 31.4
AC-MM2-41	X	523 ± 2	40.7 ± 0.3	-261 ± 1	-383 ± 1
AC-MM2-42	M	63.8 ± 0.2	504 ± 1	8.90 ± 2.33	-5.17 ± 2.87
AC-MM2-43	M	73.5 ± 0.9	356 ± 4	76.6 ± 15.8	65.6 ± 19.5
AC-MM2-44	M	97.7 ± 2.6	515 ± 13	-44.3 ± 21.0	-28.4 ± 26.3

Table A.3: The $^{12}\text{C}/^{13}\text{C}$, $^{14}\text{N}/^{15}\text{N}$, $\delta^{29,30}\text{Si}$, and sub-groups of the presolar SiC grains analysed from the JA-MM2 residue.

Grain	Type	$^{12}\text{C}/^{13}\text{C}$	$^{14}\text{N}/^{15}\text{N}$	$\delta^{29}\text{Si}$ (‰)	$\delta^{30}\text{Si}$ (‰)
AC-MM2-45	M	50.8 ± 1.4	173 ± 3	-24.1 ± 38.7	-16.3 ± 48.2
AC-MM2-46	M	90.3 ± 0.3	390 ± 1	19.7 ± 2.1	18.5 ± 2.6
AC-MM2-47	M	81.5 ± 0.4	1150 ± 7	120 ± 4	66.0 ± 4.7
AC-MM2-48	M	74.4 ± 0.7	404 ± 5	60.4 ± 7.7	37.0 ± 9.4
AC-MM2-49	M	84.9 ± 1.1	631 ± 7	50.7 ± 9.0	25.0 ± 11.0
AC-MM2-50	M	90.9 ± 0.9	251 ± 2	45.6 ± 9.0	-1.40 ± 10.84
AC-MM2-51	M	81.9 ± 1.2	215 ± 2	31.0 ± 23.2	2.54 ± 28.40
AC-MM2-52	M	111 ± 2	240 ± 3	30.7 ± 25.0	20.0 ± 30.9
AC-MM2-53	M	93.0 ± 0.5	335 ± 3	21.5 ± 3.9	-0.77 ± 4.83
AC-MM2-54	M	105 ± 1	333 ± 2	-6.07 ± 4.96	-20.1 ± 6.1
AC-MM2-55	M	71.6 ± 0.5	303 ± 3	68.1 ± 4.9	37.4 ± 6.0
AC-MM2-56	M	143 ± 1	323 ± 3	39.8 ± 4.9	41.8 ± 6.1
AC-MM2-57	M	84.0 ± 1.1	312 ± 5	145 ± 13	67.2 ± 15.4
AC-MM2-58	M	69.0 ± 0.6	436 ± 4	125 ± 8	111 ± 10
AC-MM2-59	M	81.5 ± 0.4	443 ± 2	73.8 ± 3.7	-4.41 ± 4.42
AC-MM2-60	X	233 ± 2	42.2 ± 0.9	-435 ± 6	-376 ± 7
AC-MM2-61	M	24.1 ± 0.1	726 ± 5	-57.1 ± 29.4	-27.3 ± 36.6
AC-MM2-62	M	47.8 ± 0.3	-	46.2 ± 16.4	40.9 ± 20.0
AC-MM2-63	M	29.5 ± 0.3	759 ± 4	27.8 ± 6.7	30.3 ± 8.2
AC-MM2-64	M	72.4 ± 0.4	-	34.2 ± 0.9	47.5 ± 1.1
AC-MM2-65	M	67.1 ± 0.3	621 ± 5	86.2 ± 9.1	108 ± 11
AC-MM2-66	M	47.3 ± 0.3	1153 ± 7	-31.6 ± 21.5	-86.7 ± 25.6
AC-MM2-67	M	41.8 ± 0.2	819 ± 6	13.7 ± 17.9	7.64 ± 21.82
AC-MM2-68	M	62.7 ± 0.4	-	-42.0 ± 4.8	-23.2 ± 5.9
AC-MM2-69	M	92.4 ± 0.4	-	-9.59 ± 1.79	-49.3 ± 2.1
AC-MM2-70	M	12.7 ± 0.0	-	57.0 ± 8.9	-44.1 ± 10.4
AC-MM2-71	M	55.7 ± 0.3	-	-13.5 ± 16.1	-115 ± 19
AC-MM2-72	M	48.2 ± 0.2	595 ± 6	41.8 ± 24.5	-100 ± 28
AC-MM2-73	M	57.6 ± 0.2	-	-7.52 ± 38.79	-63.6 ± 46.2
AC-MM2-74	AB	2.61 ± 0.01	55.9 ± 1.1	286 ± 8	246 ± 9
AC-MM2-75	M	49.1 ± 0.3	601 ± 5	32.3 ± 3.9	31.9 ± 6.8
AC-MM2-76	AB	7.18 ± 0.04	193 ± 2	109 ± 73	-142 ± 78
AC-MM2-77	AB	5.24 ± 0.03	234 ± 2	50.3 ± 10.8	-111 ± 12
AC-MM2-78	AB	7.76 ± 0.03	53.7 ± 1.2	26.0 ± 83.6	-139 ± 94
AC-MM2-79	M	15.5 ± 0.0	408 ± 2	280 ± 222	-178 ± 216
AC-MM2-80	M	17.1 ± 0.1	-	11.1 ± 15.0	-169 ± 17
AC-MM2-81	AB	5.76 ± 0.02	248 ± 3	48.0 ± 6.6	43.7 ± 8.1
AC-MM2-82	AB	8.41 ± 0.02	196 ± 2	51.9 ± 5.1	46.6 ± 6.3
AC-MM2-83	M	29.7 ± 0.2	3296 ± 11	4.91 ± 7.10	44.0 ± 8.9
AC-MM2-84	AB	3.84 ± 0.01	275 ± 3	33.7 ± 5.2	40.5 ± 6.4
AC-MM2-85	M	57.7 ± 0.3	663 ± 4	83.9 ± 3.8	80.6 ± 4.6
AC-MM2-86	M	53.4 ± 0.5	596 ± 4	102 ± 7	104 ± 8
AC-MM2-87	M	49.0 ± 0.7	-	48.0 ± 11.8	76.4 ± 14.7
AC-MM2-88	X	74.1 ± 5.1	116 ± 3	-245 ± 36	-248 ± 44

Table A.3 continued.

Grain	Type	$^{12}\text{C}/^{13}\text{C}$	$^{14}\text{N}/^{15}\text{N}$	$\delta^{29}\text{Si}$ (‰)	$\delta^{30}\text{Si}$ (‰)
AC-Acfer-1	M	58.5 ± 0.3	4305 ± 947	46.9 ± 3.2	82.7 ± 3.9
AC-Acfer-2	M	60.2 ± 2.1	96 ± 31	20.6 ± 19.8	-7.28 ± 23.97
AC-Acfer-3	M	50.2 ± 0.2	864 ± 32	63.9 ± 2.5	59.0 ± 3.1
AC-Acfer-4	M	52.1 ± 0.4	172 ± 33	102 ± 6	-7.72 ± 6.65
AC-Acfer-5	M	90.8 ± 3.3	493 ± 64	-55.5 ± 21.3	-75.6 ± 25.8
AC-Acfer-6	M	122 ± 6	466 ± 112	-49.0 ± 17.5	19.0 ± 22.2
AC-Acfer-7	M	97.6 ± 5.0	564 ± 179	-64.1 ± 20.0	-47.4 ± 24.8
AC-Acfer-8	M	59.4 ± 1.5	2741 ± 1367	51.7 ± 13.5	27.6 ± 16.4
AC-Acfer-9	M	60.5 ± 2.4	511 ± 155	191 ± 23	127 ± 27
AC-Acfer-10	M	62.4 ± 2.2	306 ± 60	-35.8 ± 37.0	-30.9 ± 45.5
AC-Acfer-11	M	56.7 ± 2.4	330 ± 88	194 ± 26	92.9 ± 29.9
AC-Acfer-12	M	54.9 ± 1.7	627 ± 156	-4.21 ± 18.20	3.49 ± 22.42
AC-Acfer-13	M	70.4 ± 2.2	955 ± 191	9.09 ± 15.32	-4.07 ± 18.66
AC-Acfer-14	M	87.2 ± 1.4	233 ± 28	-64.5 ± 5.9	-20.8 ± 7.5
AC-Acfer-15	AB	6.76 ± 0.12	723 ± 547	47.8 ± 28.7	-24.4 ± 33.9
AC-Acfer-16	M	83.8 ± 2.7	277 ± 15	-26.1 ± 20.0	-51.2 ± 24.2
AC-Acfer-17	M	75.9 ± 3.7	198 ± 64	-43.2 ± 24.2	-20.0 ± 30.1
AC-Acfer-18	M	16.2 ± 0.3	1119 ± 507	-48.0 ± 24.6	74.9 ± 32.2
AC-Acfer-19	M	102 ± 7	365 ± 94	-157 ± 35	-35.1 ± 46.0
AC-Acfer-20	M	53.1 ± 0.9	771 ± 250	16.6 ± 11.2	22.1 ± 13.8
AC-Acfer-21	M	63.1 ± 5.3	588 ± 439	-130 ± 39	-15.1 ± 51.8
AC-Acfer-22	M	51.2 ± 3.2	408 ± 128	-19.7 ± 37.6	-14.5 ± 46.2
AC-Acfer-23	AB	9.83 ± 0.32	253 ± 92	-28.9 ± 45.2	-25.3 ± 55.6
AC-Acfer-24	M	62.2 ± 2.1	625 ± 76	71.2 ± 20.5	12.0 ± 24.6
AC-Acfer-25	M	58.3 ± 1.4	448 ± 35	118 ± 15	71.4 ± 18.5
AC-Acfer-26	M	88.5 ± 1.5	1136 ± 351	36.4 ± 8.7	22.1 ± 10.5
AC-Acfer-27	M	80.0 ± 0.1	1093 ± 37	26.1 ± 0.9	22.1 ± 1.1
AC-Acfer-28	M	48.9 ± 0.4	299 ± 15	40.6 ± 5.1	28.7 ± 6.2
AC-Acfer-29	M	53.0 ± 0.3	772 ± 84	74.7 ± 4.1	53.9 ± 4.9
AC-Acfer-30	M	64.2 ± 0.6	526 ± 19	39.0 ± 5.6	19.9 ± 6.8
AC-Acfer-31	M	51.1 ± 1.5	600 ± 93	-44.5 ± 18.0	7.14 ± 22.59
AC-Acfer-32	M	69.5 ± 0.5	2216 ± 123	31.4 ± 3.8	19.4 ± 4.6

Table A.4: The $^{12}\text{C}/^{13}\text{C}$, $^{14}\text{N}/^{15}\text{N}$, $\delta^{29,30}\text{Si}$, and sub-groups of the presolar SiC grains analysed in-situ from Acfer 094.

Grain	Type	$^{12}\text{C}/^{13}\text{C}$	$^{14}\text{N}/^{15}\text{N}$	$\delta^{29}\text{Si}$ (‰)	$\delta^{30}\text{Si}$ (‰)
AC-GRA-1	M	83.0 ± 1.0	113 ± 2	-17.1 ± 11.0	-31.7 ± 13.2
AC-GRA-2	M	57.7 ± 0.5	169 ± 3	-12.7 ± 13.5	-14.5 ± 16.4

Table A.5: The $^{12}\text{C}/^{13}\text{C}$, $^{14}\text{N}/^{15}\text{N}$, $\delta^{29,30}\text{Si}$, and sub-groups of the presolar SiC grains analysed in-situ from GRA 95229.

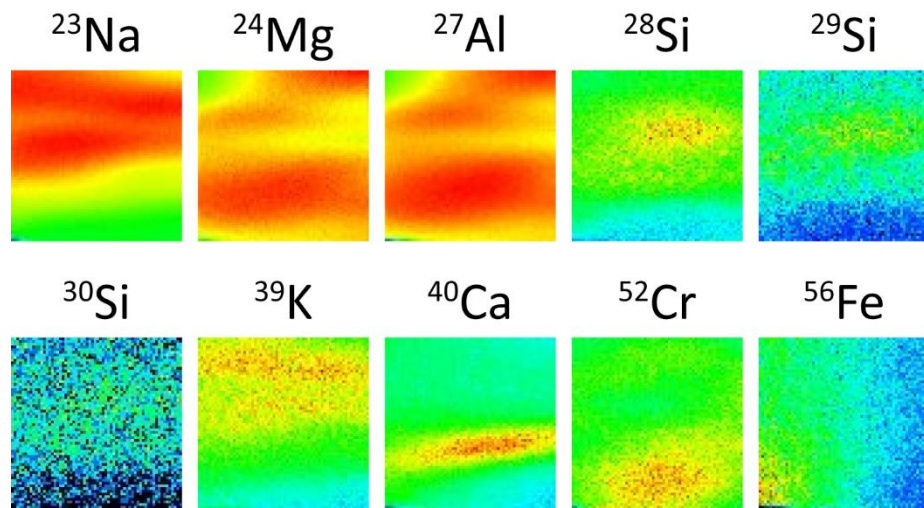


Figure A.1: Ion images of selected secondary ion species from grain AC-MM2-41, as determined by TOF-SIMS.

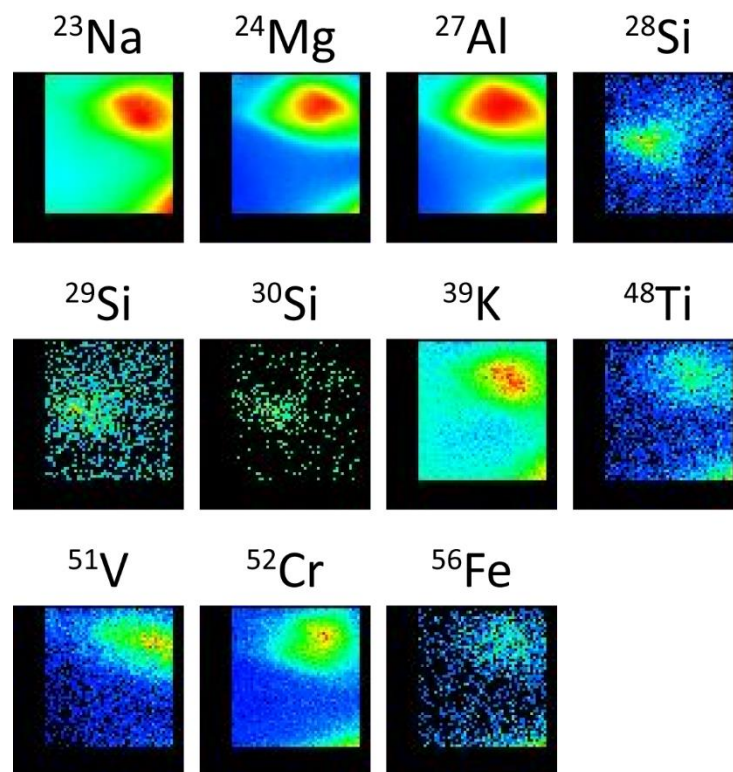


Figure A.2: Ion images of selected secondary ion species from grain MM2-1-6-3, as determined by TOF-SIMS.

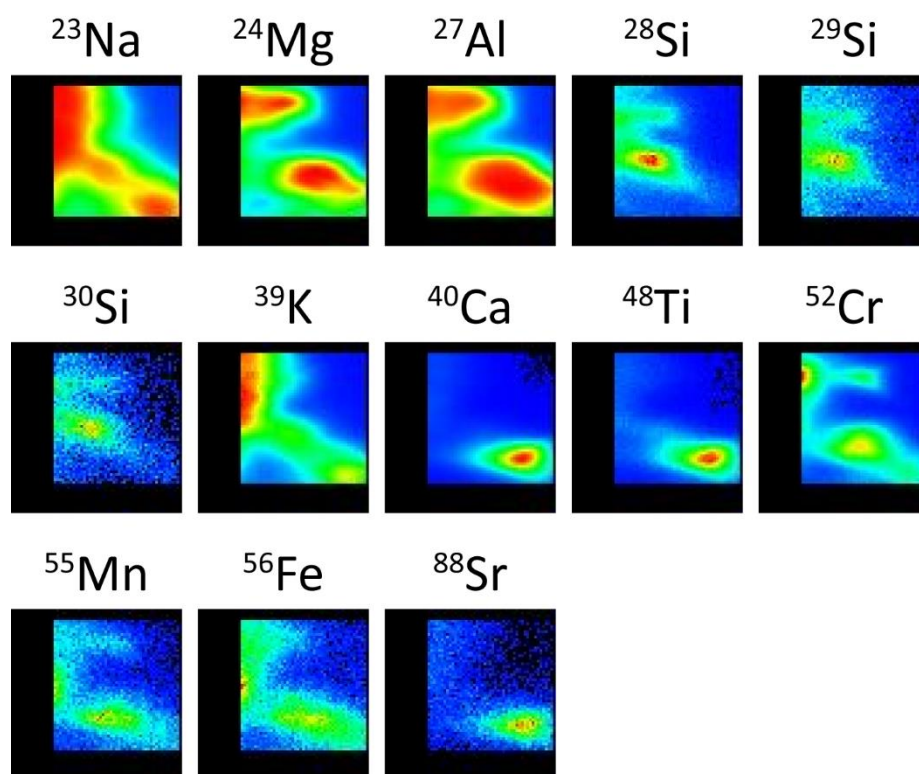


Figure A.3: Figure A.1: Ion images of selected secondary ion species from grain MM2-1-7, as determined by TOF-SIMS.